universität wien

MASTERARBEIT / MASTER'S THESIS

Titel der Masterarbeit / Title of the Master's Thesis

„Two Triplet Minima are better than One – Uncovering the Relaxation Mechanism of Photo-activated $[Re^{I}(CO)_3(bpy)(^{S\text{-}S}bpy)]^{+}$."

verfasst von / submitted by

Julia Franz, BSc

angestrebter akademischer Grad / in partial fulfilment of the requirements for the degree of

Master of Science (MSc)

Wien, 2021 / Vienna 2021

Studienkennzahl lt. Studienblatt / degree programme code as it appears on the student record sheet:	UA 066 862
Studienrichtung lt. Studienblatt / degree programme as it appears on the student record sheet:	Masterstudium Chemie
Betreut von / Supervisor:	Univ.-Prof. Dr. Dr. h.c. Leticia González Herrero

Abstract

Redox-control is often assisted by disulfide/dithiol switches in biological system. Thus, the capability of these disulfide/dithiol motifs for industrial purposes is an interesting field of research. In the framework of this thesis, a newly designed complex $[Re^{I}(CO)_3(bpy)(^{S\text{-}S}bpy)]^+$ is investigated. The complex is equipped with a sulfur-sulfur bridge, serving as a potential disulfide/dithiol switch in photo-activated proton-coupled electron transfer (PCET) reactions. The aim of this thesis is to provide theoretical insight into the excited state behavior of $[Re^{I}(CO)_3(bpy)(^{S\text{-}S}bpy)]^+$ upon photo-excitation. The theoretical studies showed, that depending on the excitation energy, different charge transfer processes are induced in the complex. These processes are defined by metal to ligand charge transfer to the two different aromatic ligands. The excited state dynamics of $[Re^{I}(CO)_3(bpy)(^{S\text{-}S}bpy)]^+$ were investigated by trajectory surface hopping in combination with time-dependent density functional theory and a linear vibronic coupling model. The results showed ultrafast intersystem crossing from the initially excited singlet states to the triplet manifold. Subsequently, two types of trajectories were observed, classified according to the structure of the complex. One type showed significant bond elongation of the sulfur-sulfur bond, the other type showed structures close to the equilibrium geometry. Optimizations of the T_1 state resulted in two minima, one with an elongated S-S bond length ($T_{1,long}$) and one similar to the equilibrium structure ($T_{1,short}$). It was therefore concluded, that the excited state dynamics lead to the population of these two minima in a 90 $T_{1,long}$: 10 $T_{1,short}$ ratio. By comparison to experimental luminescence, it was possible to assign the observed emission of $[Re^{I}(CO)_3(bpy)(^{S\text{-}S}bpy)]^+$ to phosphorescence from the $T_{1,short}$. On the other hand, relaxation from $T_{1,long}$ is achieved non-radiatively back to the ground state. Furthermore, the excited state character of $T_{1,long}$ shows local excitation at the sulfur atoms. This means, about 90% of excited population ends up in a state with high electronic density at the sulfur atoms, serving as a potential starting point for further PCET reactions. Therefore, $[Re^{I}(CO)_3(bpy)(^{S\text{-}S}bpy)]^+$ can possibly be used as a disulfide/dithiol switch in redox-controlled reactions.

Zusammenfassung

Redox-Kontrolle ist oft unterstützt durch Disulfid/Dithiol-Schalter in biologischen Systemen. Daher sind die Fähigkeiten dieser Disulfid/Dithiol-Motive für industrielle Anwendungen ein interessantes Forschungsgebiet. Im Rahmen dieser Masterarbeit wird ein neu synthetisierter Komplex $[Re^{I}(CO)_3(bpy)(^{S\text{-}S}bpy)]^+$ untersucht. Der Komplex ist mit einer Schwefel-Schwefel-Brücke ausgestattet und hat daher das Potential als Disulfid/Dithiol-Schalter in photo-aktivierten Protonen-gekoppelten Elektronentransfer (PCET) Reaktionen zu dienen. Das Ziel dieser Masterarbeit ist es theoretische Einblicke in das Verhalten von $[Re^{I}(CO)_3(bpy)(^{S\text{-}S}bpy)]^+$ im angeregten Zustand zu erhalten. Die theoretischen Studien zeigten, dass abhängig von der Anregungsenergie unterschiedliche Charge Transfer-Prozesse in dem Komplex induziert werden können. Diese Prozesse sind Metal-zu-Ligand Charge Transfere zu den beiden aromatischen Liganden möglich. Die Dynamik im angeregten Zustand von $[Re^{I}(CO)_3(bpy)(^{S\text{-}S}bpy)]^+$ wurde mittels Trajectory Surface Hopping in Kombination mit zeit-abhängiger Dichtefunktionaltheorie und einem Linear-Vibronic-Coupling-Modell untersucht. Die Ergebnisse zeigten ultra-schnelles Intersystem Crossing von den ursprünglich angeregten Singulett-Zuständen zu den Triplett-Zuständen. Anschließend wurden zwei unterschiedliche Typen von Trajektorien beobachtet, welche nach der Struktur des Komplexes klassifiziert werden können. Ein Typ zeigte signifikante Verlängerung der Schwefel-Schwefel-Bindung, der andere Typ zeigte Strukturen nahe an der Gleichgewichtsgeometrie. Optimierungen des T_1 Zustandes brachten zwei unterschiedliche Minima hervor, wobei eines eine verlängerte S-S Bindung zeigt ($T_{1,long}$) und das andere ähnlich zur Gleichgewichtsgeometrie ist ($T_{1,short}$). Mit dieser Erkenntnis wurde daraus geschlossen, dass die Dynamik im angeregten Zustand zur Population dieser beiden Minima führt, mit einer 90 $T_{1,long}$: 10 $T_{1,short}$ Verteilung. Durch Vergleich mit experimenteller Lumineszenz ist es möglich die beobachtete Emission von $[Re^{I}(CO)_3(bpy)(^{S\text{-}S}bpy)]^+$ der Phosphoreszenz vom $T_{1,short}$ aus zuzuordnen. Vom $T_{1,long}$ kann andereseits strahlungslos in den Grundzustand zurückgekehrt werden. Zusätzlich zeigt der $T_{1,long}$ lokale Anregung an den Schwefelatomen. Das bedeutet, dass rund 90% der angeregten Population in einen Zustand gelangen, in welchem hohe Elektronendichte an den Schwefelatomen zu finden ist und welcher daher als potentieller Anfangspunkt für folgenden PCET Reaktionen dienen kann. Deshalb kann $[Re^{I}(CO)_3(bpy)(^{S\text{-}S}bpy)]^+$ potentiell als Disulfid/Dithiol-Schalter in Redox-kontrollierten Reaktionen dienen.

Acknowledgments

First of all, I would like to sincerely thank Univ.-Prof. Dr. Dr. h.c. Leticia González who sparked my interest for theoretical chemistry way back during my bachelor studies. She is and has always been a great inspiration and role model as a strong woman in science and I thank her for the great opportunity to work in her group.

Another big Thank You goes to Dr. J. Patrick Zobel without whom I would not have lasted even one week in this challenge. A lot of patience, countless explanations and expertise from his side made it possible for me to learn and grow in a completely new scientific field for me. I would like to thank him for keeping up with me and all of my internal challenges and all the ups and downs of this thesis project.

I would also like to thank Dr. Markus Oppel for the great technical support and providing immediate help whenever I had computer problems.

I also want to thank my collaborators Franc Meyer, Manuel Oelschlegel, Shao-An Hua, Dirk Schwarzer, and Jan-Hendrick Borter for the rich discussions about the project.

I am very grateful to all the current and former members of the González research group who welcomed me so warmly into their team. Be it the communal lunch breaks, the relaxing coffee breaks or the super fun game nights, they always made me feel welcome and as part of the group. Without their never-ending support and uplifting spirit, this thesis would not be possible. I want to especially thank my office colleagues, Dóra Vörös, MSc. and Nadja Singer, MSc., for so many helpful tips and tricks. I could always turn to them with any questions, even with the smallest things. The stretching breaks, numerous conversations, cuddling with Amy and especially lots of laughter made every day at the office a good one.

Lastly, I want to thank my friends and family for their constant support. A special thanks goes to my mother for the endless calls at night, picking me up whenever I felt down. The amazing support of my parents made it possible to complete my studies without any major worries.

Abbreviations

1TDM one-electron transition density matrix

BOA Born-Oppenheimer approximation

CASSCF complete-active-space self-consistent field

CASPT2 complete-active-space second order perturbation theory

DFT density functional theory

ESE electronic Schrödinger equation

FC Franck-Condon

FWHM full-width at half-maximum

GGA generalized gradient approximation

HF Hartree-Fock

IC internal conversion

IR infrared

ISC intersystem crossing

KS Kohn-Sham

LDA local density approximation

LSDA local spin density approximation

LVC linear vibronic coupling

MCH molecular Coulomb Hamiltonian

MECP minimal energy crossing point

NAC non-adiabatic coupling

NTO natural transition orbital

PCET proton-coupled electron transfer

PES potential energy surface

SCF self-consistent field

SH surface hopping

SOC spin-orbit coupling

TDA Tamm-Dancoff approximation

TD-DFT time-dependent density functional theory

TDKS time-dependent Kohn-Sham

TDSE time-dependent Schrödinger equation

TISE time-independent Schrödinger equation

THF tetrahydrofuran

TRIR time-resolved infrared

ZORA zeroth-order regular approximation

Contents

1 Introduction

The switching capabilities of disulfide/dithiol motifs play an important role in many biochemical processes. Disulfide/dithiol interconversions are essential for redox control, charge storage, stability and formation of proteins in many biological systems.[1–7] A common representative of such disulfide motifs in nature are the members of the protein disulfide isomerase family.[4,5] Protein disulfide isomerase specifically is one of the most abundant proteins in the endoplastamtic reticulum, where it governs disulfide formation in polypeptides to facilitate correct protein folding. In the process, the disulfide of protein disulfide isomerase is reduced to the dithiol, which is then converted back to the disulfide by membrane-bound proteins via disulfide exchange reactions. Protein disulfide isomerase not only enables disulfide formation in proteins, but is also used to correct folding errors via disulfide isomerization.[3,5] In addition, disulfide/dithiol motifs play an essential role in antioxidant defense and redox regulation within the thioredoxin and thioredoxin reductase system. Herein, thioredoxin can act as singlet oxygen or hydroxyl radical scavenger, or reduce reactive oxygen species targets, that were oxidized by oxidative stress. Thioredoxin reductase is then used to recover the dithiol form of thioredoxin. Thus, this system plays an important role in the prevention of oxidative damage such as lipid and protein oxidation or DNA damage.[6,7]

Following the ongoing efforts to adapt such natural processes for industrial purposes, the group of Franc Meyer (University of Göttingen) developed a modified 2,2'-bipyridine (bpy) equipped with a disulfide moiety at the 3,3'-positions (Fig. 1a).[8] 2,2'-bipyridine is a versatile compound, often used as ligand in transition metal complexes. Further functionalizations at the bpy unit allow for a vast variety in electronic, steric or photophysical properties.[9] Within the research of the Meyer group[8] the potential for proton-coupled electron transfer (PCET) reactions was explored, by equipping the bpy with a disulfide/dithiol switch. This potentially allows for reversible double reduction through S-S bond breaking and subsequent double protonation to yield the dithiol. Such $2e^-/2H^+$ reactions could be immensely useful for PCET processes, especially in the framework of coordination chemistry. This newly designed dithiine 2,2'-$^{S\text{-}S}$bpy undergoes two-step electrochemical reduction at the sulfur atoms to yield the dithiolate. The reduction is accompanied by a rotation of the pyridine rings towards the separation of the

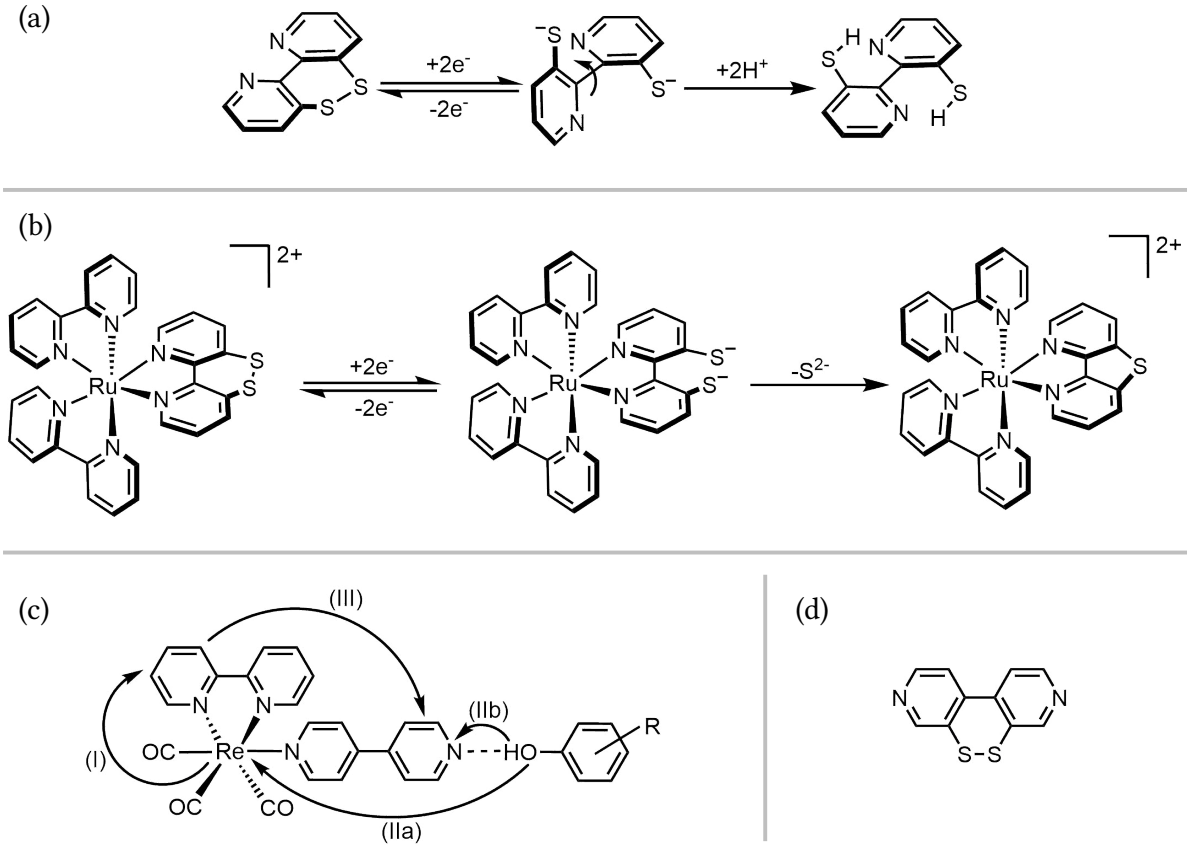

Figure 1: (a) [1,2]Dithiino[4,3-b:5,6-b']dipyridine undergoes two reduction steps inducing rotation around the central C-C bond, followed by double protonation.[8] (b) [Ru(2,2'-$^{S\text{-}S}$bpy)(bpy)$_2$]$^{2+}$ experiences S^{2-} extrusion upon double reduction.[10]. (c) PCET mechanism of *fac*-[(CO)$_3$Re^{I}(bpy)(4,4'-bpy)]$^{+}$.[11] (d) [1,2]Dithiino[3,4-c:6,5-c']dipyridine.[12]

sulfur atoms. In the presence of water the reduction is accompanied by protonation resulting in a dithiol. However, due to the twisting of the pyridine rings, the back-reaction to form the starting product is not possible, making the two-electron, two-proton transition irreversible.[8]

In an effort to improve the aforementioned system, the properties of 2,2'-$^{S\text{-}S}$bpy as ligand in a transition metal complex was explored.[10,13] A widely used photosensitizer [Ru(bpy)$_3$]$^{2+}$ [14] was equipped with the ligand 2,2'-$^{S\text{-}S}$bpy, yielding [Ru(2,2'-$^{S\text{-}S}$bpy)(bpy)$_2$]$^{2+}$ (Fig. 1b). Due to the chelating nature of the bipyridine moiety, twisting of the pyridine rings is hindered. Upon electrochemical reduction, the dithiolate is formed. However, due to the negative charges in close proximity a sulfide ion is eliminated in reductive conditions. This leads to the formation of a bipyridine bridged by a single sulfur atom ^{S}bpy. Such extrusion of a sulfide ion is irreversible, thus making extensive reduction of [Ru(2,2'-$^{S\text{-}S}$bpy)(bpy)$_2$]$^{2+}$ irreversible as well. This

transformation can be slowed down by temperature lowering. Below 273 K the redox process is reversible and the disulfide can be recovered by oxidation. Protonation of the dithiolate was not observed.[10]

PCET reactions have also been studied on photo-excited systems, such as the complex *fac*-$[(CO)_3Re^{I}(bpy)(4,4'\text{-bpy})]^+$ (Fig. 1c) proposed by the group of Leif Hammarström (Uppsala University).[11] The aforementioned complex undergoes one-electron-two-proton transfer with phenol derivatives upon excitation with light. Before the redox-process an association of the phenol derivative via a hydrogen bond to the peripheral N atom of the 4,4'-bipyridine unit occurs. The proposed PCET mechanism describes a metal to ligand charge transfer (MLCT) excitation from the rhenium to the equatorial 2,2'-bipyridine ligand after irradiation at 355 nm. Subsequently, an electron is transferred from the hydrogen-bonded phenol derivative to the rhenium center. Concertedly, the proton from the OH group is transferred to the associated pyridine unit. This in turn triggers interligand charge transfer from the equatorial bpy to the axial 4,4'-bpy ligand.[11]

Inspired by the successful PCET system of the Hammarström group[11], the group of Meyer wanted to extend upon the complex by introducing their sulfurated ligand. For that, the ligand had to be altered to replace the axially bound 4,4'-bipyridine ligand. The [1,2]Dithiino[3,4-c:6,5-c']dipyridine, herein called $^{S\text{-}S}$bpy (Fig. 1d), was previously characterized by Hall *et al.*[12] in its free form. Similar to 2,2'-$^{S\text{-}S}$bpy, the compound can be reduced twice at the sulfur atoms. Upon electrochemical reduction, first one electron is transferred to the disulfide moiety, which induces S-S bond elongation. This in turn facilitates further reduction and the second electron is transferred rapidly to yield the dithiolate.[12]

The journey of the sulfurated bipyridine lastly brings us to the complex investigated in this thesis. The group of Meyer synthesized a novel rhenium based complex equipped with the $^{S\text{-}S}$bpy ligand - $[Re^{I}(CO)_3(bpy)(^{S\text{-}S}bpy)]^+$ (Fig. 2). Their aim is to use this complex in PCET reactions similar to those proposed by the Hammarström group,[11] with the possibility of additional reduction and protonation on the sulfur atoms. This project is part of the priority program 'SPP 2102 - Light controlled reactivity of metal complexes' and is a collaboration between the groups of Franc Meyer (University of Göttingen), Dirk Schwarzer (Max-Planck-Institute, Göttingen), Oliver Wenger (University of Basel), and Leticia González (University of Vienna). The properties and characteristics of $[Re^{I}(CO)_3(bpy)(^{S\text{-}S}bpy)]^+$ will be explored

by synthetic and spectroscopic (Meyer, Schwarzer, and Wenger), and theoretical (González) methods. Since the goal is to use the complex in photo-induced reactions, the first step is to investigate its photophysical properties.

In the framework of this thesis, quantum-chemical methods will be used to investigate the excited state properties of $[Re^{I}(CO)_3(bpy)(^{S\text{-}S}bpy)]^+$. The ground state properties as well as the character of the initial excitation will be discussed. Afterwards, dynamic simulations will be conducted in order to follow the relaxation pathway of $[Re^{I}(CO)_3(bpy)(^{S\text{-}S}bpy)]^+$ upon optical excitation. Lastly, the theoretical findings and conclusions will be compared to experimental observables to propose a relaxation mechanism. The results within this thesis should lay the foundations for further experimental and theoretical research.

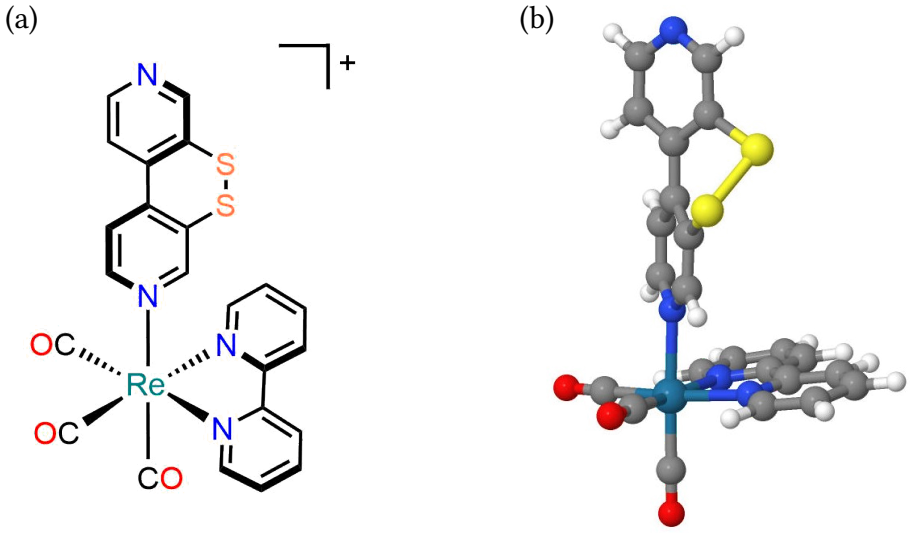

Figure 2: Structure of $[Re^{I}(CO)_3(bpy)(^{S\text{-}S}bpy)]^+$ (a) schematically and (b) in 3 dimensions with Re in turquoise, N in blue, C in gray, O in Red, S in yellow, and H in white.

2 Theoretical Background

2.1 Basic Concepts of Quantum Chemistry

The most common goal in quantum chemistry is finding an (approximate) solution to the time-independent Schrödinger equation (TISE)[15]

$$\hat{H}(r,R)\Psi(r,R) = E\Psi(r,R) \tag{1}$$

with the Hamilton operator $\hat{H}(r,R)$, the wave function $\Psi(r,R)$ and the total energy E. The wave function $\Psi(r,R)$ defines all quantum-mechanical information of a system with electronic coordinates r and nuclear coordinates R. The Hamiltonian $\hat{H}(r,R)$ describes the interactions of the electrons and nuclei of the system. For a system containing N electrons and M nuclei the Hamiltonian in atomic units ($\hbar = e = m_e = 4\pi\epsilon_0 = 1$) reads

$$\hat{H}(r,R) = \underbrace{-\frac{1}{2}\sum_{i=1}^{N}\nabla_i^2}_{\hat{T}_e} \underbrace{-\frac{1}{2}\sum_{A=1}^{M}\frac{1}{M_A}\nabla_A^2}_{\hat{T}_n} \underbrace{-\sum_{i=1}^{N}\sum_{A=1}^{M}\frac{Z_A}{|r_i - R_A|}}_{\hat{V}_{ne}} + \underbrace{\sum_{i=1}^{N}\sum_{j>i}^{N}\frac{1}{|r_i - r_j|}}_{\hat{V}_{ee}} + \underbrace{\sum_{A=1}^{M}\sum_{B>A}^{M}\frac{Z_A Z_B}{|R_A - R_B|}}_{\hat{V}_{nn}} \tag{2}$$

with M_A the mass, and Z_A the atomic number of nucleus A. The Hamiltonian comprises of the kinetic energy of the electrons ($\hat{T}_e$), the kinetic energy of the nuclei ($\hat{T}_n$), the electron-nuclear interaction ($\hat{V}_{ne}$), and the electron-electron ($\hat{V}_{ee}$) and nuclear-nuclear ($\hat{V}_{nn}$) repulsion.[16,17]

For systems with more than two particles the solution of the Schrödinger equation becomes everything but trivial. In order to investigate larger systems approximations have to be made. The most commonly applied approximation in quantum-chemistry is the Born-Oppenheimer approximation (BOA).[18] Within the BOA the nuclei of a system are considered as fixed, so that the electrons move in the field created by the nuclei. This is justified in view of the substantial mass difference of nuclei and electrons, and thus nuclei move much slower than electrons. Neglecting the movement of nuclei sets the kinetic energy of the nuclei $\hat{T}_n$ to zero and the nuclear-nuclear repulsion $\hat{V}_{nn}$ as constant. This allows us to simplify the total Hamiltonian to the electronic Hamiltonian yielding the electronic Schrödinger equation (ESE).

$$\hat{H}_{el} = \hat{T}_e + \hat{V}_{ne} + \hat{V}_{ee} \tag{3}$$

$$\hat{H}_{el}(r;R)\Psi_{el}(r;R) = E_{el}(R)\Psi_{el}(r;R) \tag{4}$$

The ESE can now be solved for fixed sets of nuclear coordinates. Thus, the electronic wave function and the electronic energy depend parametrically on the nuclear coordinates R. The total energy can than be computed from the electronic energy and the nuclear-nuclear repulsion:

$$E_{tot}(R) = E_{el}(R) + \hat{V}_{nn}(R) \ . \tag{5}$$

Solving the ESE for every set of nuclear coordinates yields a potential for the nuclear motion, the so-called potential energy surface (PES).[17,19]

2.2 Density Functional Theory (DFT)

The idea of density functional theory (DFT) is to describe the system through another quantity - the electron density $\rho(x)$, which is closely connected to the wave function as shown below. The electron density is a probability density that determines the probability of finding any of the N electrons in a certain volume element dr_i with arbitrary spin, whereas the other N-1 electrons are at arbitrary positions and with arbitrary spins in a certain state defined by Ψ.

$$\rho(x) = N \int \cdots \int |\Psi(x_1, x_2, \ldots, x_N)|^2 dx_2 \ldots dx_N \ , \tag{6}$$

with the variable x, which incorporate the coordinates (x,y,z) and the spin of the electrons.[20]

In 1964 Hohenberg and Kohn[21] postulated in their first theorem that the electronic ground state energy E_0 is completely defined by the ground state electron density ρ_0. Thus, the electronic ground state energy and its components can be rewritten as functionals of the ground state density:

$$E_0[\rho_0] = T[\rho_0] + V_{ee}[\rho_0] + V_{ne}[\rho_0]. \tag{7}$$

The second Hohenberg Kohn theorem states that this approach upholds the variational principle, i.e. the energy obtained from an approximated electron density is always an upper bound to the exact ground state energy.[20]

However, the exact form of the functionals introduced in equation (7) is not known. To tackle this problem, Kohn und Sham[22] suggested an approach to split the problem into a system of

non-interacting electrons and the corrections that arise from electron-electron interaction. The Hamiltonian for a non-interacting system is significantly simpler and reads

$$\hat{H}_S = -\frac{1}{2}\sum_i^N \nabla_i^2 + \sum_i^N V_S(r_i) \,, \tag{8}$$

with the effective potential $V_S(r)$ which includes electron-nuclear interactions. The eigenfunction of such a non-interacting Hamiltonian is simply a Slater determinant (hence the subscript S) comprised of one-electron functions ϕ_i called Kohn-Sham (KS) orbitals.

$$\Phi_S = \frac{1}{\sqrt{N!}}\begin{vmatrix} \phi_1(x_1) & \phi_2(x_1) & \dots & \phi_N(x_1) \\ \phi_1(x_2) & \phi_2(x_2) & \dots & \phi_N(x_2) \\ \vdots & \vdots & & \vdots \\ \phi_1(x_N) & \phi_2(x_N) & \dots & \phi_N(x_N) \end{vmatrix} \tag{9}$$

These KS orbitals are on their own eigenfunctions of the one-electron KS operator

$$\hat{f}^{KS}\phi_i = \epsilon_i\phi_i \,, \tag{10}$$

$$\hat{f}^{KS} = -\frac{1}{2}\nabla^2 + V_S(r) \,, \tag{11}$$

with the orbital energies ϵ_i and the effective potential $V_S(r)$. To connect this artificial system now to the real interacting system, the effective potential V_S is chosen as such, that the ground state electron density of the real system $\rho_0(r)$ is equal to the one of the non-interacting system $\rho_S(r)$.

Thus, the energy can be determined as a functional of the electron density and takes the following form:

$$E_0[\rho_0] = T_S[\rho_0] + J[\rho_0] + E_{XC}[\rho_0] + V_{ne}[\rho_0] \,. \tag{12}$$

In equation (12) $T_S[\rho_0]$ is the exact kinetic energy of a non-interacting system with the same electron density as the target system. $J[\rho_0]$ describes the classical Coulomb interactions of the electrons, $V_{ne}[\rho_0]$ is the nuclear-electronic interaction of the system, and $E_{XC}[\rho_0]$ is the so-called exchange correlation functional. The E_{XC} reads

$$E_{XC}[\rho_0] = (T[\rho_0] - T_S[\rho_0]) + (V_{ee}[\rho_0] - J[\rho_0]) \tag{13}$$

and includes the deviations of the non-interacting kinetic energy to the exact one and the non-classical electron-electron interaction terms.[20]

So far, no approximations were introduced, meaning that the ground state energy proposed in equation (12) is in principle exact. However, the exact form of the E_{XC} functional is not known, building the main hurdle of DFT. To this day the main challenge of DFT is finding the best approximation to E_{XC}. So far, no systematic improvement of the exchange-correlation functional was found, increasing the difficulty of finding the best form for E_{XC}.[20]

The simplest form of E_{XC} functionals stems from the local density approximation (LDA). Here the density is locally treated as a uniform electron gas. Thus, the exchange and correlation energies only depend on the electron density. For open-shell systems the spin has to be included resulting in the local spin density approximation (LSDA). Using LDA would result in the exact DFT energy for a uniform electron gas. In reality however, the molecules have little resemblance to a uniform electron gas.[23]

Since a real system does not have a constant electron density, the natural next step is to include the gradient of the electron density. This is done in so-called generalized gradient approximation (GGA) functionals. These GGA functionals now depend on the electron density and its gradient, as well as other parameters which are often empirically derived. The natural extension is to include even higher order derivatives of the electron density. Such expansions are called *meta*-GGA functionals.[23]

The last main group of E_{XC} functionals are so-called hybrid functionals. Such functionals exploit that in the Hartree-Fock (HF) formalism the form of the exchange energy is known. Using the KS orbitals instead of the HF orbitals within this formalism yields the exact exchange energy for the non-interacting system, as the KS Slater determinant is an exact representation of the non-interacting wave function. Combining this so-called HF exchange energy E_x^{HF} with the functionals discussed above (LDAs, GGAs or *meta*-GGAs) builds the basis of hybrid functionals. They typically include various components from different exchange and correlation formulas, weighted using semi-empirical parameters.[24]

2.3 Time-Dependent Density Functional Theory (TD-DFT)

As mentioned before, standard DFT is only able to compute the ground state density and the corresponding energies. In order to calculate electronic excited states, one has to use time-dependent density functional theory (TD-DFT). Runge and Gross[25] have shown that their

exists a similar formalism to the Hohenberg-Kohn theorem for the time-dependent case. The Runge-Gross theorem proves that there is a one-to-one correspondence between the electron density $\rho(r,t)$ and the external time-dependant potential $V_{ext}(r,t)$ for a system evolving from a fixed initial state Ψ_0. It follows, that the external potential is a unique functional of the time-dependent electron density. As $V_{ext}(r,t)$ fixes the Hamiltonian, also the Hamiltonian $\hat{H}(t)$ and the wave function $\Psi(t)$ are functionals of the density:[26,27]

$$V_{ext}(r,t) = V[\rho,\Psi_0](r,t) \longrightarrow \hat{H}(t) = \hat{H}[\rho,\Psi_0](t) \longrightarrow \Psi(t) = \Psi[\rho,\Psi_0](t)\ . \tag{14}$$

The evolution of the wave function can now be expressed by the time-dependent Schrödinger equation (TDSE)

$$i\frac{\partial\,|\Psi[\rho](t)\rangle}{\partial t} = \hat{H}[\rho](t)\,|\Psi[\rho](t)\rangle\ , \tag{15}$$

already including the density dependence. Similar to regular DFT, a now time-dependent KS approach is usually employed. A fictious system of non-interacting electrons based on a single-determinant wave function is defined following the time-dependent Kohn-Sham (TDKS) equation:

$$i\frac{\partial\varphi_i(r,t)}{\partial t} = \hat{h}^{KS}[\rho](t)\varphi_i(r,t)\ . \tag{16}$$

The time-dependent KS operator $\hat{h}^{KS}$ reads

$$\hat{h}^{KS}[\rho](t) = \underbrace{-\frac{\nabla^2}{2}}_{T_S} + V_{ext}(r,t) + \underbrace{\int dr'\frac{\rho(r',t)}{|r-r'|}}_{V_H[\rho](r,t)} + V_{XC}[\rho](r,t)\ , \tag{17}$$

with the kinetic energy of the non-interacting system $T_S(r,t)$, the time-dependent external potential $V_{ext}(r,t)$, the time-dependent Hartree potential $V_H[\rho](r,t)$ depending locally on the instantaneous density, and the time-dependent exchange-correlation functional $V_{XC}[\rho](r,t)$, which depends on the entire history of the electron density. The density of the non-interacting system

$$\rho(r,t) = \sum_{i=1}^{N}|\varphi_i(r,t)|^2\ , \tag{18}$$

is again defined to be equal to the electron density of the real system. As mentioned above, the exchange-correlation functional $V_{XC}[\rho](r,t)$ depends on the history of the electron density up to the time t. This however, makes it extremely difficult to even find approximations to it. Hence, in most applications of TD-DFT the adiabatic approximation is applied, where the exchange-correlation functional is supposed to only depend on the instantaneous density at

the time t called ρ_t. This allows us to use the ground state exchange-correlation functional of DFT $E_{XC}[\rho]$ at all times, yielding

$$V_{EX}[\rho](r,t) = \delta(t)\frac{\delta E_{XC}[\rho_t]}{\delta\rho_t(r)} \ . \tag{19}$$

The exact form of $E_{XC}[\rho_t]$ however, still remains unknown.[16,28]

A common approach for computing excitation energies in the framework of TD-DFT is linear-response TD-DFT . Herein, the response of the electron density to a small perturbation from a weak external field (i.e. excitation with light) is calculated. The first-order (linear) response can be written as

$$\delta\rho(r,t) = \int_{-\infty}^{t} dt' \int dr' \chi(r,t,r',t')\delta V_{ext}(r',t') \ , \tag{20}$$

with the density-density response function χ

$$\chi(r,t,r',t') = \left.\frac{\delta\rho(r,t)}{\delta V_{ext}(r',t')}\right|_{V_{ext,0}} \ . \tag{21}$$

Similarly, the response function of the non-interacting system is given as

$$\delta\rho(r,t) = \int_{-\infty}^{t} dt' \int dr' \chi_S(r,t,r',t')\delta V_S(r',t') \ , \tag{22}$$

with the $V_S(r',t')$ being the TDKS potential. Applying Fourier transformation to the equations (20) and (22) results in so-called Lehman representation of the response functions

$$\hat{\chi}(\omega) = \lim_{\eta\to 0^+}\sum_I \frac{\langle\Psi_0|\hat{\rho}|\Psi_I\rangle\langle\Psi_I|\hat{\rho}|\Psi_0\rangle}{\omega-(E_I-E_0)+i\eta} - \frac{\langle\Psi_0|\hat{\rho}|\Psi_I\rangle\langle\Psi|\hat{\rho}|\Psi_0\rangle}{\omega+(E_I-E_0)-i\eta} \ , \tag{23}$$

$$\hat{\chi}_S(\omega) = \lim_{\eta\to 0^+}\sum_{pq}(f_q-f_p)\frac{\varphi_p\varphi_p^*\varphi_q\varphi_q^*}{\omega-(\epsilon_q-\epsilon_p)+i\eta} \tag{24}$$

for the interacting and non-interacting systems respectively. Herein, Ψ_I is the wave function of state I with the excitation energy $\Omega_I = E_I - E_0$, $\hat{\rho}$ is the density operator, f_i is the occupation number of the KS spin orbital φ_i with the KS orbital energy ϵ_i. From equations 23 and 24 it is apparent, that the response function has a pole when the frequency equals either the exact excitation energy ($\hat{\chi}(\Omega_I) = \pm\infty$) or the difference of the KS eigenvalues ($\hat{\chi}_S(\epsilon_a - \epsilon_i) = \pm\infty$).[16,27]

On this basis, Casida[29] developed the well known pseudo-eigenvalue Casida equations:

$$\begin{pmatrix}\mathbf{A} & \mathbf{B}\\ \mathbf{B}^* & \mathbf{A}^*\end{pmatrix}\begin{pmatrix}\mathbf{X}\\ \mathbf{Y}\end{pmatrix} = \Omega\begin{pmatrix}\mathbf{1} & \mathbf{0}\\ \mathbf{0} & \mathbf{-1}\end{pmatrix}\begin{pmatrix}\mathbf{X}\\ \mathbf{Y}\end{pmatrix} \ , \tag{25}$$

from which the excitation energies Ω can be extracted. The matrices **A** and **B** read

$$A_{ia,jb} = \delta_{ij}\delta_{ab}(\epsilon_a - \epsilon_i) + 2\int dr \int dr' \varphi_i^*(r)\varphi_a(r) f_{Hxc}(r, r')\varphi_j^*\varphi_b \tag{26}$$

$$B_{ia,jb} = 2\int dr \int dr' \varphi_i^*(r)\varphi_a(r) f_{Hxc}(r, r')\varphi_j^*\varphi_b \ . \tag{27}$$

The exchange-correlation kernel f_{Hxc} in the adiabatic approximation is defined as

$$f_{Hxc} = \frac{1}{|r - r'|} + \left.\frac{\delta^2 E_{XC}[\rho]}{\delta\rho(r)\delta\rho(r')}\right|_{\rho=\rho_{[0]}} \ . \tag{28}$$

The vectors **X** and **Y** are the particle-hole and hole-particle excitations respectively.[26,27]

TD-DFT is commonly applied in the Tamm-Dancoff approximation (TDA)[30] (as is the case in this thesis), where the hole-particle excitations are neglected. This is achieved by setting the matrices **B** to zero, resulting in a simpler eigenvalue problem

$$\mathbf{AX} = \Omega\mathbf{X} \ . \tag{29}$$

The TDA achieves computational speed-up and can in some cases improve the description of the excited states.[26]

2.4 CASSCF and CASPT2

In addition to DFT, there exists a multitude of wave function based methods for obtaining the electronic structure information of a system. One of such methods is complete-active-space self-consistent field (CASSCF). In CASSCF, the orbitals of a system are divided into inactive, active and secondary (or virtual) orbitals. Inactive orbitals are considered to be doubly occupied in all configurations considered. The active orbitals are treated in a full configuration interaction type manner, where the wave function is a linear combination of all possible distributions of the chosen amount of electrons within the active space orbitals. Lastly, the secondary orbitals are considered to be empty. The number of orbitals and electrons within the active space has to be chosen beforehand and depends on the problem at hand. This multi-configurational treatment of the active space allows us to describe processes like bond breaking, which is not possible with DFT, as it only considers one electronic configuration.[31,32]

An approach to improve the energies of CASSCF computations comes with complete-active-space second order perturbation theory (CASPT2). Within CASPT2, the wave function obtained

by CASSCF is used as the zeroth-order wave function in a perturbation theory based approach. In perturbation theory, the Hamiltonian is split into a part where the solutions are known (here, the CASSCF wave function $\Psi_i^{(0)}$) labeled $\hat{H}_0$ and a perturbation on $\Psi_i^{(0)}$ labeled $\hat{H}'$. The energy contributions up to the second order perturbation can then be computed based solely on the known eigenfunctions of the zeroth order Hamiltonian $\hat{H}_0$. Thus, CASPT2 employs such perturbation correction to the energies based on the CASSCF results.[33,34]

2.5 Linear Vibronic Coupling Model (LVC)

In vibronic coupling theory[35] a model Hamiltonian based on the mass-frequency-scaled normal-mode coordinates $\mathbf{Q}$ is built:

$$\mathbf{H}(\mathbf{Q}) = (T_N + V_0(\mathbf{Q}))\,\mathbf{I} + \mathbf{W}(\mathbf{Q})\ , \tag{30}$$

with the kinetic energy operator T_N, the ground state potential energy of the reference state $V_0(\mathbf{Q})$, the idenity matrix $\mathbf{I}$ and the coupling matrix $\mathbf{W}(\mathbf{Q})$. The potential energy of other electronic states can now be computed on this basis via:

$$\mathbf{V}(\mathbf{Q}) = V_0(\mathbf{Q})\,\mathbf{I} + \mathbf{W}(\mathbf{Q})\ . \tag{31}$$

The reference PES (in most applications the ground state PES) of a system with L number of atoms is approximated by a harmonic oscillator with frequencies ω_i:

$$V_0(\mathbf{Q}) = \sum_{i=1}^{3L-6} \frac{\omega_i}{2} Q_i^2\ . \tag{32}$$

In the linear vibronic coupling (LVC) model the coupling terms are given up to the first-order (linear) terms as

$$W_{nm}(\mathbf{Q}) = \begin{cases} \epsilon_n + \sum_{i=1}^{3L-6} \kappa_i^{(n)} Q_i & \text{for} \quad n = m \\ \sum_{i=1}^{3L-6} \lambda_i^{(n,m)} Q_i & \text{for} \quad n \neq m \end{cases}\ , \tag{33}$$

where ϵ_n denote the vertical excitation energies of state n, while $\kappa_i^{(n)}$ and $\lambda_i^{(n,m)}$ are the intrastate and interstate coupling elements for the corresponding normal-mode coordinate Q_i respectively. The values for the different parameters in the coupling matrix can be obtained from reference quantum-chemical computations at the reference geometry.[36,37]

2.6 Transition Density Matrix Analysis

A useful tool to gather information about the character of a given one-electron excitation (as is the case with TD-DFT) is the analysis of the one-electron transition density matrix (1TDM). The 1TDM γ_{0I} between the ground state Ψ_0 and an excited state Ψ_I is given as

$$\gamma_{0I}(r_h, r_e) = N \int \cdots \int \Psi_0(r_h, r_2, \dots, r_N)\Psi_I(r_e, r_2, \dots, r_n) dr_2 \dots dr_N \ , \tag{34}$$

with the coordinates of the hole r_h in the ground state and the electron r_e in the excited state, respectively. From the 1TDM the hole and electron densities can be computed as follows:

$$\rho_h(r_h) = \int \gamma_{0I}(r_h r_e)^2 dr_e \tag{35}$$

$$\rho_e(r_e) \int \gamma_{0I}(r_h r_e)^2 dr_h \ . \tag{36}$$

Integrating these densities over all space yields Ω, the central quantity of transition density matrix analysis,

$$\Omega = \int \rho_h(r_h) dr_h = \int \rho_e(r_e) dr_e = \int \int \gamma_{I0}(r_h, r_e)^2 dr_e dr_h \ . \tag{37}$$

To analyze the electron-hole distribution of a given excitation, the system is partitioned into different fragments, chosen in most cases by the chemist upon chemical intuition. The charge transfer number from fragment A to fragment B is written as

$$\Omega_{AB} = \int_A \int_B \gamma_{I0}(r_h, r_e)^2 dr_e dr_h \ , \tag{38}$$

with integration over the volume elements of A and B. Ω_{AB} represents the probability of finding the hole on fragment A while the electron is on fragment B. The sum of all possible charge transfer numbers within the fragmentation equals Ω, which is 1 when considering only one-electron excitations.

Better visualisation of the excited state character is given by the natural transition orbitals (NTOs). The NTOs are obtained by a singular value decomposition of the 1TDM and lead to a representation of the 1TDM as follows:

$$\gamma_{0I}(r_h, r_e) = \sum_i \sqrt{\lambda_i} \psi_i^h(r_h) \psi_i^e(r_e) \ . \tag{39}$$

In equation (39) the 1TDM is represented as a sum over orbital pairs, where ψ_i^h and ψ_i^e are the NTOs representing the hole and electron component respectively, and the amplitude of the transition i is given by λ_i.[38,39]

2.7 Surface Hopping Dynamics

So far, no nuclear motion was included in the methods discussed. However,to simulate nuclear motion involves solving the TDSE (eq. 15) also for the nuclei, which is not feasible for polyatomic molecules in full dimensionality. Thus, mixed quantum-classical methods have been developed, where the electrons are treated quantum-mechanically, whereas nuclei are considered classical.

One of the most used mixed quantum-classical dynamics methods is surface hopping (SH), first proposed by Tully and Preston.[40] The main idea of SH is to simulate non-adiabatic effects while using classical motion of nuclei on adiabatic PES. This is achieved by allowing the trajectory to *hop* to another electronic state and continue propagating there. Repeating the dynamics for a set of multiple trajectories, should mimic the behaviour of a real wave packet. The wave packet could split at avoided crossings and continue on different PESs. By allowing different trajectories in SH to take different paths, such splitting is imitated. Therefore, non-adiabatic effects can be included in the dynamics.[40]

Nuclear Motion

In SH the nuclear motion is described through Newton's equation of motion

$$M_A \frac{\partial^2 R_A}{\partial t^2} = -\frac{\partial E_{el}}{\partial R_A} \,, \tag{40}$$

where the force on nucleus A is represented as the negative gradient of the electronic energy E_{el}. A common numerical integrator for Newton's equation is the so-called Velocity Verlet algorithm.[41,42] The algorithm computes the coordinates R and velocities v for the following time step based on the potential E_{el} of the active state β obtained by electronic structure theory of the current geometry:

$$R_A(t + \Delta t) = R_A(t) + v_A(r)\Delta t + \frac{1}{2MA}\nabla_A E_\beta(t)\Delta t^2 \tag{41}$$

$$v_A(t + \Delta t) = v_A(t) + \frac{1}{2M}\nabla_A E_\beta(t)\Delta t + \frac{1}{2M}\nabla_A E_\beta(t + \Delta t)\delta t \,. \tag{42}$$

Equations (41) and (42) show that the nuclear motion depends on the gradient of the electronic energy, i.e. the evolution of the electronic wave function. In turn, the electronic wave function parametrically depends on the nuclear positions. Hence, the nuclear and electronic evolution are intimately coupled.[16]

Electronic motion

The electronic wave function considered in SH is defined as a linear combination of basis functions which depend on the electronic coordinates r and parametrically on the nuclear coordinates $R(t)$

$$|\Psi(r, t; R(t))\rangle = \sum_{\alpha} c_{\alpha}(t) \, |\psi_{\alpha}(r; R(t))\rangle \ , \tag{43}$$

with time-dependent coefficients $c_{\alpha}(t)$. Inserting this expansion into the TDSE yields the equation of motion for the electrons, which in matrix notation reads (dropping the time dependencies for brevity):

$$\frac{\partial}{\partial t}\mathbf{c} = -\left[i\mathbf{H} + \mathbf{K}\right]\mathbf{c} \ . \tag{44}$$

In equation (44) the matrix elements of $\mathbf{H}$ and $\mathbf{K}$ are given as

$$H_{\alpha\beta} = \langle \psi_{\alpha}| \hat{H} \, |\psi_{\beta}\rangle \tag{45}$$

$$K_{\alpha\beta} = \langle \psi_{\alpha}| \frac{\partial}{\partial t} |\psi_{\beta}\rangle = \frac{\partial R}{\partial t} \langle \psi_{\alpha}| \frac{\partial}{\partial R} |\psi_{\beta}\rangle = v \langle \psi_{\alpha}| \nabla |\psi_{\beta}\rangle \ , \tag{46}$$

respectively. The matrix $\mathbf{K}$ is usually computed from the non-adiabatic couplings (NACs) $\langle \psi_{\alpha}| \nabla |\psi_{\beta}\rangle$, which are not available in density-functional based methods, such as the case for the dynamics performed within this thesis. Therefore, the time propagation of the coefficients $c(t)$ is performed in the so-called *local diabatization*[43] scheme. Here, $\mathbf{K}(t)$ is approximated from the wave function overlaps $\mathbf{S}$. The propagation of the wave function coefficients is then computed as

$$c(t + \Delta t) = \underbrace{\mathbf{S}(t, t + \Delta t)^{\dagger} \hat{\mathcal{T}} \exp\left[-\int_{t}^{t+\Delta t} \frac{i}{\hbar} \mathbf{S}(t, \tau)\mathbf{H}(\tau)\mathbf{S}(t, \tau)^{\dagger} d\tau\right]}_{\mathbf{P}(t + \Delta t, t)} c(t) \ , \tag{47}$$

with the time-ordering operator $\hat{\mathcal{T}}$, the propagator matrix $\mathbf{P}(t + \Delta t)$ and the overlap matrix

$$S_{\alpha\beta}(t, t + \Delta t) = \langle \psi_{\alpha}(t) | \psi_{\beta}(t + \Delta t)\rangle \ . \tag{48}$$

Here, the Hamiltonian matrix is diabatized via wave function overlaps, hence the name local diabatization scheme.[16]

Surface Hopping probabilities

Over an ensemble of trajectories, the active states should be chosen such that the fraction of trajectories in state β is equal to the electronic population of state β:

$$\frac{N_{\beta}(t)}{N_{traj}} = \frac{1}{N_{traj}} \sum_{i}^{N_{traj}} |c_{\beta}^{i}(t)|^2 \ . \tag{49}$$

If the electronic population $|c_\beta(t)|^2$ changes, a corresponding number of trajectories should hop to or from state β. For computing the hopping probabilities, the fewest-switches criterion[44] is used in most applications. It states, that equation (49) has to be achieved with the fewest hops possible. The individual probabilities for hopping from active state β to any target state α can then be computed as follows:

$$p_{\beta\to\alpha} = \left(1 - \frac{|c_\beta(t+\Delta t|^2}{|c_\beta(t)|^2}\right) \frac{\mathscr{R}[c_\alpha(t+\Delta t)P^*_{\alpha\beta}c_\beta(t)]}{|c_\beta(t)|^2 - \mathscr{R}[c_\beta(t+\Delta t)P^*_{\beta\beta}c_\beta(t)]} \,, \tag{50}$$

based on the propagator matrix $\mathbf{P}$. After computing all hopping probabilities, a random number ζ between 0 and 1 is drawn which dictates if a hop is performed:

$$\sum_{i=1}^{\alpha-1} h_{\beta\to i} < \zeta \leq h_{\beta\to\alpha} + \sum_{i=1}^{\alpha-1} h_{\beta\to i} \,. \tag{51}$$

If ζ falls into a certain interval of probabilities, a hop to target state α is initiated.[16,44]

Kinetic energy rescaling

After a successful hop to another electronic state, the kinetic energy of the system has to be adjusted in order to preserve the total energy, due to the difference in potential energy of the two states. The simplest way to adjust the kinetic energy is to rescale the complete velocity vector

$$v^{adjusted} = \sqrt{\frac{E_{total} - E_\beta}{E_{total} - E_\alpha}}\, v \,, \tag{52}$$

where E_{total}, E_α and E_β are the total energy, the energy of the old active state and the energy of the new active state, respectively. Another method is to only rescale the velocity components in the direction of the NAC vector. If there is not enough kinetic energy available for the adjustment, the hop is frustrated. After such a frustrated hop the kinetic energy can either be reflected by adjusting the complete velocity vector (used within this thesis) or the components in the direction of the NAC vector, or no reflection can be employed.[16,45]

Decoherence Correction

An inherent problem of SH is the over-coherence of the electronic populations during propagation. During the simulations, the electronic population is split over multiple electronic states. However, the electronic wave packet is propagated along a single trajectory determined by the gradient of the active state. Thus, electrons are propagated by the gradient of the active state, rather then the gradient of their current state. This leads to too much coherence and does not reflect physical behaviour. Therefore, decoherence correction has to be employed during the

simulation. This is commonly done in the *energy based decoherence* formalism.[46] Within this decoherence correction, the non-active populations are decayed over time, dependent on the kinetic energy. In addition, the population of the active state is adjusted accordingly, to not lose overall population.[16,47]

The *SHARC* approach

Within the work of this thesis, the surface hopping simulations were performed using the *SHARC* program package[48–50], which stands for *Surface Hopping including ARbitrary Couplings*. As the name suggests, this approach includes various different couplings in addition to non-adiabatic couplings, such as spin-orbit couplings (SOCs) or external fields (laser pulses). The total electronic Hamiltonian is thereby split into the standard electronic Hamiltonian, also called molecular Coulomb Hamiltonian (MCH), and the Hamiltonian which incorporates the additional couplings:

$$\hat{H}^{total} = \hat{H}^{MCH} + \hat{H}^{additional} \ . \tag{53}$$

However, most quantum chemical approaches do not provide eigenfunctions to the total Hamiltonian. To find approximate eigenfunctions, first a set of eigenfunctions of the MCH is computed. In the basis of these states the matrix elements can be calculated as

$$H^{MCH}_{\beta\alpha} = \langle \Psi^{MCH}_{\beta} | \hat{H}^{total} | \Psi^{MCH}_{\alpha} \rangle \ , \tag{54}$$

which builds the total Hamiltonian matrix in the MCH basis $\mathbf{H}^{MCH}$. This matrix can then be diagonalized by a unitary transformation to generate approximate eigenstates and eigenenergies of the total Hamiltonian in the diagonal representation

$$\mathbf{H}^{diag} = \mathbf{U}^{\dagger}\mathbf{H}^{MCH}\mathbf{U} \ , \tag{55}$$

$$|\Psi^{diag}_{\beta}\rangle = \sum_{\alpha} |\Psi^{MCH}_{\alpha}\rangle \, U_{\alpha\beta} \ . \tag{56}$$

The benefit of the diagonal representation is, that all state-to-state couplings are localized. Thus, the propagation is performed in the diagonal basis, whereas the quantum-chemical computations are performed in the MCH basis, with transformations in between. Both can then be used for different kinds of analysis.[49]

3 Computational Details

3.1 Electronic Structure Calculations

3.1.1 (Time-Dependent) Density Functional Theory

All quantum-chemical calculations were performed using the *ORCA4.2.1* program package.[51,52] The singlet ground-state structure of $[Re^{I}(CO)_3(bpy)(^{S\text{-}S}bpy)]^+$ was optimized using DFT with the PBE0[53] functional, the SARC-ZORA-TZVP[54] basis set for Re and the ZORA-def2-TZVP[55] basis set for the other elements (C, O, N, S, H). The D4[56] dispersion correction was employed. For the self-consistent field (SCF) calculations, the resolution-of-identity approximation (RIJ-COSX)[57], the Grid4 integration grid and tight convergence criteria (TightSCF) were used. Scalar relativistic effects were incorporated with the zeroth-order regular approximation (ZORA).[58] Vibrational frequencies were computed at every optimized geometry. When of interest, solvent effects were included using the SMD solvation model[59] with tetrahydrofuran (THF) as solvent. SMD is a universal continuum solvation model based on the full electron density of the solute interacting with an implicit description of the solvent. To determine the optimal method to describe the photophysics of $[Re^{I}(CO)_3(bpy)(^{S\text{-}S}bpy)]^+$ a number of different functionals were tested. For a Wigner ensemble of 50 geometries, 30 singlet and 30 triplet excited states were computed using TD-DFT. The functionals tested included PBE0, B3LYP[60], CAM-B3LYP[61], LC-BLYP[62], and M06-2X[63]. Additionally, the long-range correction parameters of LC-BLYP were reoptimized for $[Re^{I}(CO)_3(bpy)(^{S\text{-}S}bpy)]^+$ specifically, to obtain the customized functional LC-BLYP*.[64] The parameters employed are μ = 0.19, variable exchange = 85%, fixed HF exchange = 15%, and fixed DFT exchange = 0%.

The electronic excited states were computed using TD-DFT within the TDA[30] using the aforementioned functionals, the D4 dispersion correction[56] and the ZORA basis sets at the triple-zeta level. The resulting stick spectra were convoluted using Lorentzian functions and a full-width at half-maximum (FWHM) value of 0.25 eV.

PBE0 was deemed to best describe the system and is thus used throughout the following

computations. For the generation of a sampled absorption spectrum a total number of 550 geometries were sampled by a finite-temperature Wigner distribution[65,66] (T = 300 K) restricted to vibrational levels up to v = 15, including four rotational minima of $[Re^{I}(CO)_3(bpy)(^{S\text{-}S}bpy)]^+$ according to their relative population (see section 4.2). At each geometry the electronic ground state, 30 excited singlet states, 30 triplet states and the 120 corresponding spin-orbit coupled (SOC) states were computed, using quasi-degenerate perturbation theory[67] as implemented in *ORCA*. The resulting stick spectra were convoluted using Lorentzian functions with a FWHM of 0.1 eV.

Additionally, excited state geometry optimizations for the T_1 were carried out using PBE0. Single point calculations were carried out with PBE0, B3LYP, CAM-B3LYP, LC-BLYP, LC-BLYP*, M06-2X, and ωB97X-V[68].

A number of constrained geometry optimizations were carried out. One internal coordinate (distance, angle or dihedral angle) is set at a fixed value, whereas the remaining system is allowed to relax. A scan of different values of the dihedral angle C_{CO}-Re-$N_{s\text{-}s_{bpy}}$-$C_{s\text{-}s_{bpy}}$ was performed in the ground state. Additionally, various S-S bond lengths were scanned on the lowest-lying triplet PES.

Furthermore, minimal energy crossing point (MECP) calculations between the ground state S_0 and the lowest-lying triplet state T_1 were performed as implemented in *ORCA*.

The charge transfer characters of the excited states were analyzed with the *TheoDORE*[39] program package.

For visualisation of structures and orbitals *Jmol*[69] was used.

3.1.2 LVC Model

In addition to TD-DFT calculations, an analytical LVC model was set up to describe the PESs of the system.

The coupling terms were calculated by TD-DFT calculations on geometries displaced by ±0.05 units from the optimized ground state geometry for each of the 135 normal modes present in $[Re^{I}(CO)_3(bpy)(^{S\text{-}S}bpy)]^+$. There, $\kappa_i^{(n)}$ are obtained as numerical gradients and $\lambda_i^{(n,m)}$ are computed from the change in the wave-function overlaps. An LVC template for the singlet ground state,

15 singlet and 15 triplet excited states of the most stable rotamer of $[Re^{I}(CO)_3(bpy)(^{S\text{-}S}bpy)]^+$ was created. In addition the SOC elements were computed at the Franck-Condon (FC) geometry.

Absorption spectra, including 15 singlet and 15 triplet excited states, were calculated for a Wigner distribution of 10000 geometries using the parametrized LVC model potentials. The spectra were convoluted using Lorentzian functions with FWHM = 0.1 eV.

Additionally, geometry and crossing point optimizations have been conducted using the LVC model potentials within the *ORCA4.2.1* optimizer.

3.1.3 CASSCF / CASPT2

All CASSCF/CASPT2 calculations were performed in *OpenMolcas* Version 18.0.[70]

For reference, a number of geometry optimizations were conducted for the isolated ligand $^{S\text{-}S}$bpy using CASSCF. An active space containing 12 orbitals and 12 electrons was used (see Appendix A.1, Fig.A1). Optimizations of the T_1 minima were performed. Furthermore, constrained geometry optimizations of a range of fixed S-S bond lengths was conducted. All of these optimizations used the ANO-RCC-VDZP[71] basis set and the RICD[72] approach (resolution of identity technique with on-the-fly generated auxiliary basis sets based on the Cholesky decomposition method). At each of those CASSCF optimized geometries, a multi-state calculation using CASPT2 with an IPEA shift[73] of 0.25 eV was performed additionally. The multi-state computations included 4 singlet states and 3 triplet states for the respective spin manifold. An imaginary shift[74] of 0.1 eV was used to avoid problems with intruder states. In addition, the calculations were repeated using no IPEA shift for reference. The differences will be discussed in Appendix A.1 Figure A2, the main text will only discuss the computations with an IPEA shift of 0.25 eV. The PESs along the S-S scan obtained by CASSCF and CASPT2 were compared in Appendix A.1 Figure A3.

3.2 Non-adiabatic Excited State Dynamics

The non-adiabatic dynamics of $[Re^{I}(CO)_3(bpy)(^{S\text{-}S}bpy)]^+$ have been simulated using (SH)[40] with the *SHARC*[48–50] program package. Two sets of dynamics simulations were performed using different excited state potentials - the LVC model potentials and on-the-fly TD-DFT

calculated potentials.

3.2.1 On-the-fly TD-DFT/SH Dynamics

Based on the TD-DFT computed excited states of the Wigner ensemble of $[Re^{I}(CO)_3(bpy)(^{S\text{-}S}bpy)]^+$ an excitation window of 2.70 - 3.20 eV for the excited state dynamics was chosen. Initial conditions and initially populated states were chosen stochastically based on the oscillator strength of the excited states within the chosen energy window.[75] In total 101 trajectories were generated for the most stable rotamer of $[Re^{I}(CO)_3(bpy)(^{S\text{-}S}bpy)]^+$.

The simulations were started by instantaneous δ-pulse excitation into the stochastically chosen starting states. The trajectories were propagated for 100 fs with a nuclear time step of 0.5 fs and an electronic time step of 0.02 fs. A randomly selected amount of trajectories (60) were propagated for an additional 50 fs (150 fs total). Two example trajectories were propagated for a total of 200 fs.

An energy-based decoherence correction with a constant value of 0.1 a u was employed.[46] After a surface hop, the kinetic energy was adjusted by rescaling the velocity vectors. The surface hopping probabilities were computed based on wave-function overlaps.[76] A gradient selection was performed to speed up the computations, i.e. only gradients of states within ±0.5 eV of the active states were computed at each time step. This lead to the computation of roughly 20 gradients at each time step. Including all 61 gradients would be computationally much more expensive, increasing the wall-clock time of one time step by roughly 1 hour. Including only a selected amount of gradients however, allows hops only to states where the gradient was calculated. The simulations were performed with the *SHARC-ORCA* interface, where the energies and gradients of the electronic states were computed on-the-fly using TD-DFT using the PBE0 functional, the SARC-ZORA-SVP (Re) and ZORA-def2-SVP (C, O, N, S, H) basis sets and D4 dispersion correction, in *ORCA4.2.1*.

3.2.2 LVC/SH Dynamics

A second set of trajectories were simulated where the PESs were parametrized by the LVC model. A total of 992 initial conditions were generated based on LVC computed oscillator

strengths within the excitation window of 2.70 to 3.20 eV. The trajectories were propagated for 10 ps (10000 fs) with a nuclear time step of 0.5 fs and an electronic time step of 0.02 fs. Decoherence correction, surface hopping probabilities and rescaling was handled as mentioned above. In addition, the total energy of the system was damped by a factor of 0.99999 at each time step to simulate the energy transfer with the environment. The trajectories were stopped upon reaching the ground state (S_0) and propagating there for 20 fs, in order to hinder unrealistic hops back to excited states.

The choice of parameters for the LVC/SH dynamics are discussed in the Appendix A.2.

4 Results and Discussion

4.1 Choice of Computational Methods

Within the field of computational chemistry it is crucial to first find the best method to investigate the problem at hand. Many aspects, such as accuracy and computational cost have to be considered. This means, that for any new research question and/or system a search for the most viable computational method should be done beforehand. In the framework of this thesis, DFT and TD-DFT were the quantum-chemical methods of choice. DFT strikes a good balance between accuracy and efficiency and has proven to be applicable for various other transition metal complexes.[19,77] In order to validate the results obtained computationally, they are often compared to experimental observables. The absorption spectra are often used for comparison, when electronic excited states are of relevance, such as in this project. Thus, the experimental absorption spectrum was used as reference for choosing the optimal computational method.

In the framework of DFT the choice of functional is essential, as there is no systematic improvement between functionals. A number of well-established DFT functionals have been tested, namely B3LYP, CAM-B3LYP, LC-BLYP, PBE0, and M06-2X. In addition, the long-range correction parameters of LC-BLYP were optimized specifically for $[Re^{I}(CO)_3(bpy)(^{S\text{-}S}bpy)]^+$, further noted as LC-BLYP*. To account for scalar relativistic effects, the zeroth order regular approximation (ZORA) was applied together with specifically re-contracted basis sets SARC-ZORA-TZVP for Re and ZORA-def2-TZVP for all other elements. The D4 dispersion correction, RIJCOSX approximation, Grid4 integration and TightSCF was used (see Section 3.1). All of these parameters were kept constant for each functional. Solvent effects were included using the SMD solvation model with THF as solvent as implemented in *ORCA*. However during the testing phase, due to a bug in the implementation of SMD in *ORCA4.2.1*, solvent effects were only included in the DFT calculation of the ground state and not during the TD-DFT computations of the excited states. Since, this happened during all reference calculations, the different functionals can still be compared. The issue was resolved at later computations and the usage of a solvation model will be discussed separately below.

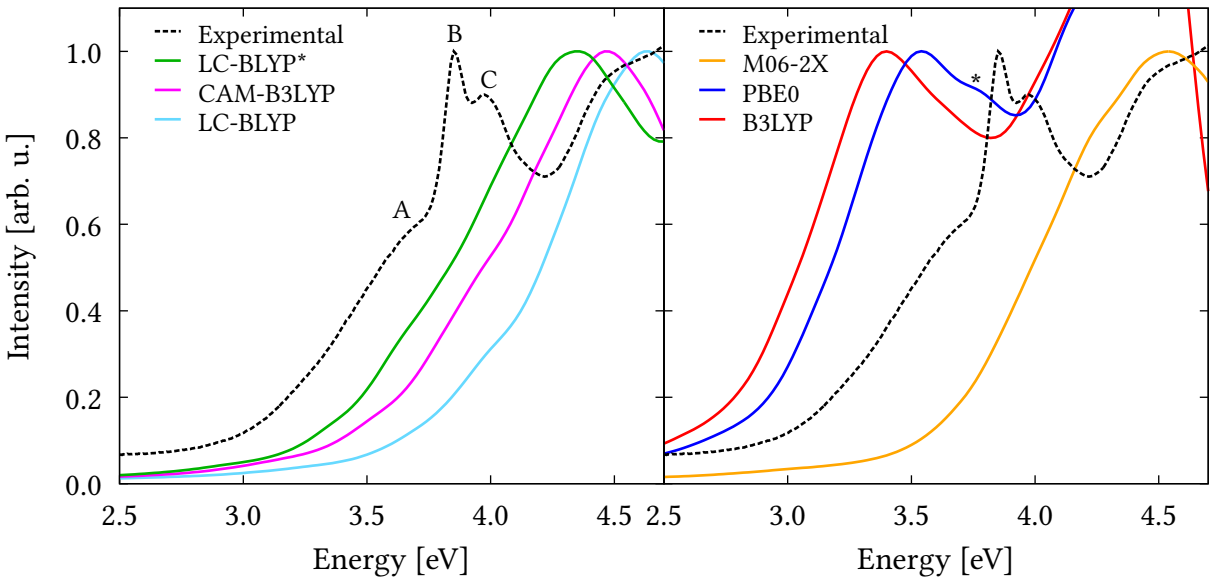

Figure 3: Experimental absorption spectrum[78] (black, dashed) in comparison to simulated absorption spectra calculated using different DFT functionals.

For a set of 50 geometries from a Wigner sampling of the optimized reference geometry (starting from the crystal structure), the 30 lowest-lying singlet excited states were computed using TD-DFT and the above-mentioned parameters. The resulting stick spectra were convoluted using Lorentzian functions with a value of FWHM = 0.25 eV to yield a simulated absorption spectrum. This procedure was repeated for every functional mentioned above. The resulting spectra are shown in Figure 3 together with the experimental absorption spectrum, which was measured in THF.

As can be seen, the experimental spectrum[78] shows a pre-band shoulder at 3.6 eV (A) and a bright absorption band split into two peaks at 3.85 eV (B) and 3.97 eV (C) respectively (marked in Fig. 3 left). Compared to the experimental reference, the long-range corrected functionals, CAM-B3LYP, LC-BLYP and LC-BLYP*, as well as M06-2X show one broad blue-shifted absorption band. Herein, the LC-BLYP* functional poses the best fit with an approximate difference of 0.5 eV. The two widely used functionals B3LYP and PBE0 show a red-shifted absorption band compared to the experimental band. PBE0 comes closest to the experimental values with an approximate deviation of 0.35 eV. In addition, the absorption band obtained from PBE0 computations is broader and shows a small shoulder after its peak (marked with * in Fig. 3 right), similar to the split band of the experiment. Due to the best accordance with the experimental absorption spectrum, PBE0 was chosen as DFT functional for all upcoming computations.

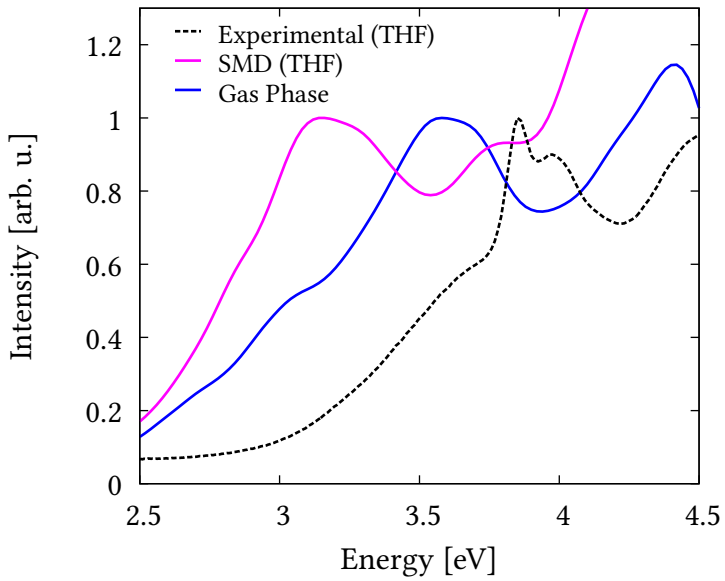

Figure 4: Comparison of computed absorption spectrum of $[Re^{I}(CO)_3(bpy)(^{S\text{-}S}bpy)]^+$ with no solvent effects (gas phase, blue), using the SMD solvation model with THF (magenta), and the experimental spectrum in THF[78] (black, dashed).

Next, the necessity of using an implicit solvation model was explored. For this, two absorption spectra were computed as described above at the PBE0/D4/SARC-ZORA-TZVP (Re), ZORA-def2-TZVP (C, O, N, S, H) level of theory, one without any solvent effects (gas phase) and one with the now correctly applied SMD solvation model with THF as solvent. Figure 4 shows the aforementioned computed spectra together with the experimental spectrum (measured in THF).

The shape of the gas phase spectrum is in good agreement to the experimental findings with a pre-band shoulder and a broad absorption band. The gas phase spectrum is red-shifted in comparison to the experimental THF spectrum, with deviations ranging from 0.25 eV (main absorption band) to 0.60 eV (pre-band shoulder). The computed absorption spectrum including solvent effects shows a broad bright absorption band at around 3.0 eV and a small shoulder followed by an increase in intensity at the high energy range of the spectrum (3.7 eV). There are two possible cases for the assignemnt of the peaks to the experimental spectrum:

1. The brighter absorption band at 3.14 eV corresponds to the shoulder seen at 3.60 eV in the experimental spectrum and the smaller band at 3.76 eV can be assigned to the main absorption band of the experimental spectrum (3.85 eV - 3.97 eV). This scenario results in deviations

ranging from 0.1 eV to 0.5 eV.

2. The bright absorption band at 3.14 eV also corresponds to the bright absorption band of the experimental spectrum (3.85 eV - 3.97 eV). The second absorption band could then be attributed to features at higher energies, not regarded in this study. The resulting differences are about 0.7 eV.

Regardless of the assignment, the gas phase and the solvated computed spectra both show red-shifted energies compared to the experimental values, with deviations in a similar range. Thus, it can be concluded that the gas phase spectrum is sufficient in describing the excited state properties of $[Re^{I}(CO)_3(bpy)(^{S\text{-}S}bpy)]^+$ and solvent effects do not need to be included in the following calculations. This allows for using the *SHARC-ORCA* interface for dynamics simulations, as it would not be capable of including implicit solvent effects, because excited state gradients with implicit solvents are not implemented in *ORCA4.2.*.

To summarize, the best functional to describe $[Re^{I}(CO)_3(bpy)(^{S\text{-}S}bpy)]^+$ was established to be PBE0. Furthermore, gas phase calculations are sufficient in describing the excited state properties of the complex. The level of theory used in the following sections is therefore PBE0/D4/SARC-ZORA-TZVP (Re), ZORA-def2-TZVP (C, O, N, S, H) for geometry optimizations and static calculations. The TD-DFT/SH dynamics are therefore performed using PBE0, D4 and SARC-ZORA-SVP (Re), ZORA-def2-SVP (C, O, N, S, H).

4.2 Ground State Chemistry

Next, the ground state properties of $[Re^{I}(CO)_3(bpy)(^{S\text{-}S}bpy)]^+$ were explored. Starting from the crystal structure, a geometry optimization at the PBE0/D4/SARC-ZORA-TZVP (Re), ZORA-def2-TZVP (C, O, N, S, H) level of theory was performed. The optimized ground state geometry is also referred to as the FC geometry. After the optimization the question arose, whether the $^{S\text{-}S}$bpy ligand can rotate along the Re-N bond. For this purpose, a set of constraint geometry optimizations were run, where the dihedral angle (C_{CO}-Re-$N_{^{S\text{-}S}bpy}$-$C_{^{S\text{-}S}bpy}$) determining the relative position of the ligand (marked red in Fig. 5a), was fixed and all other internal coordinates were allowed to relax. These optimizations were performed for dihedral angles from 0 to 360° in 25 steps. The results of this relaxed surface scan are shown in Figure 5b.

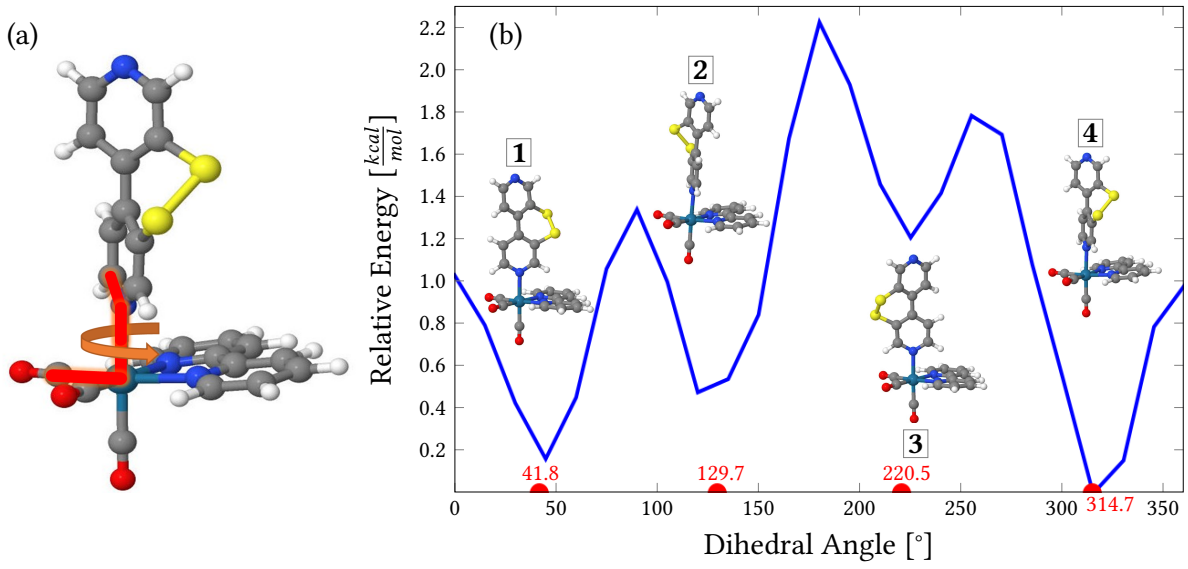

Figure 5: (a) Structure of $[Re^{I}(CO)_3(bpy)(^{S\text{-}S}bpy)]^+$, rotation along indicated dihedral angle (C_{CO}-Re-$N_{s\text{-}s_{bpy}}$-$C_{s\text{-}s_{bpy}}$) (red) shown. Re in turquoise, N in blue, C in gray, O in Red, S in yellow, and H in white. (b) Relaxed surface scan along the indicated dihedral angle for varying values. Energies shown relative to lowest total energy in kcal/mol. Optimized geometries of the four rotamers (1-4) are shown alongside their respective minimum, with the exact dihedral angles indicated by the red half-circles and the respective values in red.

The scan shows four local minima along the rotation of $^{S\text{-}S}$bpy, located at dihedral angles of approximately 45°, 120°, 225°, and 315°. The energy barriers connecting the minima lie between 0.6 to 1.7 kcal/mol, thus making all minima accessible at room temperature. Subsequent unconstrained geometry optimizations were conducted to locate the exact minimal structures. The exact dihedral angles of the minima are 41.8°, 129.7°, 220.5°, and 314.7° respectively. The optimized structures of the four rotamers (**1-4**) are shown besides their corresponding minimum in Figure 5.

In order to determine the distribution across those four minima at equilibrium, their relative populations were determined according to a Boltzmann distribution. The Boltzmann distribution is given as

$$P_m(T) = \frac{\exp(-\frac{E_m}{k_B T})}{\sum_m \exp(-\frac{E_m}{k_B T})}, \tag{57}$$

with $P_m(T)$ as the population of minimum m at the temperature T, E_m as the energy of minimum m, and k_B the Boltzmann constant ($1.98 \cdot 10^{-3}$ $\frac{\text{kcal}}{\text{mol}\cdot\text{K}}$). The temperature was chosen to be approximately room temperature, 300 K.

Table 1 depicts the relative energies of the four rotamers, where the lowest-energy one (rotamer **4**) is set to zero, together with their corresponding Boltzmann populations. The lowest energy rotamer **4** is populated by 44%, making up almost half of the population. The other three rotamers **1-3** include the remaining 56%.

In order to mimic the variety of geometries present in a real sample of $[Re^{I}(CO)_3(bpy)(^{S\text{-}S}bpy)]^+$, Wigner sampling was performed. Based on the optimized structures of the four rotamers a number of geometries shown in Table 1, in accordance to their relative population, was created using restricted, finite-temperature Wigner sampling with a temperature of 300 K. This Wigner ensemble of 550 geometries was then used to represent a solution of $[Re^{I}(CO)_3(bpy)(^{S\text{-}S}bpy)]^+$ at room temperature for excited state calculations.

Table 1: Relative energies [kcal/mol], Boltzmann population [%], and number of sampled geometries of the four rotamers of $[Re^{I}(CO)_3(bpy)(^{S\text{-}S}bpy)]^+$.

Rotamer	Relative Energy [$\frac{kcal}{mol}$]	Population [%]	Number of Sampled Geometries
1	0.24	30	165
2	0.45	21	116
3	1.33	5	27
4	0.00	44	247

4.3 Absorption Spectra

$[Re^{I}(CO)_3(bpy)(^{S\text{-}S}bpy)]^+$ is intended for use in photo-induced reactions. This means its excited state properties are very important. In particular, determining the character of the excited states at different excitation wavelengths is essential. For this reason, a simulated absorption spectrum was created based on the aforementioned Wigner ensemble using TD-DFT at the PBE0/D4/SARC-ZORA-TZVP (Re), ZORA-def2-TZVP (C, O, N, S, H) level of theory. The 30 lowest-lying singlet and triplet states were computed, as well as the 120 corresponding spin-orbit coupled states. The ensemble spectrum was created by convoluting the stick spectra from each geometry with Lorentzian functions with a FWHM value of 0.1 eV.

Figure 6a shows the computed absorption spectra in the spin-free (blue) representation, i.e.

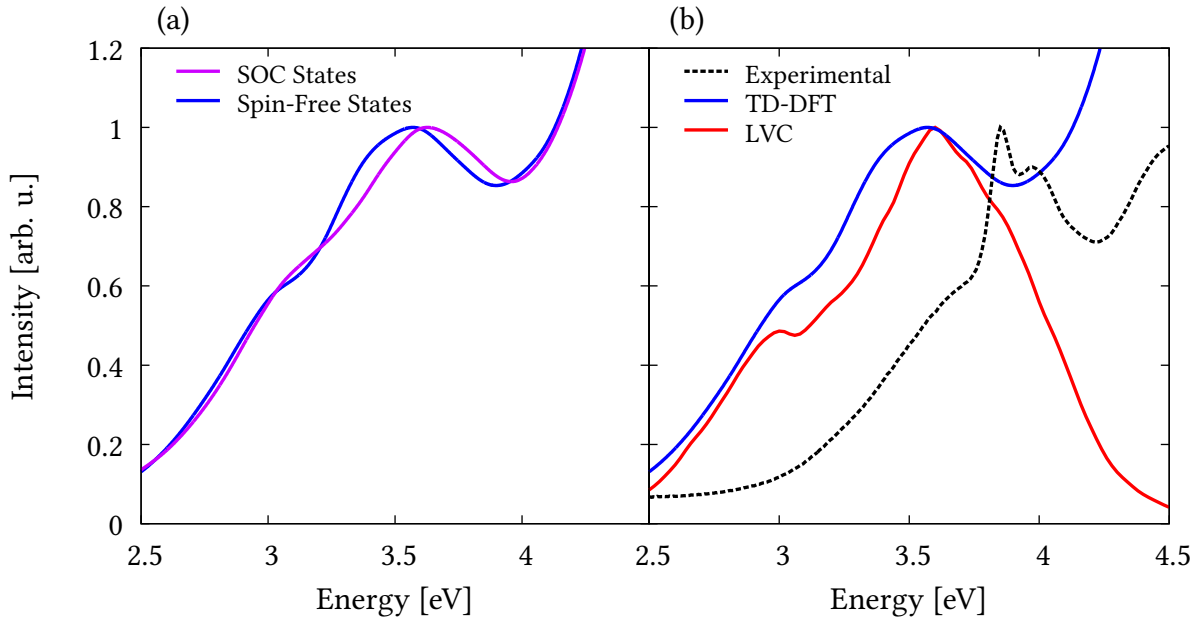

Figure 6: (a) Sampled absorption spectrum generated from spin-free states (blue) and spin-orbit coupled (SOC) states (magenta). (b) Experimental absorption spectrum[78] (black, dashed) together with the simulated sampled absorption spectra calculated with TD-DFT (blue) and with the parametrized LVC model potentials (red), in the spin-free representation.

only allowing excitations to singlet states, and in the spin-orbit coupled basis (magenta), where states are of mixed spin. The spectra generated from spin-free and spin-mixed states show only minor differences. The overall shape of the spectrum is very similar for both representations. The spectrum generated from SOC states shows a small shift to higher energies of 0.06 eV with respect to the spin-free spectrum. Looking at individual SOC matrix elements reveals relatively large values between 100 to 600 cm^{-1} for higher excited singlet and triplet states (see Appendix A.3, Table A1 and A2). Thus, mixing of states is allowed, but the excitation energy of bright states seems to not be influenced much. Later on, during transition density matrix analysis, only the spin-free states can be considered. Thus, only the spectrum generated from spin-free states will be further discussed. Since the differences between SOC and spin-free representation are minor, only negligible errors are made in this consideration.

In addition to TD-DFT computations, an LVC model potential was parametrized (see section 3.1.2). The LVC model can only encompass a single rotamer, since large geometric displacements are prohibited by the steep potentials in LVC. In the subsequent dynamics simulations only rotamer **4** will be considered due to time limitations. Thus, the model was based on the lowest-energy rotamer **4**. For validation, a second model was parametrized based on the second lowest

rotamer **1**, which only showed minor differences in the absorption spectrum to rotamer **4** (see Appendix A.4, Fig. A6). The singlet ground state, 15 singlet excited states, and 15 triplet states were incorporated into the model. To generate an absorption spectrum based on the LVC potentials, a Wigner ensemble of 10000 conformers of rotamer **4** was created. For each geometry, the respective stick absorption spectrum was calculated and then convoluted using Lorentzian functions and a FWHM of 0.1 eV. The spectra based on TD-DFT calculations and the LVC model potential compared to the experimental data are shown in Figure 6b.

The experimental absorption spectrum shows three distinct features within the energy range of 2.0 - 4.5 eV - a shoulder at 3.6 eV and an absorption band split into two peaks at 3.85 and 3.97 eV respectively. Both the TD-DFT and LVC computed spectra show a similar structure, including a pre-band shoulder and a broad bright band. However, the splitting into two peaks is not seen in the computed spectra. The decrease in intensity at 3.8 eV in the LVC spectrum originates from the smaller number of excited states computed compared to the TD-DFT spectrum, thus only the low-energy region is described. For the LVC spectrum only 15 singlet states and triplet states were considered, whereas TD-DFT incorporated 30 excited states each. The deviations made by our computational models range from 0.6 eV for the shoulder to 0.3 eV for the bright absorption band. Overall, our chosen computational methods were able to reproduce the features of the experimental absorption spectrum with moderate deviations of 0.3 - 0.6 eV. Thus, our models were deemed to be sufficient to describe the electronic transitions within $[Re^{I}(CO)_3(bpy)(^{S\text{-}S}bpy)]^+$ and dynamics simulations were conducted at this level of theory.

In addition to estimating the errors of the chosen computational model, the absorption spectrum can be further analyzed in terms of the character of excitation at different wavelengths. For this purpose, a transition density matrix analysis was performed using the *TheoDORE* package.[39]

For this, $[Re^{I}(CO)_3(bpy)(^{S\text{-}S}bpy)]^+$ was divided into five fragments, defining the following components (Fig. 7a): The central rhenium atom as M (purple), the three carbonyl ligands as L^{CO} (blue), the 2,2'-bipyridyl ligand as L (green), the two sulfur atoms as S (yellow), and the 4,4'-bipyridyl core of $^{S\text{-}S}$bpy as L^{S} (red). Taking into account all five fragments yields 25 possible excitation characters (Fig. 7b). Throughout this thesis, the fragment location of the hole will be written before the location of the electron. This is followed either by CT (charge transfer), when hole and electron fragments differ from each other, or by loc (local excitation) in cases where the hole and electron are located on the same fragment (or MC for metal centered where

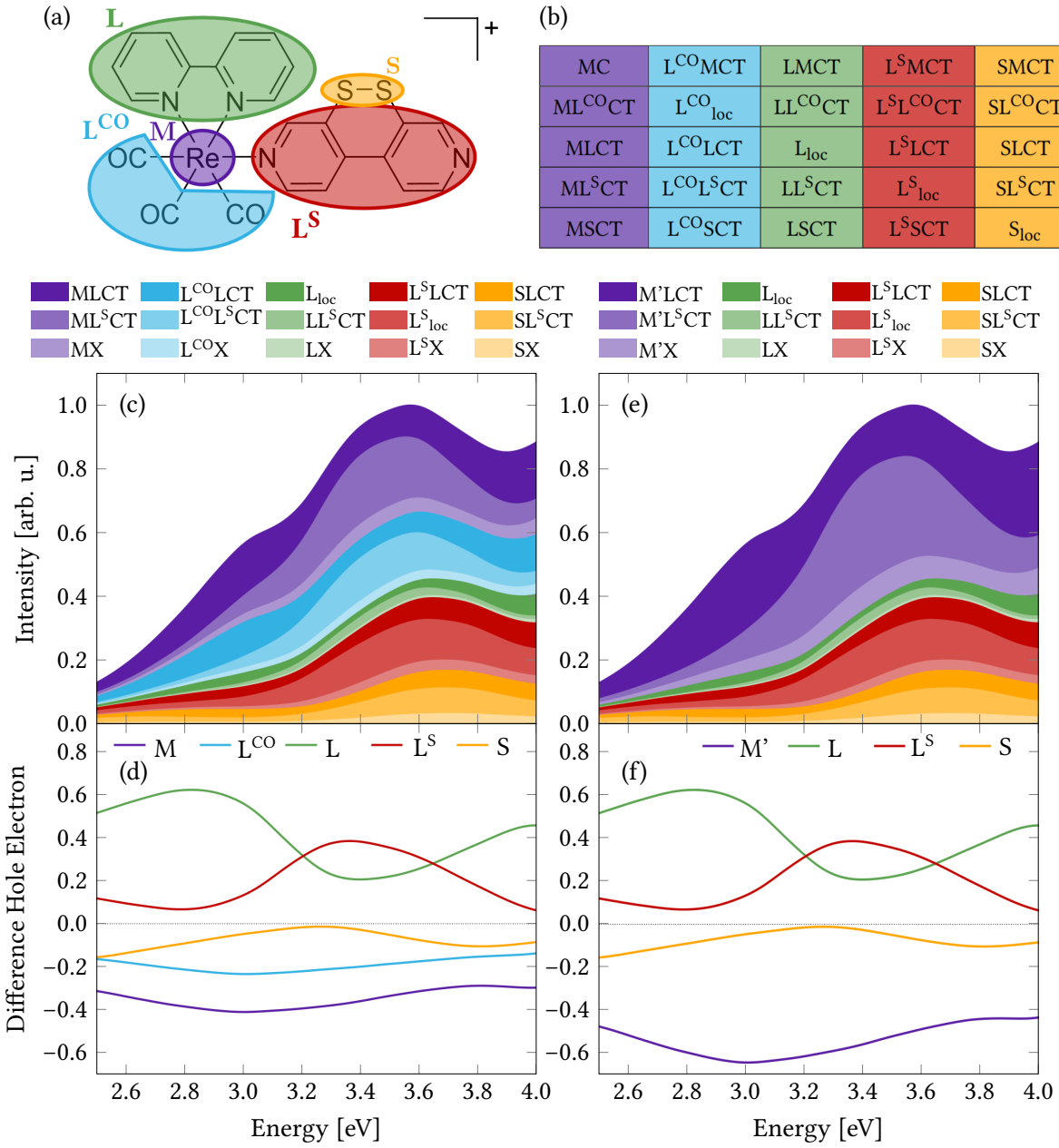

Figure 7: (a) Fragment partition of $[Re^{I}(CO)_3(bpy)(^{S\text{-}S}bpy)]^+$. (b) Characterization of possible excited state characters. CT denotes charge transfer, loc denotes local excitation. (c) TD-DFT computed absorption spectrum divided into the contribution of the excited state characters. Most important characters given explicitly. *X* denotes the sum of all contributions not explicitly given. (d) Difference hole and electron contribution on the specific fragments. Positive values correspond to dominating electron contribution on the fragment, whereas negative values indicate predominant hole components. Charge flow during excitation happens from negative to positive values. (e) Contributions of the excited state characters and (f) difference hole electron population for combined M and L^{CO} fragments as M'.

hole and electron are located at the Re). In the following figures, only the most prominent character contributions will be explicitly given. The remaining contributions will be summed up and denoted as *AX*, where *A* is the hole fragment and *X* the remaining electron fragments (for example *MX* in Figure 7 contains MC, $ML^{CO}CT$ and MSCT).

Dividing the absorption spectrum into the excited state characters gives insight into the character of the electronic states as a function of the excitation energy. Figure 7c shows that the character of the excited states has a variety of different contributions throughout the whole energy window. In literature the character of the excited states of rhenium tricarbonyl diimine complexes is usually assigned to pure MLCT to the equatorial diimine ligand.[11,79,80] In the case of $[Re^{I}(CO)_3(bpy)(^{S\text{-}S}bpy)]^+$ a mix of different contributions, also including L^S, is seen.

The most prominent character contributions show charge transfer either to the 2,2'-bpy ligand (L) or the 4,4'-$^{S\text{-}S}$bpy ligand (L^S). The rhenium metal center and the three CO ligands behave very similarly over the whole energy range and almost act like one fragment with similar relative contributions of *AX*CT where *A* is either M or L^{CO} an *X* is the hole fragment. This is better seen in the electron-hole difference population (Fig. 7d), where the curves for M and L^{CO} are almost parallel. The electron-hole difference population is computed as the sum of hole contributions subtracted from the sum of electron contributions on a given fragment. Hence, positive values indicate predominant electron contribution on that specific fragment, whereas negative values mark mostly hole contribution. This behaviour of the metal center and the CO ligands has been shown before for similar tricarbonyl rhenium complexes.[79,81,82] Thus, all excitations from the metal center will simultaneously incorporate excitation from the CO ligands. We will denote this $Re(CO)_3$ fragment as M' in the following discussions (Fig. 7e and f).

In the lower energy range (2.6 - 3.2 eV) of the absorption spectrum, where the shoulder is located, the excitation character is mostly charge transfer from M' to L, with roughly 48% M'LCT. The electron component is mainly located on the 2,2'-bpy ligand. This can be seen in Figure 7d and f, as L shows the highest positive values in that region.

When going to higher excitation energies (> 3.2 eV), the character shifts and M'L^SCT, M'LCT, as well as $L^S{}_{loc}$ transitions become predominant, with roughly 38%, 16% and 13% respectively. The remaining 33% are evenly spread over the other contributions, not exceeding 5%. In the range of the absorption band between 3.2 and 3.6 eV, the electron is mainly located at the L^S fragment,

however there is still charge flow to L. The character is therefore a mixture of M'L^{S}CT, L$^{S}_{loc}$ and M'LCT at the bright absorption band. The sulfur atoms only play a minor role within the electronic transitions in the energy range of 2.5 to 4.0 eV, thus indicating little relevance in the absorbance behaviour of $[Re^{I}(CO)_3(bpy)(^{S\text{-}S}bpy)]^{+}$.

Overall it can be said, that the metal center M and the carbonyl ligands CO function as electron donors within the absorbance energy range of 2.5 to 4.0 eV, whereas the two ligands L and L^{S} are electron acceptors. The predominant electron fragment is dependent on the excitation wavelength. This hints at the possibility of influencing the excited state behaviour of $[Re^{I}(CO)_3(bpy)(^{S\text{-}S}bpy)]^{+}$ by changing the excitation wavelength.

4.4 Triplet Optimization ($T_{1,long}$)

After absorption at 370 nm (3.35 eV), $[Re^{I}(CO)_3(bpy)(^{S\text{-}S}bpy)]^{+}$ shows luminescence at 573 nm (2.16 eV).[78] For rhenium complexes such luminescence generally stems from phosphorescence, due to their ability to populate the triplet manifold. The low emission energy (2.16 eV) and long emission rates (270 ns) also indicate phosphorescence for this complex.

In order to understand this experimental phosphorescence, the minimum of the lowest-lying triplet state has to be optimized first. Starting from the Franck-Condon geometry, an excited state geometry optimization using PBE0/D4/SARC-ZORA-TZVP (Re), ZORA-def2-TZVP (other)

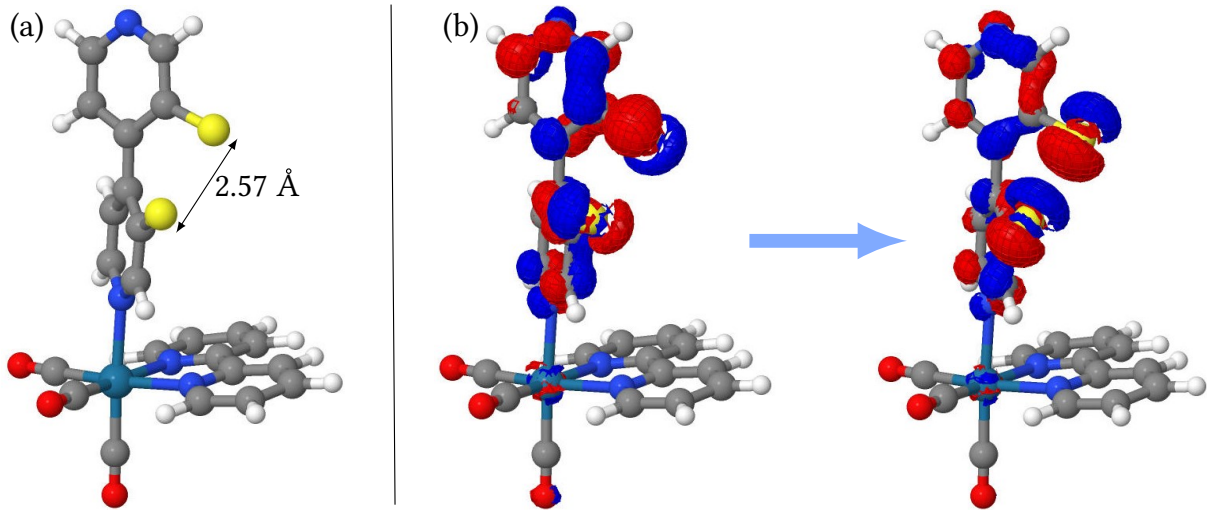

Figure 8: (a) Structure of $T_{1,long}$. (b) Natural transition orbitals of the S_0 - T_1 transition at $T_{1,long}$ geometry from left (hole) to right (electron), obtained by PBE0.

for the first excited triplet state was conducted.

The geometry of the resulting T_1 minimum is shown in Figure 8a. A large elongation of the S-S bond length from 2.05 Å at the FC geometry to 2.57 Å at this minimum geometry is seen. Thus, this minimum will be called $T_{1,long}$. The energy gap of $T_{1,long}$ to the ground state S_0 is 0.56 eV. Compared to the experimental phosphorescence energy of 2.16 eV, this differs by 1.60 eV.

In an effort to improve the prediction of the emission energy, single point calculations of the $T_{1,long}$ geometry with different functionals were performed. The results are shown in Table 2. Using long-range corrected functionals (CAM-B3LYP, LC-BLYP, LC-BLYP*, and wB97X-V) improves the predicted emission energy slightly. Other widely used functionals (B3LYP, M06-2X, PBE) did not yield a significant improvement to PBE0. Thus, none of the results are satisfactory in describing the experimental observations, which indicates that this minimum might not be the one responsible for the emission seen experimentally.

Looking at the excited state character of $T_{1,long}$ and its natural transition orbitals (Fig. 8b) one sees almost exclusive local excitation at $^{S\text{-}S}$bpy. More precisely, an excitation from a π orbital to a σ^* orbital of the S-S bond, with contributions of the neighbouring π-system of the 4,4'-bipyridyl moiety on both the hole and electron component, is seen. The excited state character consists of 62% S_{loc}, 10% SL^SCT, 22% L^SSCT, and 5% L^Sloc. However, the broad and structurless long-lived emission of Re-complexes is typically assigned to MLCT states.[79]

Table 2: S_0-T_1 energy gaps [eV] at the $T_{1,long}$ geometry calculated with different functionals.

Functional	**S_0-T_1 Energy Gap [eV]**
PBE0	0.556
PBE	0.561
B3LYP	0.623
CAM-B3LYP	0.711
LC-BLYP	0.751
LC-BLYP*	0.668
wB97X-V	0.902
M06-2X	0.642
Experiment[78]	2.16

We thus conclude, that the optimized $T_{1,long}$ does not seem to be able to describe the experimental emission behaviour adequately.

4.5 TD-DFT Surface Hopping Dynamics

Equipped with a computational model to describe the absorption behaviour of $[Re^{I}(CO)_3(bpy)(^{S\text{-}S}bpy)]^+$, excited state dynamics were conducted. First, TD-DFT surface hopping was performed as implemented in the *SHARC-ORCA* interface (see section 3.2.1).

4.5.1 100 fs Simulation Time

Within an energy range of 2.7 to 3.2 eV, a set of 101 trajectories were selected stochastically based on relative oscillator strengths.[75] They were propagated for 100 fs. The parameters used for the TD-DFT calculations as well as the SHARC simulations are given in section 3.2.1. For analysis only 96 of the 101 trajectories were considered. The remaining 5 were excluded due to very large differences in kinetic and potential energy initiated by a hop (> 1.2 eV). Thus, making these hops into high energetic states unrealistic (discussed in Appendix A.5, Fig. A7). To conclude, 96 trajectories were propagated for 100 fs and gathered for analysis.

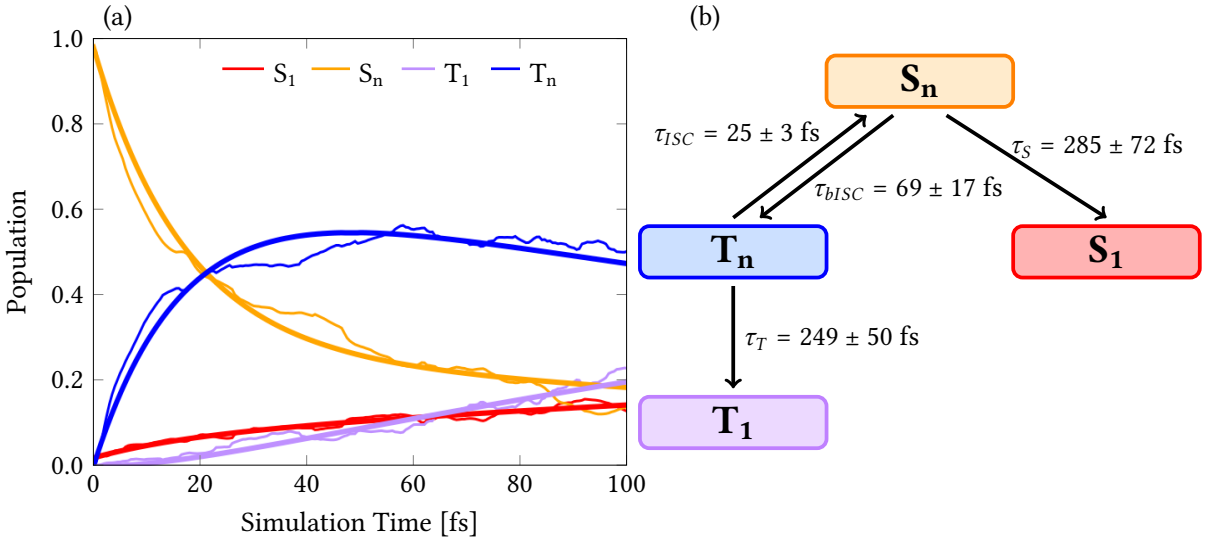

Figure 9: (a) Population of various excited states over the simulation times (thin lines) and fitted populations (bold lines). S_n = S_2 - S_{15}; T_n = T_2 - T_{15}. (b) Kinetic model of the population transfer within $[Re^{I}(CO)_3(bpy)(^{S\text{-}S}bpy)]^+$ together with fitted time constants.

Figure 9a (thin lines) shows the time evolution of the electronic populations within the spin-adiabatic states, i.e. electronic states distinguished by spin multiplicity and ordered by energy. The excited states were grouped together for clarity, where *S* stands for singlet states and *T* for triplet states (the population of all states are shown in Appendix A.5, Fig. A8).

Within the spin-free basis, S_n states (S_2-S_{15}) are populated by 98%, while the S_1 is populated by 2%. The initial population of S_n decays rather quickly and ultrafast intersystem crossing (ISC) to higher triplet states T_n (T_2-T_{15}) is observed. Subsequent population of the S_1 and T_1 due to internal conversion (IC) in the corresponding spin manifold are seen. After 100 fs simulation time, 48% of trajectories populate T_n states, 26% have relaxed to the T_1, 11% are located at S_n states, and 15% populate the S_1.

Analyzing the transitions between the electronic excited states (see Appendix A.5, Table A3) reveals, that relaxation to the S_1 and T_1 happens in a ladder like manner from higher singlet and triplet states respectively. Additionally, ISC does not only happen from the initially excited singlet manifold into the triplets, but also the back reaction is observed. Generally, the higher excited states experience spin-mixing and spin-expectation values around 1.0 are seen. Especially the initially excited states are already of mixed spin (Fig. 10), further facilitating the fast ISC rates. The dynamics are propagated in the diagonal basis, but the populations are plotted in the adiabatic representations. This explains the fast back and forth between singlet and triplet states if represented in the adiabatic basis.

Based on these findings a kinetic model (Fig. 9b) was proposed and time constants were fitted accordingly. Bootstrapping with 100 cycles was applied to obtain error estimates.[83] The fitted curves are shown as bold lines in Figure 9a together with the computed results (thin lines).

IC from the initially populated S_n states to energetically lower singlets and subsequently to the S_1 state occurs with a time constant of $\tau_S = 285 \pm 72$ fs. The majority of S_n population however, is transferred to the triplet manifold via ultrafast ISC with $\tau_{ISC} = 25 \pm 3$ fs. There, the system either relaxes down to the T_1 state with $\tau_T = 249 \pm 50$ fs or transfers back into the singlet manifold with $\tau_{bISC} = 69 \pm 17$ fs. The ultrafast ISC is not surprising as the initially populated excited states are already mixed in spin due to strong spin-orbit couplings. Some trajectories experience almost instantaneous ISC, which indicates that this process is rather driven electronically than by structural changes (similar to the fast components of ISC described in Ref. 81). No relaxation to the ground state S_0 within 100 fs was observed.

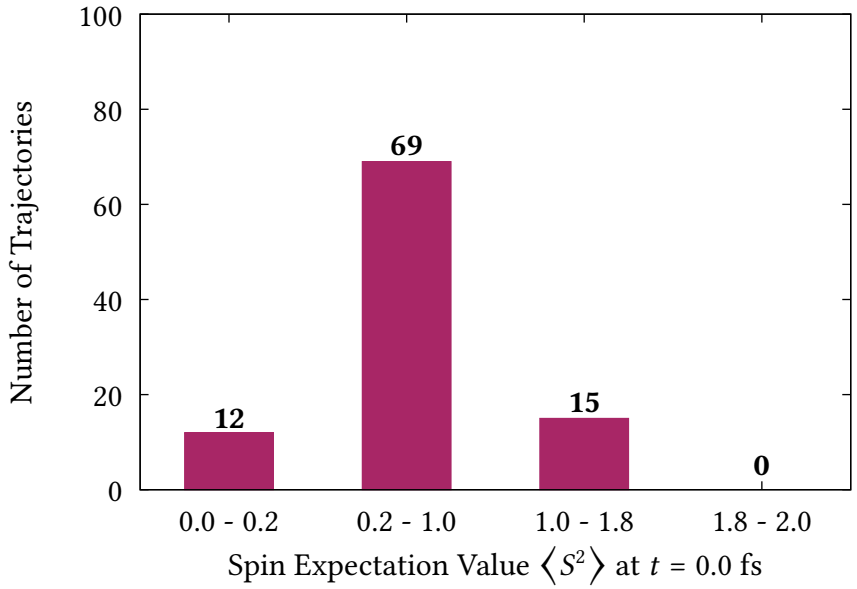

Figure 10: Spin expectation values $\langle S^2 \rangle$ of the starting states collected for each trajectory. Values between 0.2 and 1.8 indicate mixed spin.

Additionally, within the time frame of 100 fs almost no rotation around the Re-N bond is seen. The dihedral angle C_{CO}-Re-$N_{s\text{-}s_{bpy}}$-$C_{s\text{-}s_{bpy}}$ changes on average only a few degrees (5-9°) throughout the simulations. Thus, no conversion to different conformers are observed. Albeit the small energy barrier of the rotational conformers, rotation seems to be on a time-scale beyond 100 fs.

An interesting observation can be made when analyzing the length of the S-S bond over the simulated time. Here, two different pathways for the system are observed.

S-S_{long} Trajectories:

First, one set of trajectories experience drastic elongation of the S-S bond from 2.05 Å to up to 3.20 Å. These trajectories will be called S-S_{long} trajectories in the following discussion. As a consequence of the elongation, dissociation of the S-S bond could be assumed. However, dissociative behaviour cannot be computed correctly by our current computational method, since DFT is a single-reference method and dissociation requires multi-reference treatment. Thus, no real dissociation can be observed in our simulations, only elongation of the bond, and the results at the geometries with elongated bond lengths have to be treated with caution. The trends can be discussed nonetheless.

Figure 11 shows (a) the time evolution of the excited state character, (b) the electron-hole

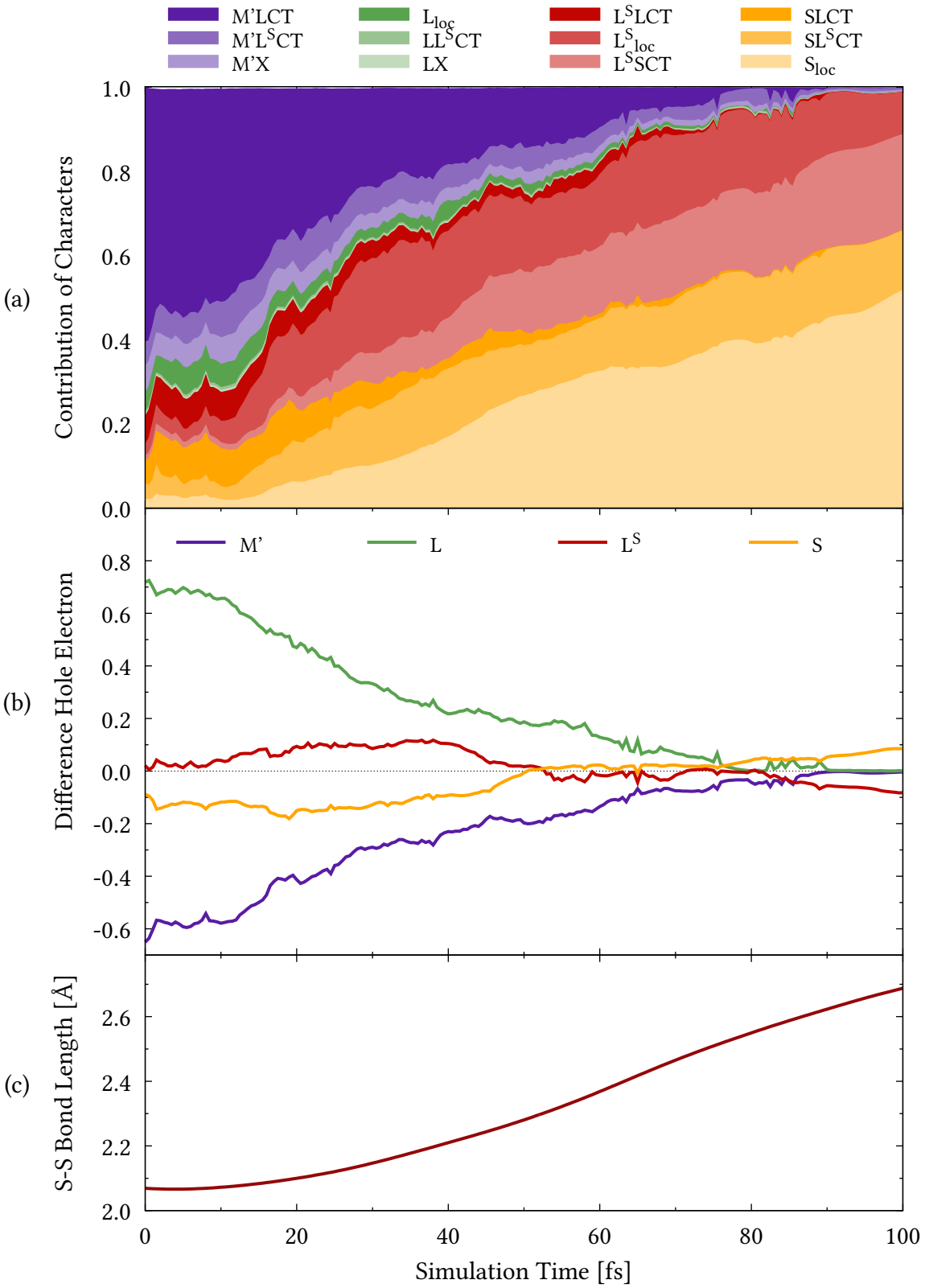

Figure 11: (a) Transition density matrix analysis. (b) Difference population (hole-electron) on each fragment. (c) Time evolution of the S-S bond length. The data for each panel is averaged over all S-S_{long} trajectories.

composition over time, and (c) the time evolution of the S-S bond length, averaged over all S-S_{long} trajectories (Plots including M and L^{CO} seperately are shown in Appendix A.5, Fig. A9). Regarding the excitation character, the trajectories start in predominantly M'LCT (61%) states. During the simulation, the contributions of S_{loc}, $SL^{S}CT$, $L^{S}S$, and $L^{S}{}_{loc}$ increase and dominate the excited state character after 100 fs (51% S_{loc}, 14% $SL^{S}CT$, 23% $L^{S}S$, and 10% $L^{S}{}_{loc}$). It is apparent, that the S-S bond lengthening is akin to local excitation at the sulfurated ligand. The difference population for hole and electron contributions also show little to no charge flow between the fragments at t = 100 fs.

Analyzing the natural transition orbitals at such elongated geometries reveals an excitation of the π-orbital of the S-S bond to a σ^*-orbital, thus destabilizing the bond and aiding the elongation. Furthermore, the geometry, character and NTOs of such trajectories closely resemble the NTOs at the $T_{1,long}$ geometry (Fig. 8b) found during T_1 optimization in Section 4.4. This suggests, that S-S_{long} trajectories populate the $T_{1,long}$ or regions near it.

Looking into the behaviour of the individual trajectories reveals that first a state with local excitation on the $^{S\text{-}S}$bpy ligand is reached and then the S-S bond lengthens subsequently (Fig. 12). This reinforces that the anti-bonding σ^*-orbital has to be occupied to allow the bond elongation. The S-S_{long} trajectories populate predominantly the T_1 state (59%) after 100 fs. Population of the S_1 and T_2 state are observed as well, albeit to a smaller extent (18% and 24% respectively). The high population of these low-energy states is achieved as follows. The trajectory hops at some point in the simulation to an excited singlet or triplet state with S_{loc} character. From there the propagation starts following its gradient leading to elongation of the S-S bond length towards the $T_{1,long}$, facilitated by the occupation of the anti-bonding S-S orbital. These structural changes invoke energy lowering of the S_{loc} state, whereas all other states (including the ground state) destabilize, increasing their energy. Thus, the S_{loc} state separates from the other excited states, now being the lowest excited state of its spin multiplicity, the S_1 or T_1. This means, the fast population of low lying excited states cannot be attributed to efficient relaxation within the respective spin manifold, but rather to an energy lowering of the S_{loc} state.

Within the first 100 fs 20% of trajectories (19 out of 96) experience S-S bond lengthening and end up in a S_{loc} state. The energy gap between the active state and the ground state decreases with longer S-S bond lengths. The T_1 potential energy drops below the S_0 energy at S-S bond

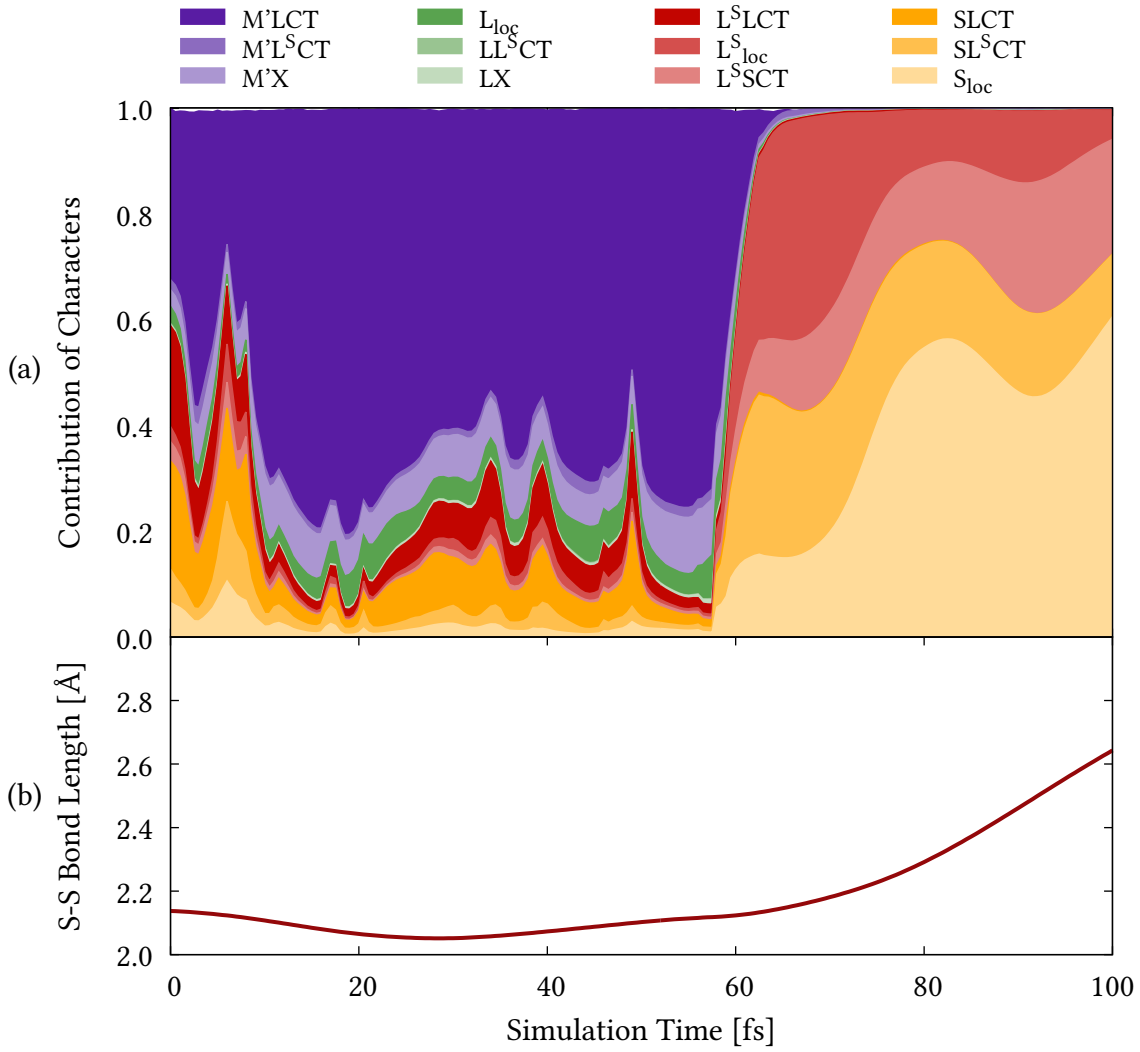

Figure 12: (a) Contribution of characters for one example S-S$_{long}$ trajectory. (b) Respective S-S bond length [Å].

lengths above 2.8 Å (see Appendix A.5, Fig. A10). Two possibilities arise - either TD-DFT cannot describe the system accordingly with this elongation and the energies are not to be trusted. Or a crossing point between T_1 and S_0 is reached and the T_1 is the lowest energy state at those geometries. Nonetheless, the small energy gap suggests that non-radiative relaxation to the ground state may be possible from this point. This will be discussed later in section 4.8 in light of a crossing point between S_0 and T_1. However, such transitions were not observed in the simulations, due to their short time scale.

S-S$_{short}$ Trajectories:

The remaining trajectories (80%) do not experience elongation of the S-S bond within the 100 fs simulation time and are thus labelled as S-S$_{short}$ trajectories. Oscillation around the equilibrium

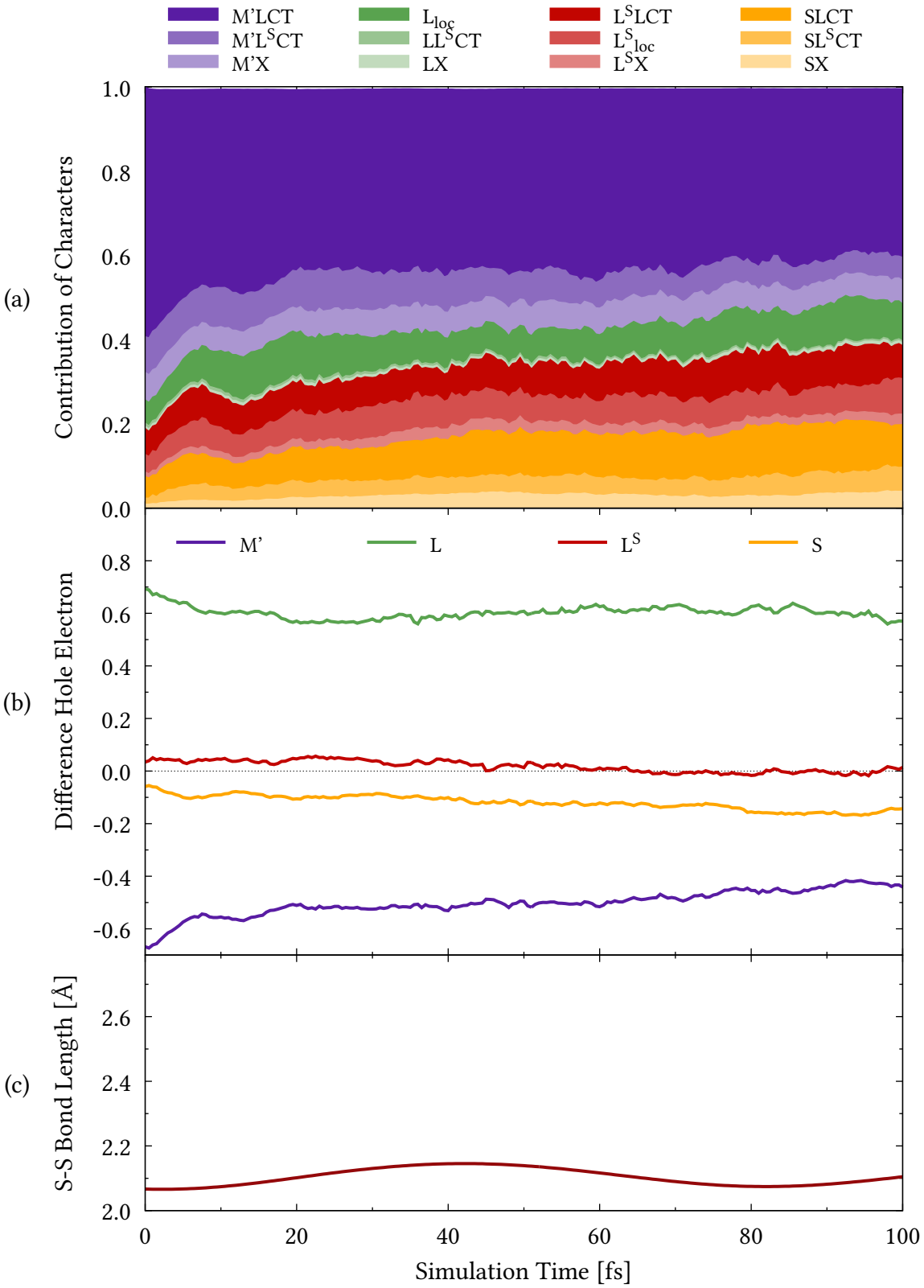

Figure 13: (a) Transition density matrix analysis. (b) Difference population (hole-electron) on each fragment. (c) Time evolution of the S-S bond length. The data for each panel is averaged over all S-S_{short} trajectories.

S-S bond length of 2.05 Å is seen (see Fig. 13c). As for the S-S_{long} trajectories, the dynamics start in predominant M'LCT (59%) states (Fig. 13a). This stays the main character over the whole simulation time, although its contribution decreases to 40% at t = 100 fs. Over the simulation time the contribution of charge transfer from L^S and S to L increases when averaging over all S-S_{short} trajectories. Analyzing the individual trajectories shows that the excitation character at t = 100 fs is comprised over multiple components (see Appendix A.5, Fig. A11). Some trajectories keep the M'LCT character, whereas other change in character to either M'L^SCT, L_{loc} or L^SLCT/SLCT. This is in contrast to the more uniform character of the S-S_{long} trajectories. All trajectories have in common, that the electron component is located almost exclusively at the 2,2'-bpy ligand (see fragment L, Fig. 13b). The hole component is split between the metal center, the CO ligands and the sulfur atoms, as also seen in the excited state characters. Plots including M and L^{CO} seperately are shown in Appendix A.5, Fig. A12.

The S-S_{short} trajectories relax to different electronic excited states, with 10% S_1, 22% S_n, 16% T_1, and 52% T_n after 100 fs. The large amount of population in higher lying excited states S_n and T_n suggests slower relaxation rates within the singlet and triplet manifolds. This is in contrast to the rather high populations of the S_1 and T_1 in the S-S_{long} trajectories. This difference in population after 100 fs can be seen in the population curves (thin lines) in Fig. 14a and c.

Due to this difference in populated states, the distribution among states and time constants for each set of trajectories will be discussed separately. The same kinetic model as established before was used, however the populations and time constants were fitted using only data points from the respective set of trajectories. The populations and kinetic fits are shown in Figure 14.

The ultrafast ISC ($\tau_{ISC} \approx 23 - 26$ fs) seems independent from the type of trajectory. This is in line with the suggestion, that ISC shows little dependency on structural changes. However, the fast back and forth between the singlet and triplet manifold is only seen in the S-S_{short} trajectories. The fast energy lowering to the T_1 suppresses ISC back to the singlet manifold for the S-S_{long} trajectories. Furthermore, relaxation to the T_1 and S_1 is fast for the S-S_{long} trajectories with $\tau_T = 54 \pm 19$ fs and $\tau_S = 116 \pm 68$ fs. In contrast, the S-S_{short} trajectories show time constant of $\tau_T = 535 \pm 137$ fs and $\tau_S = 400 \pm 122$ fs.

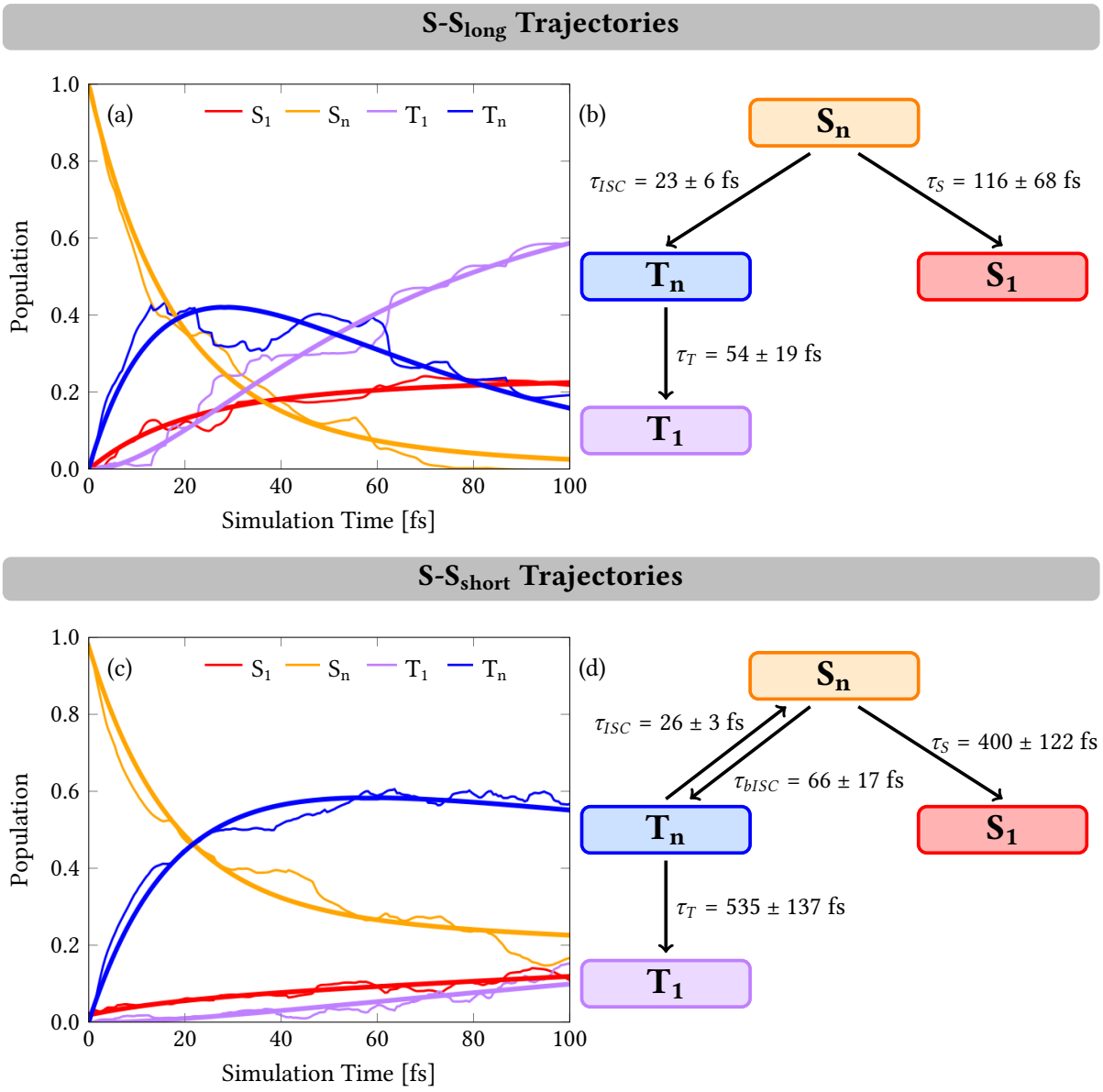

Figure 14: (a) Population of various excited states for the S-S$_{long}$ trajectories (thin lines) with fitted curves (bold lines). (b) Kinetic model with fitted time constants for S-S$_{long}$ trajectories. (c) Population (thin lines) and fitted curves (bold lines) for S-S$_{short}$ trajectories. (d) Kinetic model and fitted time constants for S-S$_{short}$ trajectories.

4.5.2 150 fs Simulation Time

To analyze the excited state behavior of $[Re^{I}(CO)_3(bpy)(^{S\text{-}S}bpy)]^+$ further, randomly selected trajectories were propagated for an additional 50 fs, summing to 150 fs simulation time in total. However, due to the large computational cost of the TD-DFT dynamics, this was done only for 60 trajectories.

After 100 fs, 48 (80%) of these trajectories were denoted as S-S_{short} and 12 (20%) were regarded S-S_{long} trajectories. During the additional 50 fs simulation time, 6 previously regarded S-S_{short} trajectories reached the S_{loc} state and experienced subsequent S-S bond elongation. Such trajectories had not reached a minimum yet at the 100 fs mark. This indicates, that over time more population will go from higher-lying states to the S_{loc} state and thus into the elongated geometry. However, the time scale of populating the S_{loc} is not tangible from the current simulations.

Regarding the overall kinetic model and time constants, only marginal changes are seen for the 150 fs dynamics with $\tau_{ISC} = 25 \pm 4$ fs, $\tau_{bISC} = 79 \pm 24$ fs, $\tau_S = 160 \pm 69$ fs, and $\tau_T = 251 \pm 69$ fs (see also Table 3). Similarly, the character composition of the S-S_{long} and S-S_{short} trajectories are comparable to the values discussed for 100 fs simulation time. The population curves for 150 fs are shown in Appendix A.5, Figure A13.

The most interesting observation is the evolution of the S-S bond length over longer time scales. Figure 15a shows the S-S bond length evolution of all trajectories over time, coloured according to the S_{loc} contribution ($\geq$ 20% S_{loc} orange). The S-S_{long} trajectories experience S-S bond elongation to bond lengths of about 2.8 Å to 3.2 Å. However, when propagating for longer times no further elongation is seen. In contrast, the S-S bond length decreases again. Two example trajectories were propagated for an additional 50 fs (200 fs total) to further investigate their behaviour (Figure 15b). There, the S-S bond length seems to oscillate around a "new" equilibrium length of around 2.6 Å (Fig. 15b). This would correspond nicely to the $T_{1,long}$ minimum discussed earlier in section 4.4.

Regarding this behaviour of the S-S bond lengths, two possibilities arise.

1. The bond would dissociate in experiment, but is hindered in our simulations by the inability of TD-DFT to describe dissociation.

2. The system finds a minimum on the T_1 PES (most likely the $T_{1,long}$), which is defined by a longer S-S bond length.

The second possibility is in line with the characteristics of the optimized $T_{1,long}$ minimum. However, the possibility of dissociation cannot be discarded either, since it cannot described with the current methods.

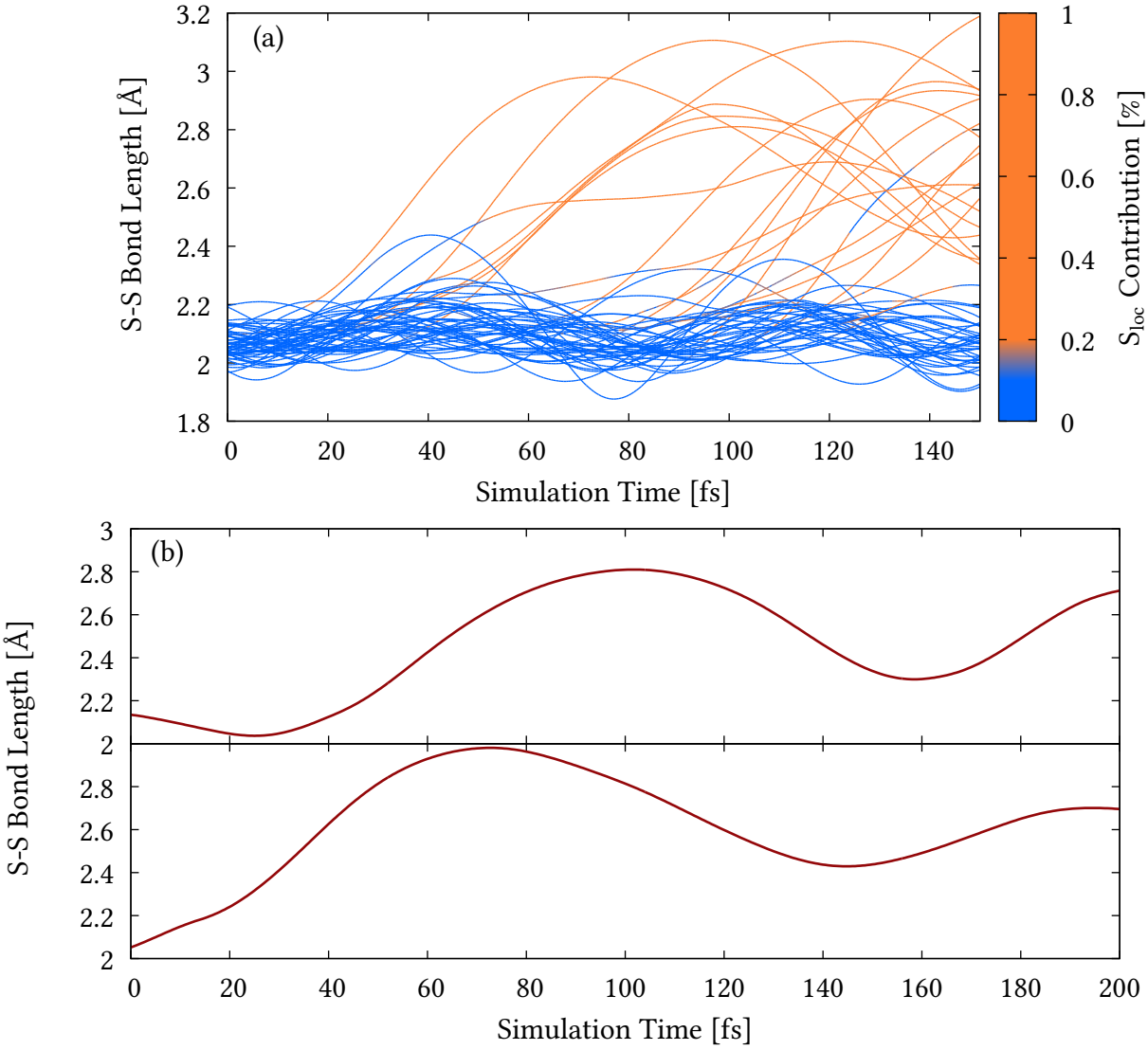

Figure 15: (a) Time evolution of the S-S bond length for all trajectories that were propagated for 150 fs. Blue corresponds to S_{loc} contribution < 20%, orange to S_{loc} contribution ≥ 20%. (b) S-S bond length evolution for two example S-S_{long} trajectories for 200 fs.

4.6 LVC Surface Hopping Dynamics

4.6.1 Population Analysis

The previously discussed TD-DFT/SH dynamics were able to give insight into the early dynamics of $[Re^{I}(CO)_3(bpy)(^{S\text{-}S}bpy)]^+$. However, due to the high computational cost of such calculations, no dynamics beyond the 200 fs mark were simulated in the framework of this thesis. In order to investigate the long-time dynamics, SH simulations with the parametrized LVC model

potentials were conducted. This allows for very fast computations of the individual time steps. Thus, a set of 992 trajectories was propagated for 10 ps (10000 fs). The parameters used within the *SHARC* package are described in section 3.2.2.

First a comment about the limitations of LVC is in order. Within LVC the PESs of the excited states are expanded upon the reference (here FC) geometry on the basis of the harmonic normal mode coordinates of the ground state. This can lead to large energy barriers when leaving the structural vicinity of the FC geometry, especially regarding high frequency modes. Thus, large distortion of the geometry, such as rotation or dissociation, is prohibited by applying these potentials as the energy barrier would be too large to overcome. Therefore, no interconversion between the rotamers can be simulated by LVC. Furthermore, the potentials are computed from the lowest-lying excited states at the FC geometry and only these states are considered during the dynamics. Thus, no intruder states, i.e. states that become lower in energy during the simulations, are considered.

The behaviour within the first 100 fs simulation time will be discussed first (Fig. 16a), to compare the results of the TD-DFT/SH and LVC/SH dynamics (Population curves for all states are given in Appendix A.6, Fig. A14). The trajectories initially populate various S_n states (98%) as well as the S_1 (2%). The population of S_n decays quickly to around 13% within the first 100 fs. At nearly the same rate the T_n states are populated, reaching their maximum with 55% electronic population at around 45 fs, after which a slow decay is observed. Simultaneously, the population of the S_1 and T_1 increase, with faster population of the T_1 compared to the S_1 state. The ground state S_0 is not populated within 100 fs.

Compared to the results obtained by TD-DFT/SH (Fig. 16b), faster relaxation to the T_1 is seen. This could be due to underestimated energy differences between the respective states within the LVC model. Another reason could be the gradient selection applied in the TD-DFT/SH dynamics, thus not all states are accessible at every time step. This could hinder hops to lower-energetic states in the TD-DFT/SH simulations, which were possible for LVC/SH. Nonetheless, the overall populations and kinetics seem to be in good agreement between LVC/SH and TD-DFT/SH dynamics. This conformance validates the performance of the LVC model on the one hand, and indicates that TD-DFT/SH dynamics give accurate statistics on the other hand, at least for the first 100 fs.

The fast computational performance of the LVC model allows us to investigate the non-adiabatic

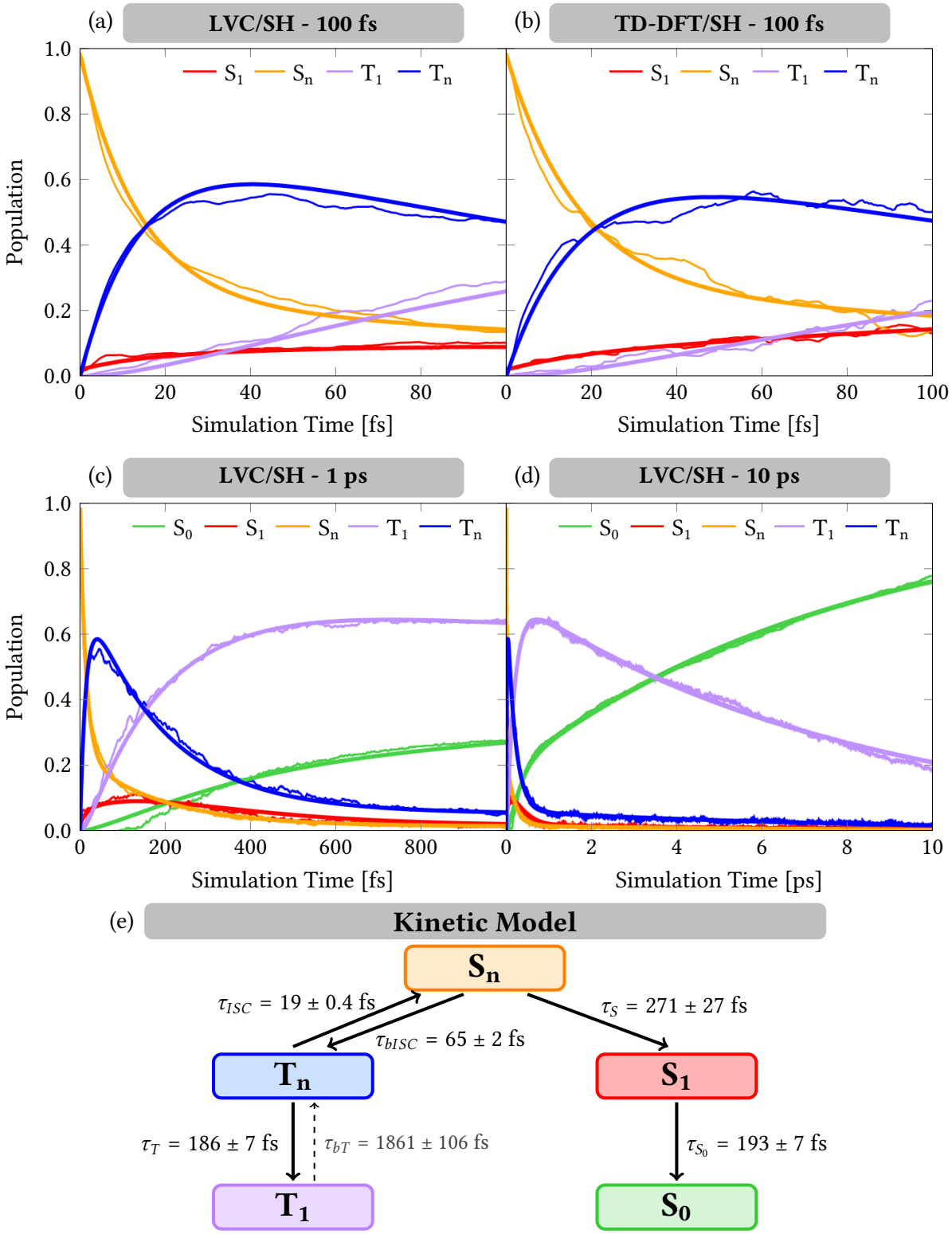

Figure 16: Calculated adiabatic electronic populations (thin lines) and fitted populations (bold lines) for (a) LVC/SH 100 fs (b) TD-DFT /SH 100 fs, (c) LVC/SH 1 ps, (d) LVC/SH 10 ps.(e) Kinetic model and fitted time constants according to the results from LVC/SH 10 ps.

dynamics of $[Re^{I}(CO)_3(bpy)(^{S\text{-}S}bpy)]^+$ beyond the 100 fs mark. Figure 16c shows the electronic populations for 1 ps simulation time (thin lines). The population of high energetic singlet states S_n decays further and has reached almost zero within 1 ps. After reaching a maximum of 12% at 132 fs, the electronic population of the S_1 starts slowly decaying to 2%. The population of the T_n states also decreases, reaching 3% at t = 1 ps. In contrast the T_1 state gets populated quickly and reaches a maximal population of 65%. Population of the ground state S_0 is seen starting around 150 fs.

Finally, extending the dynamics simulations to 10 ps (Fig. 16d), reveals the decay of T_1 population in favor of the increasing electronic population in S_0. After 10 ps the trajectories show 78% population in S_0 and 19% in T_1, with minor contributions in the other electronic states.

Based on the transitions seen in the trajectories (see Appendix A.6, Table A4) a kinetic model was proposed and the population curves were fitted accordingly, resulting in estimated time constants τ_X (Fig. 16e). Error estimates were obtained by bootstrapping including 100 cycles.[83] The fitted curves are shown in Figures 16b - d (bold lines), which closely follow the population curves in the most parts. These curves show the fit using the data until 10 ps for every time-window shown. Time constants fitted for data points up to 100 fs and 1 ps respectively are given in Table 3, however are not discussed thoroughly here.

The fast component of the decrease in S_n population is attributed to ultrafast ISC with a time constant of τ_{ISC} = 19 ± 0.4 fs. The slower component can be assigned to relaxation down the singlet manifold to the S_1 state, which is populated with a time constant of τ_S = 271 ± 27 fs. The fitted curves for the S_0 start increasing already at t = 0 fs, whereas the computed population only rises after about 150 fs. (Fig. 16c). Incorporating relaxation within the S_1 state into the model leads to more accurate description of the onset of the S_0 population (see Appendix A.6, Fig. A15).

The triplet manifold experiences a multitude of reaction pathways. Intersystem crossing back to S_n with a time constant of τ_{bISC} = 65 ± 2 fs and relaxation to the T_1 state, with τ_T = 186 ± 7 fs, decrease the population in T_n. As discussed before, the fast interchanging between singlet and triplet multiplicity is attributed to high amounts of mixing in the excited states due to strong spin-orbit coupling (see also Figure 17a, where initial states show mixed spin character).

Once the T_1 is reached, the trajectories stay in that state for a while, most likely reaching a

minimum on the T_1 PES. In an experimental setup, the system would relax to the ground state from there, by reaching a nearby (or any other) crossing point via non-radiative relaxation or by luminescence. Experimental phosphorescence happens on a time scale of a few hundred nanoseconds, thus not reachable by our simulations. A crossing point between the S_0 and T_1 can indeed be found (see Section 4.8), but is not accessible by LVC (discussed in Section 4.9). Therefore, the relaxation to the ground state from the long-lived T_1 minimum is forbidden in the simulations. During SH the total energy is conserved, meaning lowering the potential energy increases the kinetic energy. We applied a damping function during the dynamics to decrease the total energy steadily in order to mimic energy loss due to interactions with the environment. There are some limitation however, and trajectories in low-lying states might still have unrealistically high kinetic energy. The prolonged population of the T_1 with relatively high kinetic energies enables the system to encounter a stochastic hop to excited states at higher energies. Such a transition is very unlikely to occur in a real system. However, in our dynamics such hops are seen for trajectories populating the T_1, where slow transitions (τ_{bT} = 1861 ± 106 fs) to the T_n states are observed. The timescales on which this happens, do not resemble any pathway for real molecules, thus are not further discussed here.

Relaxation to the ground state S_0 exclusively occurs from the S_1 state. Population transfer to S_0 follows a time constant of τ_{S_0} = 193 ± 7 fs. However, one has to keep in mind that the relaxation via the S_1 is most likely only a minor pathway in the real system, as most population would accumulate in the T_1. Thus, rates for ground state recovery obtained by LVC/SH have to be treated with caution. Overall, the time constants fitted for LVC/SH dynamics are in good agreement with their respective TD-DFT/SH counterparts (see Table 3), further validating the obtained values and the chosen computational models.

4.6.2 Geometric Analysis

The TD-DFT/SH simulations showed the existence of two possible pathways within the excited state dynamics of $[Re^{I}(CO)_3(bpy)(^{S\text{-}S}bpy)]^+$. The defining difference between those pathways is the S-S bond length, whether elongation occurs or not. To investigate such behaviour in the LVC dynamics a geometric analysis has been conducted. At each time step, the S-S bond length and the energy gap between the active state and the ground state was collected for each

Table 3: Time constants in fs fitted for the different dynamics simulations. The LVC/SH time constants only contain data points up to the indicated simulation time during the respective fits.

[fs]	TD-DFT/SH				LVC/SH		
	100 fs (all)	S-S_{long}	S-S_{short}	150 fs (all)	100 fs	1 ps	10 ps
τ_{ISC}	25 ± 3	23 ± 6	26 ± 3	25 ± 4	18 ± 0.6	19 ± 0.6	19 ± 0.4
τ_{bISC}	69 ± 17	-	66 ± 17	79 ± 24	52 ± 3	63 ± 3	65 ± 2
τ_T	249 ± 50	54 ± 19	535 ± 137	251 ± 69	129 ± 10	182 ± 8	185 ± 7
τ_S	285 ± 72	116 ± 68	400 ± 122	160 ± 69	314 ± 26	274 ± 21	271 ± 27
τ_{S_0}	-	-	-	-	-	183 ± 5	193 ± 7
τ_{bT}	-	-	-	-	-	1709 ± 260	1861 ± 106

trajectory. Additionally, a differentiation of trajectories according to the spin expectation value of the active state was made. Spin expectation values of $0.2 > \langle S^2 \rangle$ are considered as singlet states, $0.2 < \langle S^2 \rangle < 1.8$ correspond to mixed states, and values of $\langle S^2 \rangle > 1.8$ are considered as triplet states. The time-resolved data points were convoluted both in bond length and energy using Gaussian functions with FWHM values of 0.025 Å and 0.1 eV respectively.

The resulting plots are shown in Figure 17 for selected simulation times. The initially populated states already show significant amounts of mixed character as seen in Figure 17a, with S-S bond lengths corresponding to the Wigner distribution around the equilibrium bond length of 2.05 Å. Over time, the population of mixed states redistributes to singlet and triplet states. A slight elongation of the S-S bond length accompanied by energy gap lowering is seen within the first 100 fs. Considering even longer simulation times further elongation of the S-S bond occurs, especially in the triplet manifold. The bond lengths do not surpass 2.6 Å for the most part, as they are constrained by the LVC model potentials. Still, the same trend as in the TD-DFT/SH dynamics is observed and the system tends to elongate the S-S bond. Furthermore, the population of two different regions **A** and **B** within the triplet states is observed, best seen in Figure 17c and d.

Region **A** shows energy gaps of the active state to the ground state between 1.5 to 2.5 eV with S-S bond lengths close to equilibrium. Region **B** is characterized by higher S-S bond lengths (2.3 - 2.6 Å) and smaller energy gaps (0.5 - 1.5 eV). The population of these two distinct regions

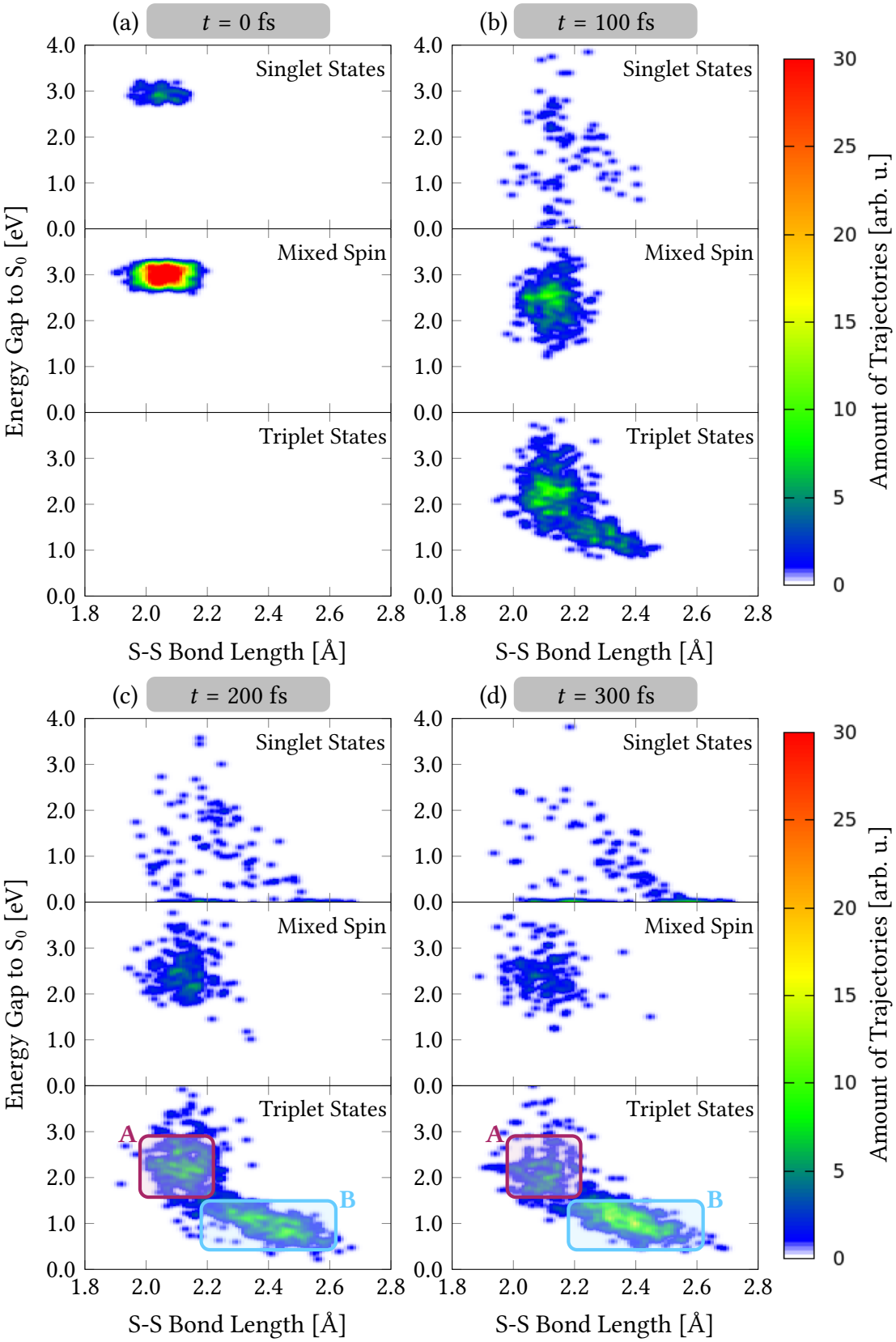

Figure 17: Convoluted scatter plots of the S-S bond length [Å] against the energy gap of the active state to the S_0 [eV] at (a) $t = 0\,\text{fs}$, (b) $t = 100\,\text{fs}$, (c) $t = 200\,\text{fs}$, and (d) $t = 300\,\text{fs}$. Trajectories divided by spin expectation value $\langle S^2 \rangle$ ($0.2 > \langle S^2 \rangle$ singlet states, $0.2 < \langle S^2 \rangle < 1.8$ mixed spin, and $\langle S^2 \rangle > 1.8$ triplet states).

suggests the possibility of two local minima within the triplet manifold or more precisely the T_1. After 300 fs (Fig. 17d), region **A** is depleted in favour of region **B**, which spans a relatively wide range of bond lengths. Turning attention to the singlet states at longer simulation times reveals trajectories in the ground state S_0 scattered across a multitude of S-S bond lengths.

Within the TD-DFT/SH dynamics, most trajectories were of S-S_{short} character. Similarly, the LVC/SH dynamics at t = 100 fs (Fig. 17b) show predominant population of the high energy region with shorter bond lengths. However, over time it can be seen that the majority of trajectories transfer to the elongated S-S bond region within the first 300 fs. At even longer times (see Appendix A.6, Fig. A16) the distribution remains similar to the one seen in Figure 17d with further population shift to region **B** and overall depletion of the triplet manifold in favor of the S_0 (as seen in the populations of Fig. 16d). The beginning of this trend was already seen in the TD-DFT/SH dynamics where 6 additional trajectories reached the elongated state. Thus, it can be assumed that the the S-S_{long} region gets populated increasingly over longer simulation times, whereas the population of the S-S_{short} region is decreasing.

4.7 Triplet Optimization Revisited ($T_{1,long}$)

The previously optimized triplet minimum $T_{1,long}$ (Section 4.4) was not able to describe the experimental luminescence of $[Re^{I}(CO)_3(bpy)(^{S\text{-}S}bpy)]^+$. The small S_0-T_1 energy gap of 0.56 eV and the locally excited character at the $^{S\text{-}S}$bpy ligand do not resemble the experimental observables.

After analysing the dynamics simulations, the possibility of another T_1 minimum close to the FC region arose. This could explain the two possible pathways in the TD-DFT/SH dynamics, with and without S-S bond elongation, as well as the two populated regions in the LVC/SH dynamics.

In order to find such second minimum, 120 geometries were extracted from the LVC trajectories at t = 300 fs, which fulfilled two conditions: T_1 being the active state and showing an S-S bond length between 2.05 and 2.15 Å. Subsequently, a T_1 optimization at each geometry using the LVC potentials was performed. Here, two different minima were reached. One minimum is defined by an energy gap to the ground state of 1.22 eV and S-S bond lengths around 2.25 Å and was reached in 36% of computations, very much resembling the $T_{1,long}$ found with TD-DFT . The other minimum (64% of geometries) showed bond lengths more close to the equilibrium length

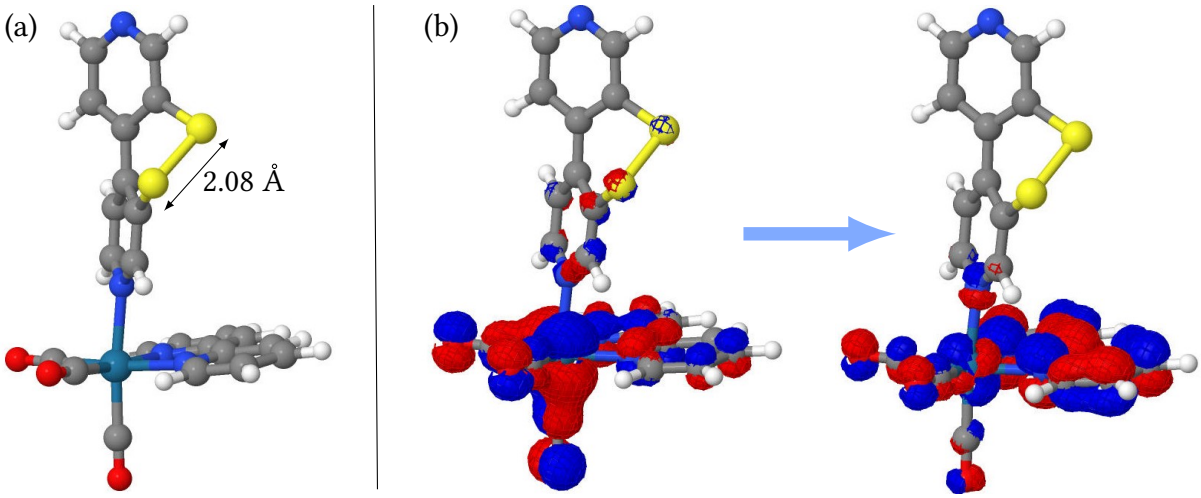

Figure 18: (a) Structure of $T_{1,short}$. (b) Natural transition orbitals of the S_0 - T_1 transition at the $T_{1,short}$ geometry from left (hole) to right (electron).

around 2.08 Å and higher energy difference between the S_0 and T_1 surface of approximately 1.83 eV. Out of these geometries, 30 were then reoptimized at the PBE0/D4/SARC-ZORA-SVP (Re), ZORA-def2-SVP (C, O, N, S, H) level of theory to confirm the existence of a local minimum more accurately. All of these geometries converged to the same critical point. Subsequent frequency calculations produced only positive frequencies, confirming that this is a minimum on the PES.

This newly found T_1 minimum (Fig. 18a), called $T_{1,short}$, has a S_0-T_1 energy gap of 1.99 eV, closely resembling the experimental phosphorescence energy of 2.16 eV. The S-S bond length is 2.08 Å, a slight elongation compared to the FC geometry, albeit to a much lesser extent than $T_{1,long}$ (2.57 Å). The character of the $S_0 \rightarrow T_1$ transition at $T_{1,short}$ is dominated by M'LCT (53%). More precisely, the NTOs (Fig. 18b) reveal a transition of a Re d-orbital, including CO contributions, to a π^*-orbital of the 2,2'-bpy ligand. This kind of excitation is typical for the long-lived emissive state in Re-tricarbonyl-diimine complexes.[79]

Based on the energy gap, the S-S bond length and the character of excitation, $T_{1,short}$ is most likely the emissive T_1 minimum. In this case, the predicted phosphorescence energy of 1.99 eV is in good agreement with the experimental value of 2.16 eV, resulting in a difference of 0.17 eV.

4.8 S_0-T_1 Crossing Point

The question for the fate of $T_{1,long}$ remains. To answer this, a MECP computation, as implemented in *ORCA*, between the S_0 and T_1 PESs was conducted, to find a crossing point where radiationless relaxation to the ground state can occur. The so-found geometry shows an S-S bond of 2.8 Å, longer than in the $T_{1,long}$ geometry (2.56 Å). Comparing the total energy of the T_1 state at the $T_{1,long}$ geometry and the MECP shows a difference of 0.14 eV. This suggests, that the MECP is accessible from the $T_{1,long}$ by elongation of the S-S bond. Figure 19 shows the $T_{1,long}$ geometry together with the MECP geometry, revealing besides the longer S-S bond, only minor displacements such as rotation of the upper ring of $^{S\text{-}S}$bpy and a slightly different orientation of the 2,2'-bpy ligand. During the TD-DFT /SH dynamics, S-S_{long} trajectories were able to reach geometries with highly elongated S-S bonds (see Fig. 15). Even bond lengths beyond 2.8 Å were observed, supporting the possibility of reaching the MECP.

This suggests, that radiationless relaxation is possible from $T_{1,long}$ upon reaching the aforementioned crossing point. However, no relaxation from the T_1 to the ground state was seen in the LVC dynamics. Within the LVC model, harmonic approximations were applied, thus prohibiting large geometry distortions for high frequency modes compared to the FC geometry. This artificially increases the barrier between the $T_{1,long}$ minimum and the MECP to 0.57 eV (both were recalculated based on the LVC potentials). Radiationless decay is therefore unfavoured in the framework of the LVC model and thus not observed in the dynamics.

As this T_1-S_0 transition is not seen in any of the dynamics, no time constant can be fitted. However, an estimation can be made. Based on the oscillation around high S-S bond lengths in S-S_{long} trajectories (Fig. 15) within 150 fs, one can assume that the MECP can be reached on the femto-second to pico-second time-scale. Ground state recovery seen in time-resolved infrared (TRIR) spectra show time constants of $\tau = 21 - 27$ ps. By comparison to experimental ground state recovery an estimated time constant can be proposed, discussed in section 4.10.

4.9 Limitations of the Computational Models

As every computational method has its limits and inaccuracies, the limitations of the computational methods used in this thesis and their implications will be discussed here.

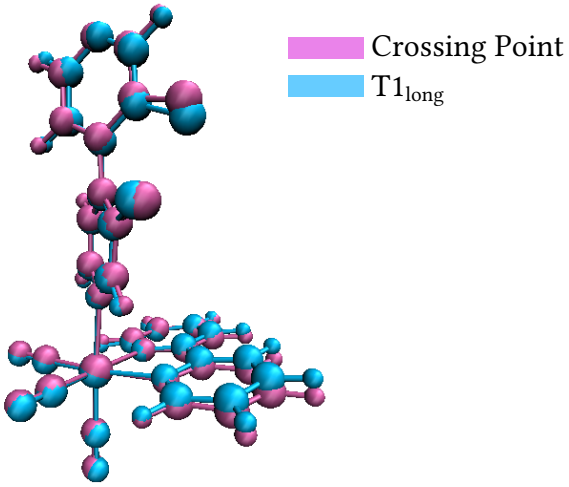

Figure 19: S_0-T_1 crossing point (pink) and $T_{1,long}$ (blue) geometry.

Both TD-DFT and LVC have limited usage when it comes to dissociative processes. However, during the dynamics it was revealed, that at least pronounced bond elongation and possibly bond breaking of the S-S bond takes place in $[Re^{I}(CO)_3(bpy)(^{S\text{-}S}bpy)]^+$. To compare the performance of TD-DFT and LVC, reference calculations with two multi-reference methods - CASSCF and CASPT2 - were employed. The active space was chosen to include 12 orbitals and 12 electrons. Since such calculations are computationally very expensive and the relevant bond elongation takes place in the $^{S\text{-}S}$bpy ligand, only the free ligand of $[Re^{I}(CO)_3(bpy)(^{S\text{-}S}bpy)]^+$ will be considered.

In order to simulate the dissociation of the S-S bond, a scan over multiple bond lengths was conducted. At each step, the S-S bond length was fixed and the rest of the molecule was allowed to relax. These constrained optimizations were performed on the T_1 PES. This procedure was repeated with each method (LVC, TD-DFT, CASSCF). Additionally, the energies of the CASSCF optimized structures were recomputed with CASPT2. The results of the scans are shown in Figure 20.

In addition, the $T_{1,short}$ and $T_{1,long}$ were optimized with all three methods. Each method will be discussed separately in the following.

We note that the computations with LVC were performed for the whole complex $[Re^{I}(CO)_3(bpy)(^{S\text{-}S}bpy)]^+$ as the model was parametrized for the complex, while the other calculations (TD-DFT, CASSCF, CASPT2) were performed for the free ligand $^{S\text{-}S}$bpy.

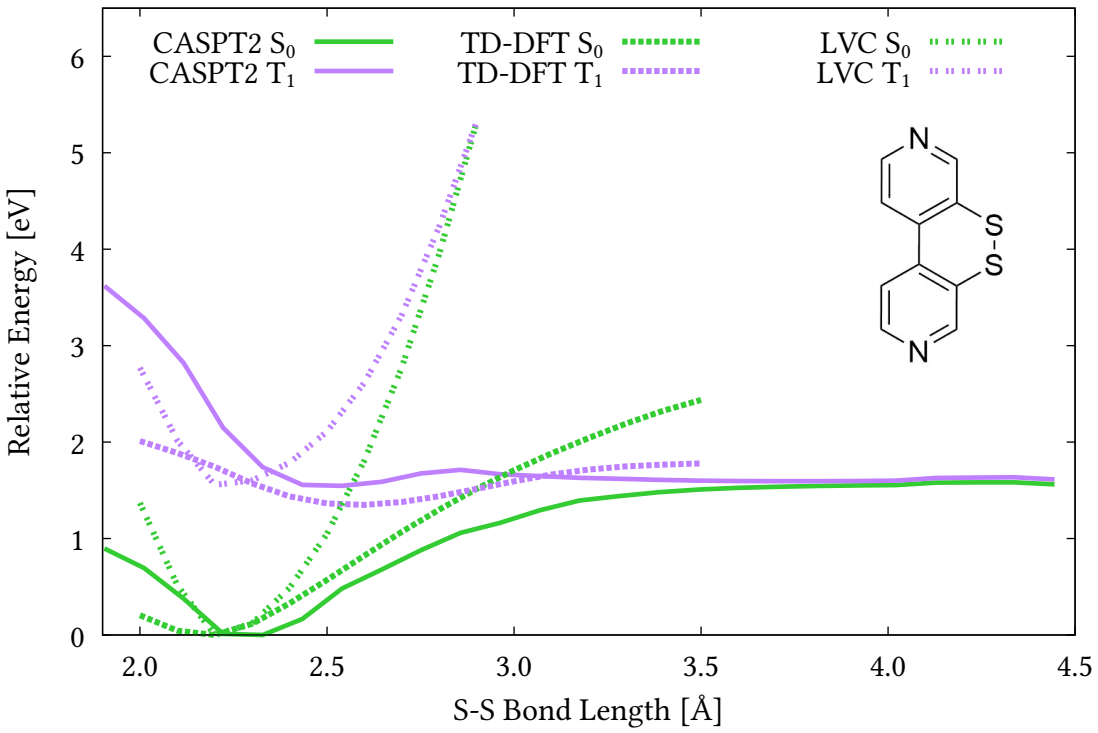

Figure 20: Potential energy curves upon the elongation of the S-S bond of $^{S\text{-}S}$bpy calculated with CASPT2(12,12), TD-DFT and of $[Re^{I}(CO)_3(bpy)(^{S\text{-}S}bpy)]^+$ calculated with LVC. Energies relative to the lowest energy within the respective method.

4.9.1 CASSCF / CASPT2

First, the S-S bond length scan was performed using CASSCF for the optimizations and CASPT2 at the respective geometries. The multi-configurational nature of these methods allows describing homolytic bond breaking, such as the case for a disulfide bond. Upon the dissociation of the bond, the S_0 and T_1 become almost degenerate. At this point, the lowest triplet state is mostly described by one configuration consisting of two singly occupied p_z-type orbitals at the two sulfur atoms (Fig. 21). The singlet ground state however, is composed of multiple configurations with similar weights, reinforcing the necessity of a multi-configurational method.

In addition, both the $T_{1,short}$ and $T_{1,long}$ could be localized with CASPT2. The $T_{1,short}$ is characterized by an S-S bond length of 2.07 Å (2.08 Å in TD-DFT) and an energy gap to the ground state of 2.74 eV (1.99 eV in TD-DFT). One might ask, why there is a $T_{1,short}$ minimum for the free ligand, if this minimum is characterized by MLCT in the complex. This is explained by the fact, that the ligand has to have a minimum structure on its own for the complex to be minimal,

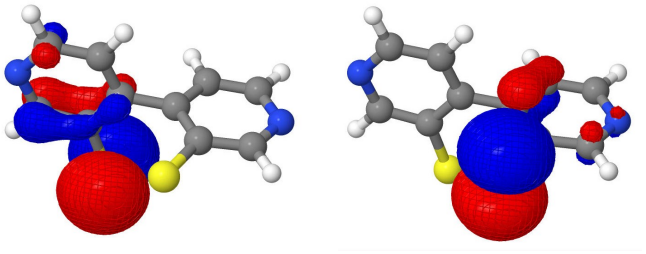

Figure 21: The two singly occupied p_z-type orbitals of the triplet state in the dissociation limit obtained by CASPT2(12,12).

since the ligand is not involved in the charge transfer.

The $T_{1,long}$ shows an S-S bond length of 2.56 Å (2.57 Å in TD-DFT) and an S_0-T_1 energy gap of 0.88 eV (0.56 eV in TD-DFT). This shows, that the CASSCF optimized geometries are very similar to the ones obtained by TD-DFT. However, the energy gaps to the ground state are higher for the CASPT2 computed ones by about 0.3 - 0.8 eV.

The crossing point of S_0-T_1 can still be easily reached from $T_{1,long}$ with an energy barrier of about 0.16 eV to overcome (seen in Fig. 20). The previously proposed relaxation mechanism still seems feasible based on the CASPT2 results. In addition, dissociation of the S-S bond also appears to be an option for the free ligand $^{S\text{-}S}$bpy. Whether this would also apply to the bound situation in the complex cannot be confirmed at this point.

4.9.2 TD-DFT

Density functional theory is a single-reference method, thus only one configuration of electrons can be considered. During homolytic dissociation however, a multi-configurational ansatz is necessary to accurately describe the electronic wavefunction, especially for the singlet case, as shown above. The necessity for multi-configurational treatment is seen by comparing the potential energy curves obtained by CASPT2 and TD-DFT in Figure 20. The T_1 is described fairly well by TD-DFT even for longer S-S bond lengths, shown by its similarities to the CASPT2 curve. The S_0 on the other hand increases in energy upon bond elongation even beyond the triplet state, which is not observed by CASPT2. Thus, the single-configuration description is not sufficient to describe the singlet ground state behaviour. This leads to a S_0-T_1 crossing point at shorter bond lengths compared to CASPT2, facilitating relaxation back to the ground

state in favour of dissociation. Additionally, the dissociation energy from the $T_{1,long}$ geometry is increased to roughly 0.4 eV compared to the 0.16 eV obtained by CASPT2. This could be the reason, why no dissociation but rather oscillation around $T_{1,long}$ is seen in the TD-DFT/SH dynamics. However, it cannot be confirmed if dynamics simulations using CASPT2 would produce different results.

4.9.3 LVC

Lastly, the LVC model potentials show different behavior at elongated S-S bond lengths than the ones obtained by TD-DFT and CASPT2. The excited PESs are approximated based on the harmonic ground state normal modes. As a consequence, large distortions of the structure lead to increasingly high energies. Thus, elongation of the S-S bond is only possible to a certain point as the potential energies increase steeply. On the one hand, this prohibits dissociation of the S-S bond. On the other hand, the S_0-T_1 crossing point lies at artificially high energies, making it not reachable from the T_1 minimum. Therefore, none of the proposed relaxation pathways to the ground state are possible within the framework of LVC. The observed population of S_0 in the LVC dynamics should only be considered with caution. The steep potentials also push the $T_{1,long}$ minimum to lower S-S bond lengths of 2.25 Å.

To conclude, near the FC region TD-DFT produces similar results to CASPT2 and is a good approximation for the electronic behaviour. Going to higher S-S bond lengths, the description of the S_0 becomes less accurate, whereas the T_1 is still described fairly well. In consequence, dissociation of the bond cannot be simulated accordingly with TD-DFT. However, the second possible relaxation pathway over the S_0-T_1 crossing point can be described similarly to CASPT2. At this point of the study, both relaxation pathways - dissociation and recovering of the FC structure - are possible mechanisms for $[Re^{I}(CO)_3(bpy)(^{S\text{-}S}bpy)]^+$ upon excitation. Lastly, LVC cannot describe either of those pathways due to overestimated potential energy barriers. But the dynamics near the FC region can still be approximated quite well by using LVC.

4.10 Comparison to the Experiments

Here all theoretical results will be compared to known experimental data to assess the performance of the computational methods and combine theory and experiment to propose a complete photo-initiated relaxation mechanism.

4.10.1 UV-Vis Absorption Spectra

Based on PBE0/D4/SARC-ZORA-TZVP (Re), ZORA-def2-TZVP (C, O, N, S, H) calculations in gas phase for a Wigner ensemble of 550 geometries, an UV-Vis absorption spectrum was simulated. Compared to the experimental spectrum, the shape could be reproduced nicely. Regarding energies, the calculated spectrum was shifted to lower energies with deviations ranging from 0.3 - 0.6 eV. The lower energy region of the spectrum (2.5 - 3.2 eV) was assigned to predominant M'LCT transitions. In the range of the bright absorption peak (3.2 - 3.7 eV) the character shifts to include more contributions of M'L^{S}CT. Thus, depending on the excitation wavelength, the charge flow of the system can be tuned.

4.10.2 Emission Spectra

$[Re^{I}(CO)_3(bpy)(^{S\text{-}S}bpy)]^+$ shows luminescence in the visible range, with a maximum at 573 nm (Fig. 22).[78] The large stokes shift and the structureless shape of the emission band suggests phosphorescence from an MLCT dominated state.[79] The originally found minimum $T_{1,long}$ was not able to describe the emission behaviour in a satisfactory manner, with a S_0-T_1 energy gap of 0.56 eV (2214 nm). Thus, a second T_1 minimum was proposed, discovered through the dynamics simulations - $T_{1,short}$. Based on PBE0/D4/SARC-ZORA-SVP (Re), ZORA-def2-SVP (C, O, N, S, H) calculations, $T_{1,short}$ has a phosphorescence energy of 1.99 eV. The character of the transition is dominated by M'LCT. More precisely, the NTOs show highest contributions of a Re d-orbital and CO π-orbitals in the hole component and 2,2'-bpy π*-orbital in the electron component. Such MLCT states are known to produce broad, structureless emission bands, as seen in experiment.[79] In conclusion, $T_{1,short}$ is able to explain the luminescence behaviour of $[Re^{I}(CO)_3(bpy)(^{S\text{-}S}bpy)]^+$ regarding emission energy, peak shape, and transition character. Therefore, $T_{1,short}$ is concluded to be the emissive triplet minimum.

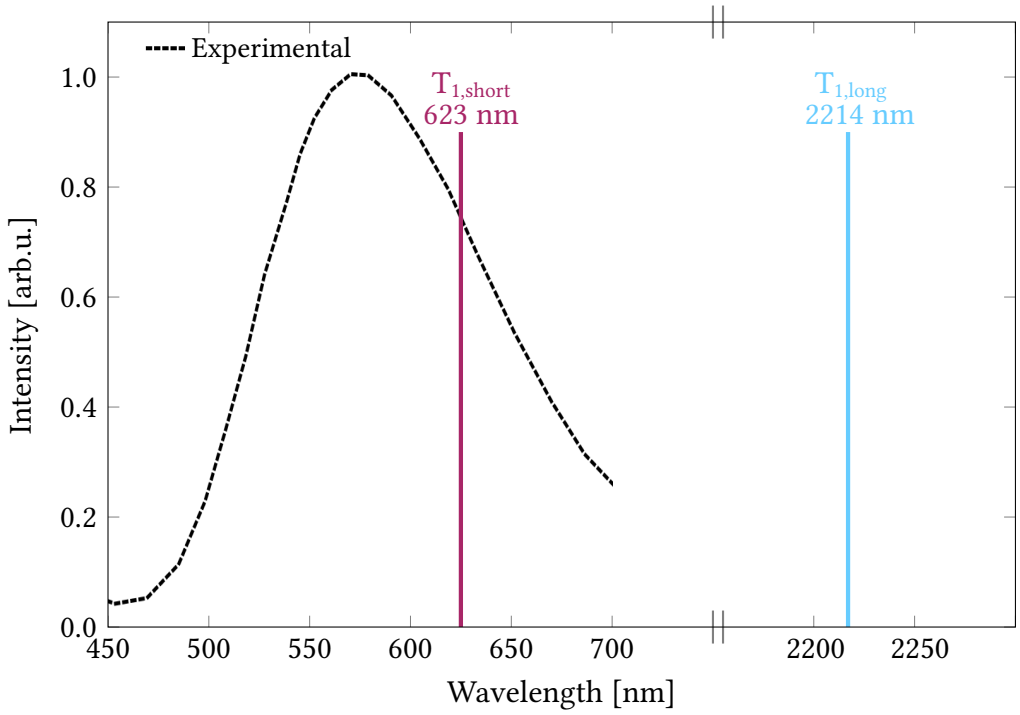

Figure 22: Experimental emission spectrum[78] (black, dashed) together with the calculated S_0-$T1_1$ energy differences for $T_{1,short}$ (purple) and $T_{1,long}$ (blue).

4.10.3 Time-Resolved Infrared Spectra

The ground state infrared (IR) spectrum[84] of $[Re^{I}(CO)_3(bpy)(^{S\text{-}S}bpy)]^+$ in the region of CO-stretching frequencies (1850 - 2150 cm^{-1}) shows two bands located at 1930 cm^{-1} and 2035 cm^{-1} respectively (Fig. 23a). Such bands are typically labelled according to their symmetry in C_S symmetric Re tricarbonyl diimine complexes.[79] Although $[Re^{I}(CO)_3(bpy)(^{S\text{-}S}bpy)]^+$ has C_1 symmetry we will keep the labelling of the bands for better comparison. The first broad band (1930 cm^{-1}) belongs to two asymmetric stretching motions involving only the equatorial CO ligands (A") for one and all three CO ligands (A'(2)) for the other. The second band (2035 cm^{-1}) can be attributed to the symmetric stretching involving all CO ligands (A'(1)). Time-resolved IR (TRIR) spectroscopy[84] (Fig. 23b) reveals a blue-shift of the CO stretching frequencies upon excitation with 400 nm. The low-energy band is split into three distinct bands located at 1960 - 1970 cm^{-1}, 2000 cm^{-1}, and 2030 cm^{-1} respectively. Blue-shift is also seen for the high-energy band to 2050 - 2065 cm^{-1}. Over time, ground state recovery and further blue-shift of the excited bands is seen, especially for the A'(1) band. After about 190 ps, 90% of the ground state has recovered, with a time constant of τ = 21 – 27 ps. About 10% of intensity still remains for the

bands at 1970 cm^{-1}, 2030 cm^{-1}, and 2065 cm^{-1}.

In order to simulate the IR spectra of $[Re^{I}(CO)_3(bpy)(^{S\text{-}S}bpy)]^+$, vibrational frequencies at the FC, the $T_{1,short}$, and $T_{1,long}$ geometries were computed. To accommodate for the errors made by calculating frequencies based on DFT in organometallic complexes, a scaling factor of 0.955 [85] was applied. Figure 23c shows the computed frequencies for the ground state S_0 (green), $T_{1,short}$ (purple), and $T_{1,long}$ (blue) geometries respectively. The predicted CO stretching frequencies for the ground state show a similar distribution to the experimental spectrum. The two lowest frequency bands A" and A'(2) are located in close proximity to each other at 1966 cm^{-1} and 1979 cm^{-1}, and the A'(1) vibration is calculated to be 2049 cm^{-1}. Beyond the usual error obtained by DFT, our model shows an additional systematic shift to higher energies of around 30 cm^{-1}.

$T_{1,long}$ predicts the blue-shift of the IR absorption bands as seen in the experimental spectrum. The calculated peaks are located at 2001 cm^{-1}, 2013 cm^{-1}, and 2082 cm^{-1}. The two low-frequency bands are in close proximity similar to the ground state ones.

The $T_{1,short}$ on the other hand, shows blue-shifted vibrations in addition to a splitting of the two asymmetric stretching bands. CO frequencies of 2018 cm^{-1}, 2050 cm^{-1}, and 2109 cm^{-1} were obtained. For $T_{1,short}$ the two lowest-frequency bands show significant splitting and seem to be better separated than the respective S_0 and $T_{1,long}$ bands.

Based on the calculated frequencies and the time evolution of the experimental spectrum, the following assumptions were made. Intensity loss of the excited state peaks can be attributed to relaxation to the ground state exclusively from the $T_{1,long}$ geometry through a S_0/T_1 crossing point on a time scale of $\tau = 21 - 27$ ps. Any remaining intensity is caused by the long-lived population in the $T_{1,short}$ minimum, which most likely relaxes to the ground state via phosphorescence on a longer time scale. Based on the results from LVC/SH dynamics and the ground state recovery of approximately 90%, the equilibrated population of the two T_1 minima, is estimated to be 90% $T_{1,long}$ and 10% $T_{1,short}$. Lastly, temporal blue-shift of certain bands can be caused by solvent relaxation as often discussed in literature.[86–88] Thus, the experimental bands can be assigned as follows (Fig. 23d).

- 1960 - 1970 cm^{-1} : This band consists of an overlap of the A" vibrations of $T_{1,short}$ and $T_{1,long}$, indicated by its broad nature and long-lived intensity of 10%.
- 2000 cm^{-1} : No remaining intensity after 1000 ps allows to attribute this band exclusively

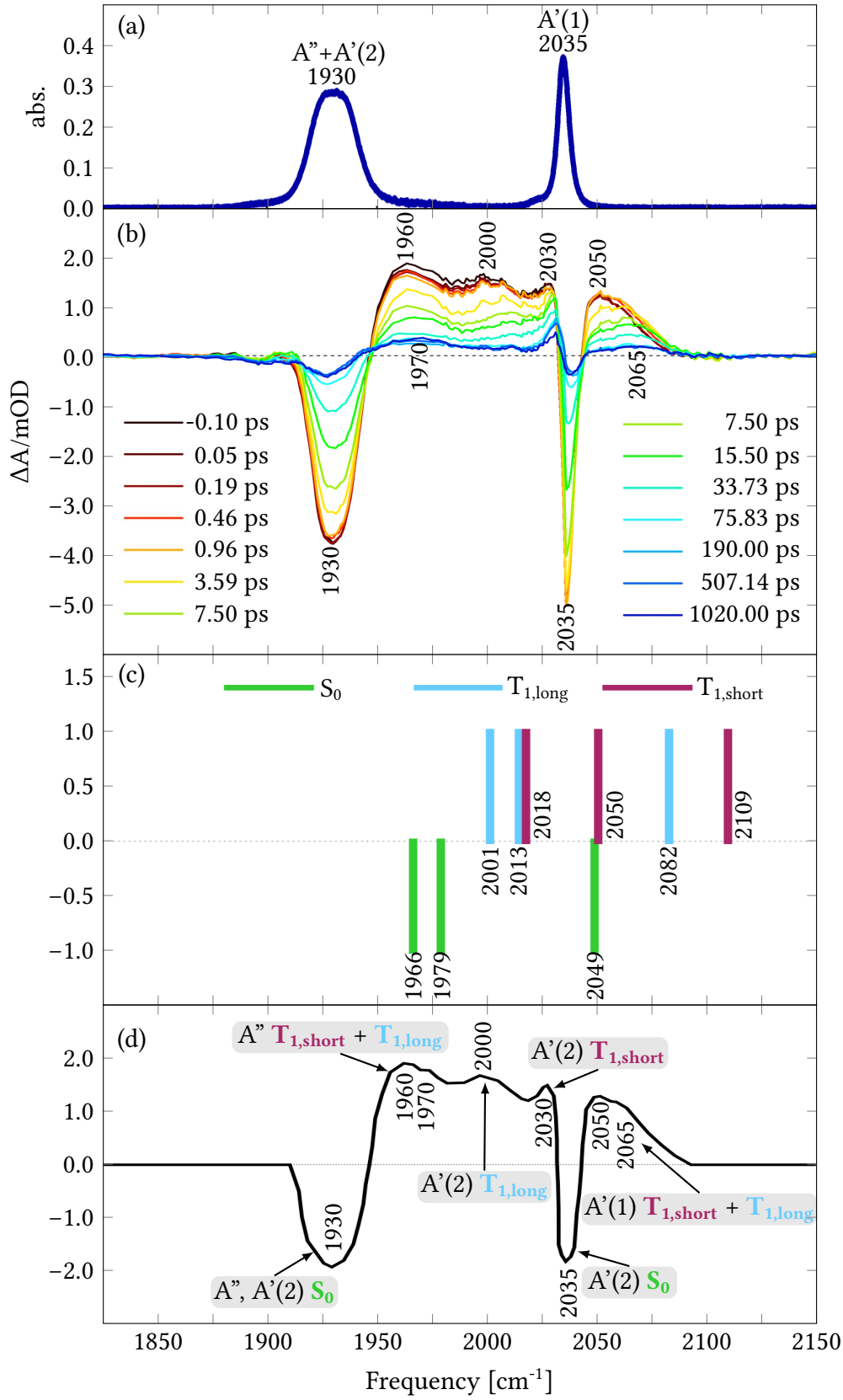

Figure 23: (a) Steady-state IR spectrum of $[Re^{I}(CO)_3(bpy)(^{S\text{-}S}bpy)]^+$.[84] (b) Difference Time-resolved IR-spectra after excitation at 400 nm. Negative peaks belong to the bleached ground state, positive values correspond to excited states.[84] (c) Computed CO frequencies for the FC, $T_{1,long}$, and $T_{1,short}$ geometries. (d) Scheme for the assignment of the experimental bands.

to the A'(2) band of $T_{1,long}$.

- 2030 cm^{-1} : Based on the calculated frequencies and the remaining intensity at this frequency, this band belongs to the A'(2) band of $T_{1,short}$. The loss in intensity within the first hundreds of ps can be assigned to the overlap with the broad bands of $T_{1,long}$.

- 2050 - 2065 cm^{-1} : This peak belongs to the A'(1) vibration of both $T_{1,long}$ (2050 cm^{-1}) and $T_{1,short}$ (2065 cm^{-1}). The observed blue-shift over longer times is most likely a combination of solvent relaxation and relaxation of $T_{1,long}$ to the ground state. At first glance, one might think that this band consists of only one peak, which shifts over time to higher frequencies. However, the remaining intensity indicates that the $T_{1,short}$ band overlaps with the $T_{1,long}$ one, with the $T_{1,short}$ accounting for the right-most peak in the band.

The clear assignment of peaks to either $T_{1,short}$, $T_{1,long}$ or both indicates that thermal equilibrium is already reached within the time scale of the measurements. This puts the population of the two triplet minima within a time frame of 100 fs to 1 ps. Time constants for the population of the T_1 obtained by theoretical dynamics of $k_T = 185 - 250$ fs agree nicely with the experimental observations.

5 Conclusion

$[Re^{I}(CO)_3(bpy)(^{S\text{-}S}bpy)]^+$ is a newly designed complex, proposed to operate dual photo-induced proton-coupled electron transfer. The goal is to reversibly reduce the two sulfur atoms and subsequently protonate both to yield the dithiol. Ideally, these protons can then be transferred to an acceptor unit and the disulfide complex can be recovered. The initial electron transfer is initiated by radiation with light in the visible range (370 nm). Herein, it is essential to understand the excited state dynamics of $[Re^{I}(CO)_3(bpy)(^{S\text{-}S}bpy)]^+$ in terms of laying the underlying mechanisms and thus aid experimental research.

In the framework of this thesis, the initial photo-excitation and subsequent dynamics were investigated by computational chemistry methods. After establishing a suitable level of theory with PBE0/D4/SARC-ZORA-TZVP (Re), ZORA-def2-TZVP (C, O, N, S, H), the absorption spectrum of $[Re^{I}(CO)_3(bpy)(^{S\text{-}S}bpy)]^+$ was simulated. The shape and energies of the absorption spectrum were reproduced by TD-DFT with an approximate deviation of 0.5 eV compared to experimental values. More important, it was revealed, that upon excitation at 370 nm, a transition from the $Re(CO)_3$ fragment to the 2,2'-bpy ligand (M'LCT) occurs. However, by increasing the excitation energy, the charge flow within the system changes and more electron contribution is transferred to the sulfur decorated ligand $^{S\text{-}S}$bpy. Depending on the desired product, the excitation wavelength can be tuned to steer the initial excitation within $[Re^{I}(CO)_3(bpy)(^{S\text{-}S}bpy)]^+$.

The excited state dynamics following the photo-excitation were investigated using trajectory surface hopping together with TD-DFT and a parametrized LVC model. The system is excited into higher-lying singlet states (S_n), which already show highly mixed spin character. From there, ultrafast intersystem crossing ($\tau_{ISC} = 18 - 25$ fs) to the triplet manifold occurs. Here, the system relaxes to the lowest-lying triplet state ($\tau_T = 185 - 250$ fs), where two different T_1 minima can be found, labelled as $T_{1,short}$ and $T_{1,long}$.

The $T_{1,short}$ minimum is characterized by a geometry close to the FC geometry, a S_0-T_1 energy gap of 1.99 eV, and M'LCT character. Based on these findings, $T_{1,short}$ was established to be the emissive species responsible of the experimental phosphorescence with a time constant of

τ_{phosp} = 270 ns. Estimated by TRIR spectroscopy, roughly 10% of the initially excited population ends up in the long-lived $T_{1,short}$.

The $T_{1,long}$ shows an elongated S-S bond of 2.57 Å. The energy gap to the ground state is 0.56 eV, due to the destabilization of the ground state PES upon bond elongation. The character of the $S_0 \rightarrow T_1$ transition is exclusively localized on the sulfur decorated ligand. Electron density is transferred to the anti-bonding σ^* orbital located at the S-S bond, aiding elongation of the bond. Based on TD-DFT and CASPT2 computations, a S_0/T_1 crossing point is in close proximity to the $T_{1,long}$ geometry ($\Delta E_{T1_{long}-MECP}$ = 0.14 – 0.16 eV) and can be reached by further S-S bond elongation. Additionally, CASPT2 calculations revealed the possibility for dissociation of this bond, as S_0 and T_1 become degenerate at high bond lengths. This points to two possible relaxation mechanisms of $T_{1,long}$. Either dissociation of the S-S bond yields a diradical photo-product or the equilibrium starting geometry is reformed over radiationless relaxation through the S_0/T_1 crossing point. TRIR spectroscopy reveals recovery of the ground state up to 90% with a time constant τ = 21 – 27 ps. This suggests that relaxation through the crossing point is the major relaxation channel for $[Re^{I}(CO)_3(bpy)(^{S\text{-}S}bpy)]^+$. However, formation of a photo-product in small amounts via dissociation cannot be excluded.

Lastly, a minor relaxation channel over the S_1 state to the singlet ground state was observed in the dynamics computations. Such pathway cannot be confirmed by any of the experimental observables available so far. Thus, no definite conclusion about such a relaxation pathway can be made.

The above-mentioned relaxation mechanism of $[Re^{I}(CO)_3(bpy)(^{S\text{-}S}bpy)]^+$ after photo-induced excitation with 370 nm is condensed in Figure 24. It encompasses theoretical and experimental results and shows where both can be combined.

To conclude, excitation of $[Re^{I}(CO)_3(bpy)(^{S\text{-}S}bpy)]^+$ with 370 nm leads to a charge transfer from the Re center and the three carbonyl ligands to the equatorial 2,2'-bipyridyl ligand. The initial excitation populates various excited singlet states. Ultrafast ISC transfers the population to the triplet manifold. Roughly 10% accumulates in a long-lived M'LCT characterized state ($T_{1,short}$), from where phosphorescence is observed. The remaining population experiences S-S bond elongation and eventually relaxes back to the ground state non-radiatively via a crossing point.

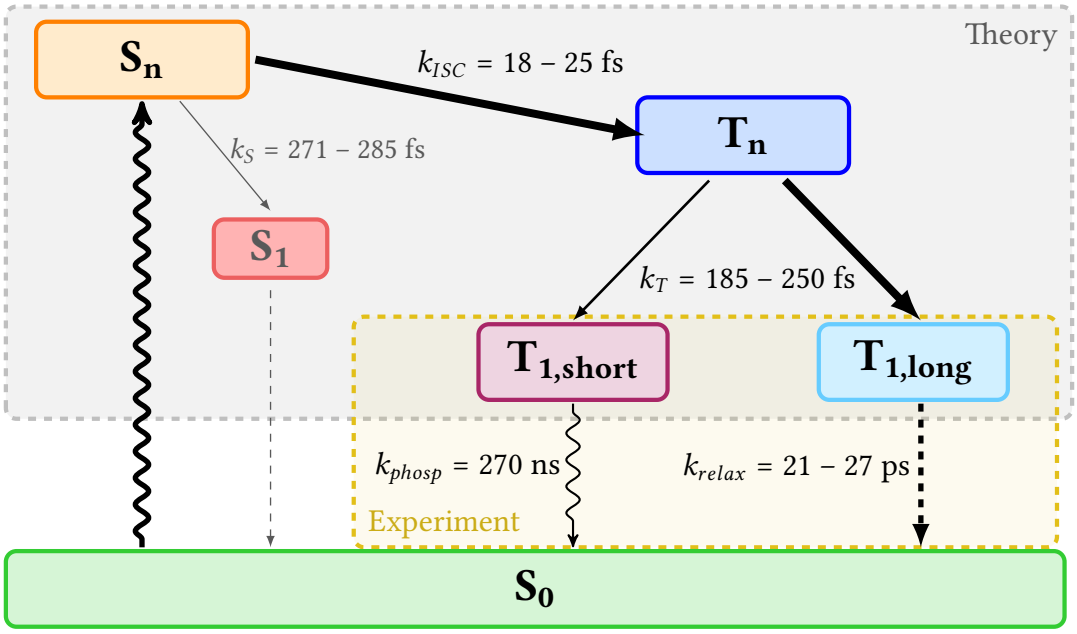

Figure 24: Overall relaxation mechanism of $[Re^{I}(CO)_3(bpy)(^{S\text{-}S}bpy)]^+$ upon excitation at 370 nm. Optical excitations of the S_0 leads to population of excited singlet states S_n. From there, the main relaxation channel experiences ultra-fast intersystem crossing to excited triplet states T_n. Here the majority of population is transferred to a locally excited triplet minimum $T_{1,long}$. Subsequently, the ground state is recovered radtionless over a S_0/T_1 crossing point. A smaller portion of the triplet manifold accumulates in a long-lived minimum $T_{1,short}$, from which phosphorescence back to the ground state occurs. Lastly, a minor reaction channel over the S_1 to the ground state is observed. Gray and yellow boxes indicate theoretical and experimental results respectively. Arrow thickness is in accordance to the importance of the respective pathway. Arrow types correspond to different transitions: wavy - radiative transitions, solid - non-radiative transitions within the excited states, and dashed - non-radiative relaxation to the ground state.

The experimental goals are to use $[Re^{I}(CO)_3(bpy)(^{S\text{-}S}bpy)]^+$ in photo-induced PCET reactions, preferable including reduction and protonation of the sulfur atoms. The theoretical results show that electron transfer to the sulfur moiety should occur for the majority of species. This facilitates the possibility of further reactions at the sulfur atoms upon introduction of a proton donor unit. Therefore, based on theoretical results, around 90% of the electronically excited population is able to reach a possible starting point, i.e. the $T_{1,long}$, for the desired PCET reactions.

References

[1] C. S. Sevier and C. A. Kaiser, *Nature Reviews. Molecular Cell Biology*, 2002, **3**, 836–847.

[2] C. H. Lillig and C. Berndt, *Antioxidants & Redox Signaling*, 2013, **18**, 1654–1665.

[3] P. Nagy, *Antioxidants & Redox Signaling*, 2013, **18**, 1623–1641.

[4] D. M. Ferrari and H.-D. Söling, *Biochemical Journal*, 1999, **339**, 1–10.

[5] B. Wilkinson and H. F. Gilbert, *Biochimica et Biophysica Acta*, 2004, **1699**, 35–44.

[6] F. Mohammadi, A. Soltani, A. Ghahremanloo, H. Javid and S. I. Hashemy, *Cancer Chemotherapy and Pharmacology*, 2019, **84**, 925–935.

[7] J. Nordberg and E. S. Arnér, *Free Radical Biology and Medicine*, 2001, **31**, 1287–1312.

[8] M. Cattaneo, C. E. Schiewer, A. Schober, S. Dechert, I. Siewert and F. Meyer, *Chemistry - A European Journal*, 2018, **24**, 4864–4870.

[9] C. Kaes, A. Katz and M. W. Hosseini, *Chemical Reviews*, 2000, **100**, 3553–3590.

[10] S.-A. Hua, M. Cattaneo, M. Oelschlegel, M. Heindl, L. Schmid, S. Dechert, O. S. Wenger, I. Siewert, L. González and F. Meyer, *Inorganic Chemistry*, 2020, **59**, 4972–4984.

[11] P. Dongare, A. G. Bonn, S. Maji and L. Hammarström, *Journal of Physical Chemistry C*, 2017, **121**, 12569–12576.

[12] G. B. Hall, R. Kottani, G. A. N. Felton, T. Yamamoto, D. H. Evans, R. S. Glass and D. L. Lichtenberger, *Journal of the American Chemical Society*, 2014, **136**, 4012–4018.

[13] M. Heindl, J. Hongyan, S.-A. Hua, M. Oelschlegel, F. Meyer, D. Schwarzer and L. González, *Inorganic Chemistry*, 2021, **60**, 1672–1682.

[14] C. K. Prier, D. A. Rankic and D. W. C. MacMillan, *Chemical Reviews*, 2013, **113**, 5322–5363.

[15] E. Schrödinger, *Phys. Rev.*, 1926, **28**, 1049–1070.

[16] *Quantum Chemistry and Dynamics of Excited States*, ed. L. González and R. Lindh, John Wiley & Sons, Ltd, 2020.

[17] A. Szabo and N. S. Ostlung, *Modern Quantum Chemistry*, Dover Publications, Inc., 1996.

[18] M. Born and R. Oppenheimer, *Annalen der Physik*, 1927, **389**, 457–484.

[19] C. J. Cramer and D. G. Truhlar, *Physical Chemistry Chemical Physics*, 2009, **11**, 10757–10816.

[20] W. Koch and M. C. Holthausen, *A Chemist's Guide to Density Funcional Theory*, John Wiley & Sons, Ltd, 2001.

[21] P. Hohenberg and W. Kohn, *Phys. Rev.*, 1964, **136**, B864–B871.

[22] W. Kohn and L. J. Sham, *Phys. Rev.*, 1965, **140**, A1133–A1138.

[23] F. Jensen, *Computational Chemistry*, John Wiley & Sons, Ltd, 2nd edn., 2007.

[24] E. G. Lewars, *Computational Chemistry - Introduction to the Theory and Applications of Molecular and Quantum Mechanics*, Kluwer Academic Publishers, 2003.

[25] E. Runge and E. K. U. Gross, *Phys. Rev. Lett.*, 1984, **52**, 997–1000.

[26] C. A. Ullrich, *Time-Dependent Density-Functional Theory*, Oxford University Press, 2011.

[27] *Fundamentals of Time-Dependent Density Functional Theory*, ed. M. A. Marques, N. T. Maitra, F. M. Nogueira, E. Gross and A. Rubio, Springer Berlin Heidelberg, 2012.

[28] *Time-Dependent Density Functional Theory*, ed. M. A. Marques, C. A. Ullrich, F. Nogueira, A. Rubio, K. Burke and E. K. U. Gross, Springer Berlin Heidelberg, 2006.

[29] M. E. Casida, in *Time-Dependent Density Functional Response Theory for Molecules*, ed. D. P. Chong, World Scientific, 1995, pp. 155–192.

[30] S. Hirata and M. Head-Gordon, *Chemical Physics Letters*, 1999, **314**, 291–299.

[31] J. Olsen, *International Journal of Quantum Chemistry*, 2011, **111**, 3267–3272.

[32] B. O. Roos, P. R. Taylor and P. E. Sigbahn, *Chemical Physics*, 1980, **48**, 157–173.

[33] R. J. Bartlett, *Annual Review of Physical Chemistry*, 1981, **32**, 359–401.

[34] K. Andersson, P. Malmqvist and B. O. Roos, *The Journal of Chemical Physics*, 1992, **96**, 1218–1226.

[35] H. Köuppel, W. Domcke and L. S. Cederbaum, in *Multimode Molecular Dynamics Beyond the Born-Oppenheimer Approximation*, John Wiley & Sons, Ltd, 1984, pp. 59–246.

[36] F. Plasser, S. Gómez, M. F. S. J. Menger, S. Mai and L. González, *Phys. Chem. Chem. Phys.*, 2019, **21**, 57–69.

[37] M. Fumanal, F. Plasser, S. Mai, C. Daniel and E. Gindensperger, *The Journal of Chemical Physics*, 2018, **148**, 124119.

[38] F. Plasser, M. Wormit and A. Dreuw, *Journal of Chemical Physics*, 2014, **141**, 024106.

[39] F. Plasser, *Journal of Chemical Physics*, 2020, **152**, 084108.

[40] J. C. Tully and R. K. Preston, *The Journal of Chemical Physics*, 1971, **55**, 562–572.

[41] L. Verlet, *Phys. Rev.*, 1967, **159**, 98–103.

[42] L. VERLET, *Phys. Rev.*, 1968, **165**, 201–214.

[43] F. Plasser, G. Granucci, J. Pittner, M. Barbatti, M. Persico and H. Lischka, *The Journal of Chemical Physics*, 2012, **137**, 22A514.

[44] J. C. Tully, *The Journal of Chemical Physics*, 1990, **93**, 1061–1071.

[45] N. L. Doltsinis, Computational Nanoscience: Do It Yourself!, 2006.

[46] G. Granucci, M. Persico and A. Zoccante, *The Journal of Chemical Physics*, 2010, **133**, 134111.

[47] M. Barbatti, *WIREs Computational Molecular Science*, 2011, **1**, 620–633.

[48] S. Mai, M. Richter, M. Heindl, M. F. S. J. Menger, A. Atkins, M. Ruckenbauer, F. Plasser, L. M. Ibele, S. Kropf, M. Oppel, P. Marquetand and L. González, *SHARC2.1: Surface Hopping Including Arbitrary Couplings — Program Package for Non-Adiabatic Dynamics*, sharc-md.org, 2019.

[49] S. Mai, P. Marquetand and L. González, *WIREs Computational Molecular Science*, 2018, **8**, e1370.

[50] M. Richter, P. Marquetand, J. González-Vázquez, I. Sola and L. González, *Journal of Chemical Theory and Computation*, 2011, **7**, 1253–1258.

[51] F. Neese, *WIREs Computational Molecular Science*, 2012, **2**, 73–78.

[52] F. Neese, *WIREs Computational Molecular Science*, 2017, **8**, e1327.

[53] C. Adamo and V. Barone, *The Journal of Chemical Physics*, 1999, **110**, 6158–6170.

[54] D. A. Pantazis, X.-Y. Chen, C. R. Landis and F. Neese, *Journal of Chemical Theory and Computation*, 2008, **4**, 908–919.

[55] F. Weigend and R. Ahlrichs, *Physical Chemistry Chemical Physics*, 2005, **7**, 3297–3305.

[56] E. Caldeweyher, S. Ehlert, A. Hansen, H. Neugebauer, S. Spicher, C. Bannwarth and S. Grimme, *The Journal of Chemical Physics*, 2019, **150**, 154122.

[57] F. Neese, F. Wennmohs, A. Hansen and U. Becker, *Chemical Physics*, 2009, **356**, 98–109.

[58] E. van Lenthe, J. G. Snijders and E. J. Baerends, *Journal of Chemical Physics*, 1996, **105**, 6505–6516.

[59] A. V. Marenich, C. J. Cramer and D. G. Truhlar, *The Journal of Physical Chemistry B*, 2009, **113**, 6378–6396.

[60] P. J. Stephens, F. J. Devlin, C. F. Chabalowski and M. J. Frisch, *The Journal of Physical Chemistry*, 1994, **98**, 11623–11627.

[61] T. Yanai, D. P. Tew and N. C. Handy, *Chemical Physics Letters*, 2004, **393**, 51–57.

[62] Y. Tawada, T. Tsuneda, S. Yanagisawa, T. Yanai and K. Hirao, *The Journal of Chemical Physics*, 2004, **120**, 8425–8433.

[63] Y. Zhao and D. G. Truhlar, *Theoretical Chemistry Accounts*, 2008, **120**, 215–241.

[64] O. Bokareva, *University of Rostock*, private communication.

[65] E. Wigner, *Physical Review*, 1932, **40**, 749–759.

[66] J. P. Zobel, J. J. Nogueira and L. González, *Physical Chemistry Chemical Physics*, 2019, **21**, 13906–13915.

[67] B. de Souza, G. Farias, F. Neese and R. Izsák, *Journal of Chemical Theory and Computation*, 2019, **15**, 1896–1904.

[68] N. Mardirossian and M. Head-Gordon, *Physical Chemistry Chemical Physics*, 2014, **16**, 9904–9924.

[69] *Jmol: an open-source Java viewer for chemical structures in 3D.*, `http://www.jmol.org/`.

[70] I. Fdez. Galván, M. Vacher, A. Alavi, C. Angeli, F. Aquilante, J. Autschbach, J. J. Bao, S. I. Bokarev, N. A. Bogdanov, R. K. Carlson, L. F. Chibotaru, J. Creutzberg, N. Dattani, M. G. Delcey, S. S. Dong, A. Dreuw, L. Freitag, L. M. Frutos, L. Gagliardi, F. Gendron, A. Giussani, L. González, G. Grell, M. Guo, C. E. Hoyer, M. Johansson, S. Keller, S. Knecht, G. Kovačević, E. Källman, G. Li Manni, M. Lundberg, Y. Ma, S. Mai, J. a. P. Malhado, P. r. Malmqvist, P. Marquetand, S. A. Mewes, J. Norell, M. Olivucci, M. Oppel, Q. M. Phung, K. Pierloot, F. Plasser, M. Reiher, A. M. Sand, I. Schapiro, P. Sharma, C. J. Stein, L. K. Sørensen, D. G. Truhlar, M. Ugandi, L. Ungur, A. Valentini, S. Vancoillie, V. Veryazov, O. Weser, T. A. Wesołowski, P.-O. Widmark, S. Wouters, A. Zech, J. P. Zobel and R. Lindh, *Journal of Chemical Theory and Computation*, 2019, **15**, 5925–5964.

[71] B. O. Roos, R. Lindh, P.-Å. Malmqvist, V. Veryazov and P.-O. Widmark, *Journal of Physical Chemistry A*, 2004, **108**, 2851–2858.

[72] F. Aquilante, R. Lindh and T. Bondo Pedersen, *The Journal of Chemical Physics*, 2007, **127**, 114107.

[73] G. Ghigo, B. O. Roos and P. Åke Malmqvist, *Chemical Physics Letters*, 2004, **396**, 142–149.

[74] N. Forsberg and P. Åke Malmqvist, *Chemical Physics Letters*, 1997, **274**, 196–204.

[75] M. Barbatti, M. Ruckenbauer, F. Plasser, J. Pittner, G. Granucci, M. Persico and H. Lischka, *WIREs Computational Molecular Science*, 2014, **4**, 26–33.

[76] F. Plasser, M. Ruckenbauer, S. Mai, M. Oppel, P. Marquetand and L. González, *Journal of Chemical Theory and Computation*, 2016, **12**, 1207–1219.

[77] J. N. Harvey, *Annual Reports Section "C" (Physical Chemistry)*, 2006, **102**, 203–226.

[78] F. Meyer, *University of Göttingen*, private communication.

[79] A. Vlček, in *Ultrafast Excited-State Processes in Re(I) Carbonyl-Diimine Complexes: From Excitation to Photochemistry*, ed. A. J. Lees, Springer Berlin Heidelberg, Berlin, Heidelberg, 2010, pp. 115–158.

[80] L. A. Worl, R. Duesing, P. Chen, L. D. Ciana and T. J. Meyer, *Journal of the Chemical Society, Dalton Transactions*, 1991, 849–858.

[81] S. Mai and L. González, *Chemical Science*, 2019, **10**, 10405–10411.

[82] A. Cannizzo, A. M. Blanco-Rodríguez, A. E. Nahhas, J. Šebera, S. Záliš, A. V. Jr. and M. Chergui, *Journal of the American Chemical Society*, 2008, **130**, 8967–8974.

[83] S. Nangia, A. W. Jasper, T. F. Miller and D. G. Truhlar, *The Journal of Chemical Physics*, 2004, **120**, 3586–3597.

[84] D. Schwarzer, *Max-Planck Institute, Göttingen*, private communication.

[85] L. Yu, G. Srinivas and M. Schwartz, *Journal of Molecular Structure: THEOCHEM*, 2003, **625**, 215–220.

[86] A. E. Nahhas, C. Consani, A. M. Blanco-Rodríguez, K. M. Lancaster, O. Braem, A. Cannizzo, M. Towire, I. P. Clark, S. Záliš, M. Chergui and A. V. Jr., *Inorganic Chemistry*, 2011, **50**, 2932–2943.

[87] A. M. Blanco-Rodríguez, M. Busby, C. Grădinaru, B. R. Crane, A. J. Di Bilio, P. Matousek, M. Towrie, B. S. Leigh, J. H. Richards, A. Vlček and H. B. Gray, *Journal of the American Chemical Society*, 2006, **128**, 4365–4370.

[88] D. J. Liard, M. Busby, P. Matousek, M. Towrie and A. Vlček, *The Journal of Physical Chemistry A*, 2004, **108**, 2363–2369.

[89] J. P. Zobel, J. J. Nogueira and L. González, *Chemical Science*, 2017, **8**, 1482–1499.

A Appendix

A.1 CASSCF / CASPT2

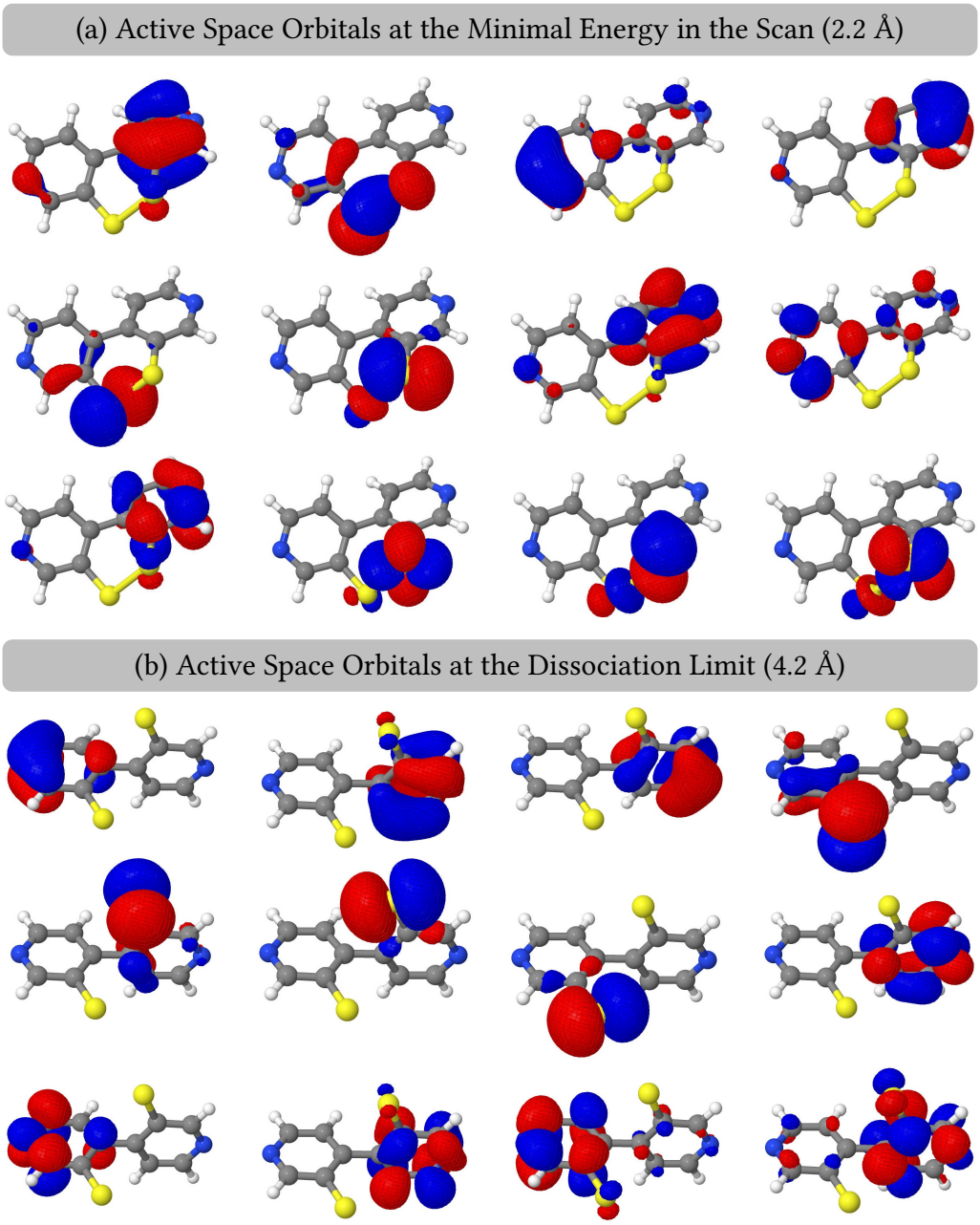

Figure A1: Orbitals included in the active space during the CASSCF/CASPT2 computations at (a) the minimum geometry of the S-S scan (2.2 Å, see Fig. 20) and (b) at the dissociation limit (4.2 Å).

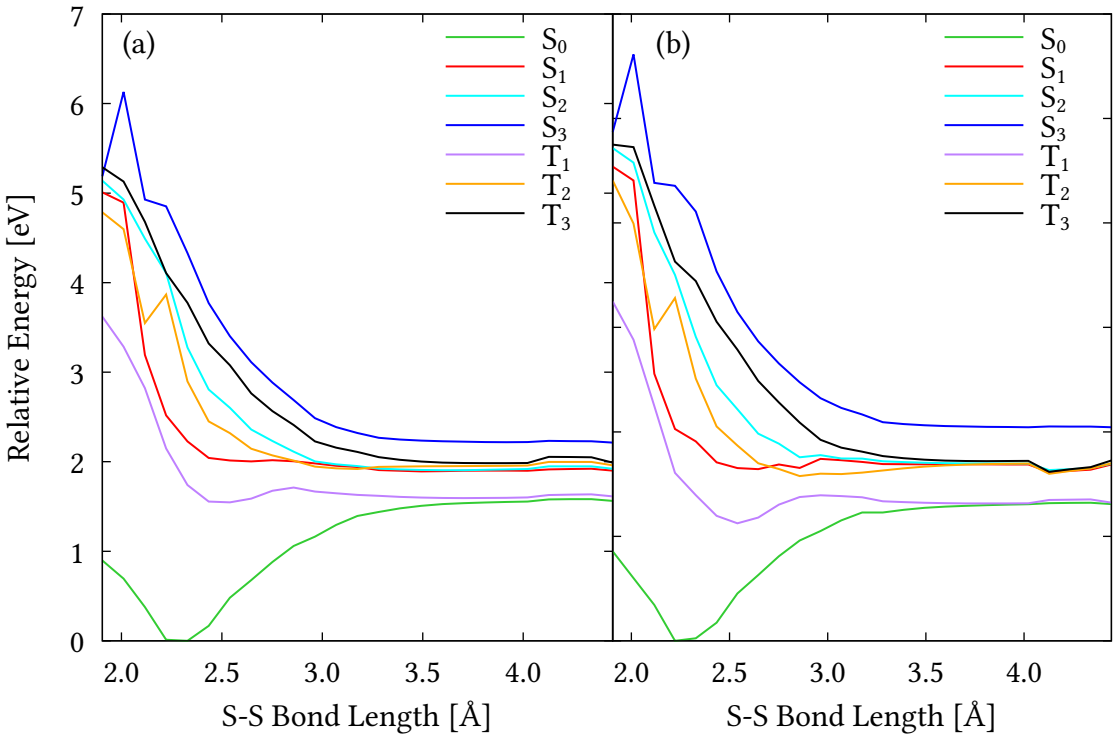

Figure A2: Relaxed surface scan over multiple S-S bond lengths. The geometries were optimized using CASSCF(12,12) on the T_1. Subsequently MS-CASPT2(12,12) computations were performed including 4 singlet states and 3 triplet states. (a) Depicts the results of the MS-CASPT2 computations using an IPEA shift of 0.25 eV, (b) depicts the results without IPEA shift. It can be seen that the differences are marginal. The excitation energies (which are often badly described by the IPEA shift [89]) seem to not be influenced much by the IPEA for our system. Therefore, we include an IPEA shift of 0.25 eV in the computations in an effort to improve dissociation energies.

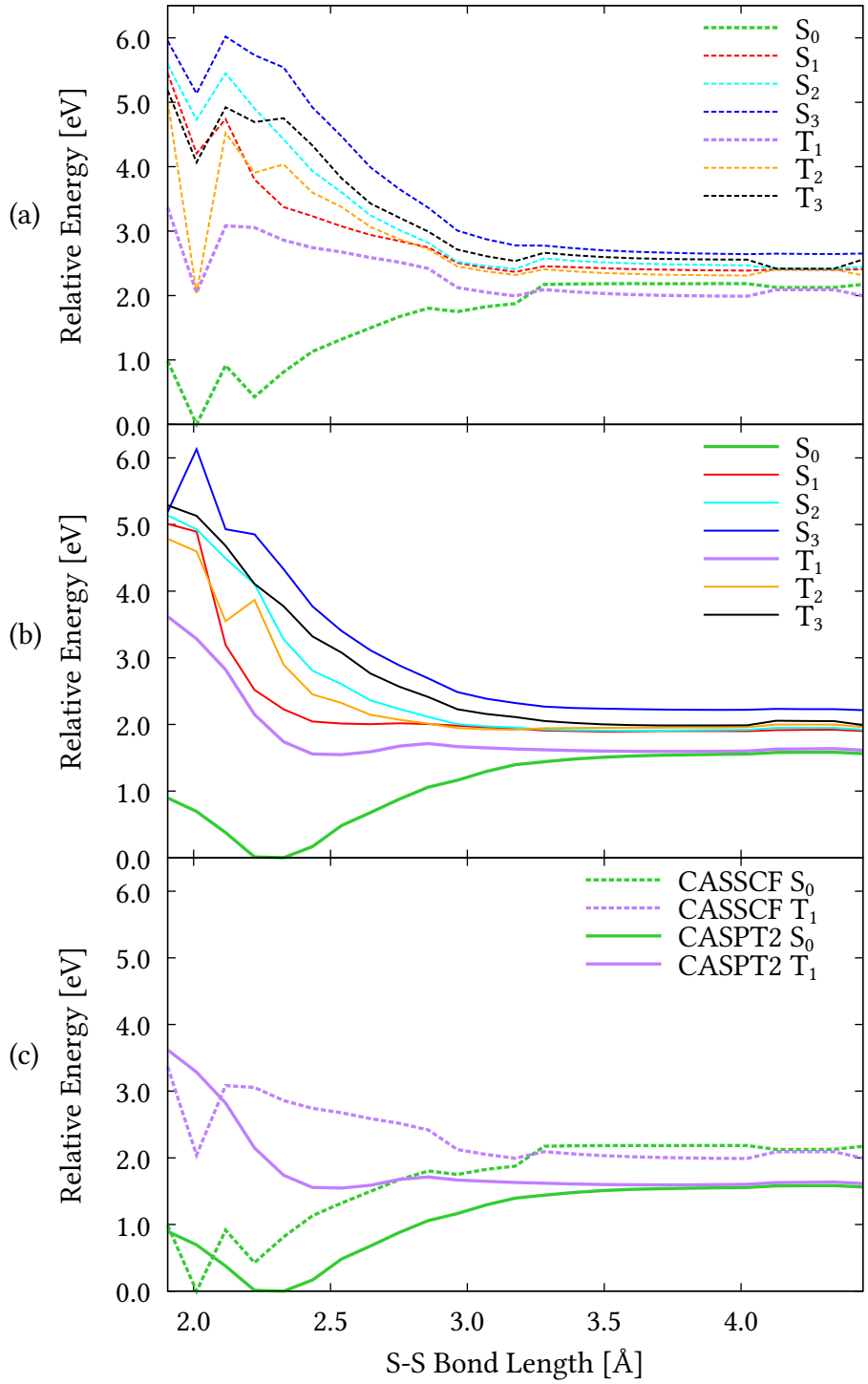

Figure A3: Relaxed surface scan over multiple S-S bond lengths. The geometries were optimized using CASSCF(12,12) on the T_1. Subsequently CASSCF (a, c dashed) and MS-CASPT2(12,12) (b, c continuous) computations were performed including 4 singlet states and 3 triplet states. It can be seen that the CASSCF computed energies do not provide smooth potential energy curves, due to state mixing. Neither the S_0, nor the T_1 ($T_{1,long}$) minimum can be located using CASSCF. The multi-state treatment of CASPT2, produces smooth curves.

A.2 Influence of the LVC/SH Parameters

Figure A5 shows the electronic populations of 500 example trajectories propagated with LVC/SH used to test various parameter settings in order to find the most appropriate settings for the dynamics. The parameters tested were:

- Damping: The total energy of the system was either damped at each time step with a certain damping factor (0.9999 or 0.99999) or no damping was applied.
- Stopping trajectories: The propagation was either stopped upon reaching the ground state S_0 and propagating there for 20 fs (called S_0quit) or the propagation was allowed to reach the end of the chosen simulation time regardless of active state (no S_0quit).
- Velocity rescaling: The velocity of the system was rescaled after a hop either based on the full velocity vector (v rescaling), or based on the NAC vector (NAC rescaling).

Panel (a) was propagated without damping, no S_0quit, and v rescaling. These trajectories were only propagated for 1000 fs. Comparing to panel (b) (0.9999 damping, no S_0quit, and v rescaling) shows that applying a damping of the energy slows down the population of the low-energetic excited states T_1 (violet) and S_1 (red). Furthermore, the population of the S_0 (green) within 100 fs is hindered.

Panel (c) shows the same trajectories as panel (b) (0.9999 damping, no S_0quit, and v rescaling) for a simulation time of 10 ps. Comparing panel (d) (0.9999 damping, S_0quit, and v rescaling) to panel (c) shows that stopping the simulation upon reaching the ground state S_0, accumulates population in the S_0. Thus, in panel (c) the trajectories hopped back from the ground state to higher excited states, which is not a realistic pathway.

In addition, panel (d) shows a decrease of the T_1 population in favour of the S_0. This happens because of the high amount of kinetic energy of the system when accumulating in the T_1. Since there is no relaxation pathway from the T_1 to the S_0 in the LVC/SH dynamics, eventually a hop to higher excited states can occur for trajectories that populate the T_1.

Next, panel (e) shows trajectories that were damped with a factor of 0.99999 (in contrast to 0.9999 discussed before), S_0quit, and v rescaling, which are the trajectories discussed in the main text. Comparing panel (d) and (e) shows that a higher damping factor (i.e. slower energy

loss) allows for faster population of low-lying states in the early dynamics. However, the unrealistic depopulation of the T_1 due to high kinetic energies is more abundant when applying less damping.

Lastly, panel (f) shows trajectories with a damping factor of 0.99999, S_0quit and NAC rescaling. Including NACs describes the early dynamics well and also hinders the depopulation of the T_1 over higher-lying excited states to a certain extend. However, they were not able to fully constrain the population in the T_1.

Based on the energies and population curves shown here, rescaling using the NACs looks the most promising. However, when analyzing the geometries of the trajectories displayed in panel (f) reveals that highly unrealistic distortions take place (Fig. A4). A common approach to this problem of LVC is to exclude certain normal modes in the model. Within this master thesis however, this problem was only discovered at the end of the project, thus no new model could be established in time. The other LVC/SH dynamics presented in Figure A5 did not show this problem of geometry distortion. Therefore, the parameters shown in panel (e), 0.99999 damping, S_0quit, and rescaling based on the velocity vector, were deemed to be the best description for the system.

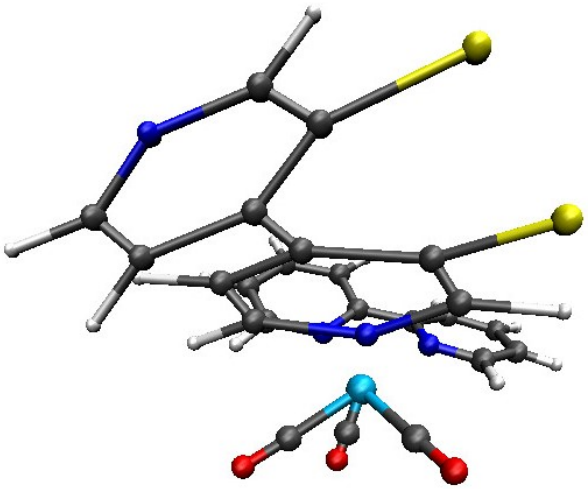

Figure A4: Example geometry of a LVC/SH trajectory using NAC rescaling. Various different deformations were seen over all trajectories.

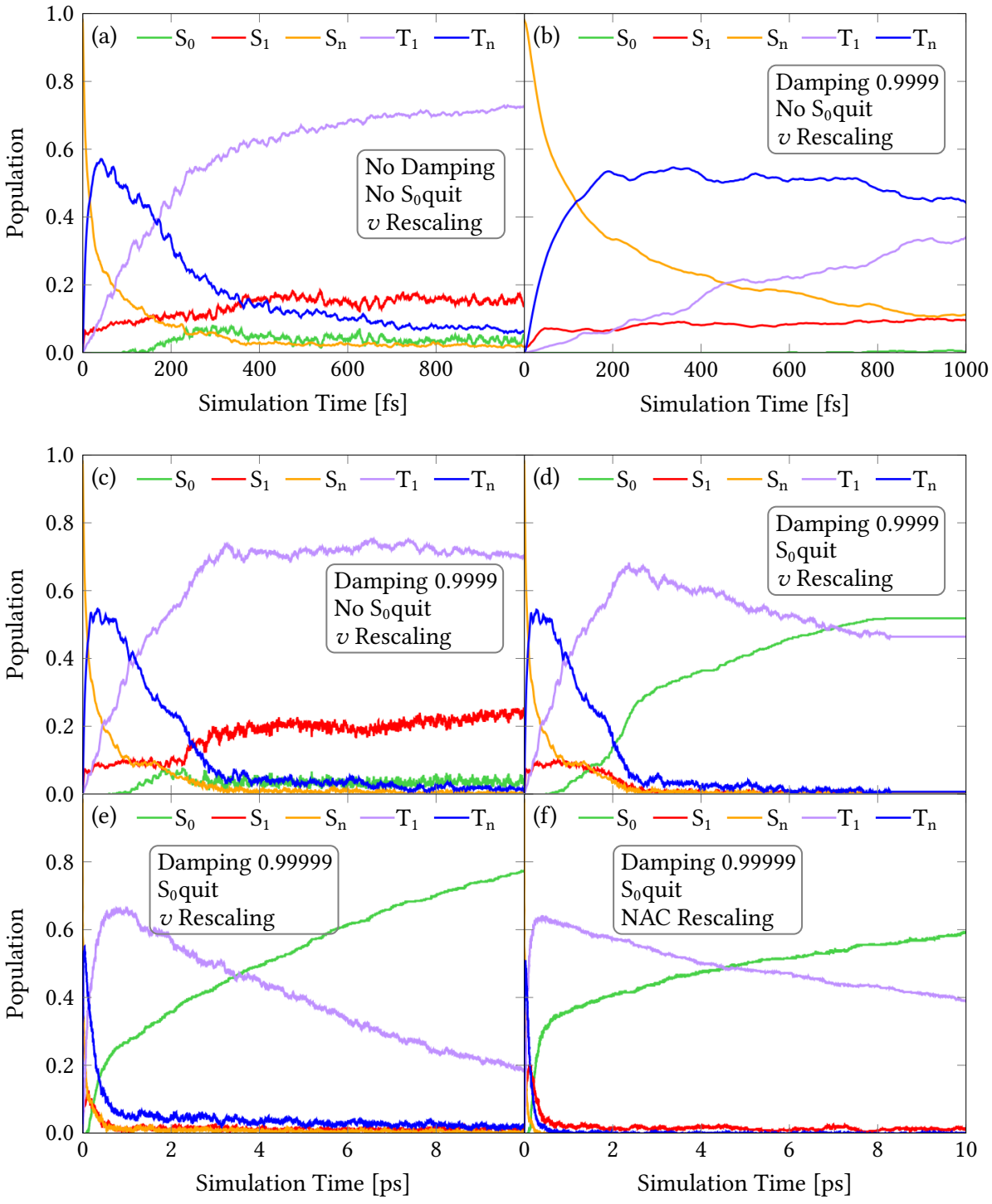

Figure A5: Electronic populations of 500 trajectories simulated with LVC/SH with (a) no damping, no S_0quit, v rescaling (1 ps). (b) 0.9999 damping, no S_0quit, v rescaling (1 ps). (c) same trajectories as in (b) for 10 ps. (d) 0.9999 damping, S_0quit, v rescaling (10 ps). (e) 0.99999 damping, S_0quit, v rescaling (10 ps). (f) 0.99999 damping, S_0quit, NAC rescaling (10 ps).

A.3 Spin-Orbit Coupling Matrix Elements

Table A1: Spin-orbit coupling matrix elements [cm^{-1}] for the optimized FC geometry including S_0-S_{30} and T_1-T_{15}

		Triplets														
	$[cm^{-1}]$	1	2	3	4	5	6	7	8	9	10	11	12	13	14	15
Singlets	0	44.4	246.0	208.7	82.1	115.4	24.1	27.9	95.1	129.2	80.3	51.9	106.3	36.2	6.3	24.5
	1	5.4	11.7	209.2	71.6	206.0	34.0	10.1	63.0	27.5	20.8	23.5	61.7	18.3	11.6	7.3
	2	19.2	242.0	693.6	298.1	757.5	9.8	8.4	5.2	12.7	5.6	6.4	14.0	51.4	15.7	12.8
	3	17.5	387.8	151.3	163.7	402.4	13.4	7.5	8.0	27.9	73.5	17.3	41.0	22.1	29.6	26.3
	4	20.9	795.4	627.2	126.3	395.6	4.2	3.9	29.5	50.3	212.9	8.2	57.5	33.6	22.6	53.3
	5	21.2	618.9	486.9	232.3	469.8	2.1	6.2	56.1	110.9	167.5	24.1	114.2	18.9	26.9	57.0
	6	79.6	20.7	25.8	15.7	29.5	391.1	386.7	394.2	196.8	11.7	196.3	866.8	118.5	2.0	23.0
	7	50.2	98.1	43.0	31.5	93.5	151.7	142.2	402.7	693.8	52.0	118.5	496.3	105.2	6.6	51.1
	8	16.0	16.3	9.2	11.0	14.1	148.0	140.5	260.6	411.8	35.8	85.1	144.7	52.6	3.5	18.7
	9	64.8	59.6	29.1	4.7	53.8	261.6	265.1	433.8	665.8	54.1	185.9	396.0	24.7	5.7	45.8
	10	9.4	10.6	11.7	41.1	33.2	22.9	28.0	46.3	70.4	6.9	20.8	55.9	6.9	0.7	4.1
	11	4.9	26.7	29.7	6.7	32.5	12.1	12.1	19.5	38.9	2.6	7.6	32.2	279.0	11.5	265.8
	12	17.8	36.4	29.2	8.3	39.0	10.3	16.7	11.2	31.2	3.6	10.7	39.9	61.0	17.1	19.0
	13	0.9	12.2	27.2	15.7	34.3	2.6	3.1	7.3	23.3	8.8	2.5	31.7	355.2	23.1	70.0
	14	6.1	61.3	12.1	22.4	51.8	8.9	8.1	10.8	39.5	5.3	7.8	25.8	481.8	50.5	285.7
	15	30.4	19.6	12.9	7.1	23.0	10.6	22.1	31.6	18.2	0.8	11.5	48.8	30.2	9.2	70.9
	16	4.4	32.7	31.5	8.5	23.8	3.2	3.5	18.1	31.5	21.0	2.9	17.0	153.2	12.3	617.8
	17	3.8	31.0	18.5	11.6	26.2	4.1	3.5	13.1	23.4	8.0	17.5	16.8	155.1	18.2	165.8
	18	5.8	33.5	33.1	8.7	56.3	17.5	16.3	22.0	49.6	50.7	12.0	30.2	382.6	30.2	465.0
	19	4.2	31.9	34.0	16.5	36.4	1.8	3.7	21.6	43.8	11.8	5.4	53.2	358.9	32.3	387.9
	20	5.2	81.5	32.1	27.9	103.5	12.6	15.8	42.1	86.6	77.7	14.2	93.1	195.8	13.9	302.2
	21	1.1	33.2	31.8	12.7	7.7	7.4	6.9	10.9	11.5	60.3	21.9	12.4	263.8	26.4	325.4
	22	10.7	8.6	39.0	8.2	17.3	29.2	26.0	30.7	30.8	9.4	40.9	18.6	34.6	3.9	25.2
	23	7.1	24.3	12.3	8.3	20.9	14.7	13.7	33.3	15.3	17.8	22.6	41.4	26.3	2.9	7.6
	24	1.1	96.2	47.7	41.2	87.8	6.2	6.4	7.3	1.9	32.4	7.3	4.8	8.2	5.9	20.9
	25	22.6	18.1	31.3	12.0	11.2	13.3	15.7	12.4	17.6	2.8	17.1	11.0	20.7	0.8	6.1
	26	6.9	44.0	82.1	19.3	23.6	31.5	35.6	23.9	43.9	3.8	6.8	24.2	43.8	5.3	3.7
	27	14.9	15.2	28.4	7.4	41.7	8.2	4.0	29.1	17.1	3.9	26.3	25.7	22.2	5.3	14.5
	28	16.2	80.9	42.1	10.3	23.0	8.8	9.5	43.6	66.9	33.3	16.2	9.4	11.5	3.0	42.6
	29	12.1	12.6	8.2	4.1	4.4	4.2	2.0	8.1	10.7	4.3	17.8	10.1	9.9	3.7	10.2
	30	32.5	44.6	24.6	29.5	35.4	6.1	6.8	7.7	15.4	12.8	12.1	19.8	8.4	15.9	19.5

Table A2: Continuation of Table A1 including the SOCMEs between S_0-S_{30} and T_{16}-T_{30} [cm^{-1}]

		Triplets														
	$[cm^{-1}]$	16	17	18	19	20	21	22	23	24	25	26	27	28	29	30
Singlets	0	95.2	14.8	75.2	44.2	124.7	157.8	75.8	48.6	87.6	636.7	648.0	615.4	453.1	208.2	494.1
	1	29.9	10.1	6.5	16.4	6.9	40.4	3.4	1.6	29.0	32.7	8.0	12.7	23.6	9.2	16.1
	2	11.9	36.2	27.6	16.0	29.4	18.1	17.4	6.3	9.4	106.6	13.1	17.0	28.9	11.6	37.1
	3	9.5	19.7	17.1	20.2	31.3	12.3	38.7	9.9	8.1	44.3	8.7	38.0	13.2	13.5	22.8
	4	14.5	31.7	43.2	17.0	43.5	23.1	43.4	10.7	4.6	21.5	37.3	95.0	28.3	13.2	10.3
	5	29.4	24.5	51.7	36.2	49.6	16.0	66.1	25.9	3.9	12.6	59.0	50.0	23.4	22.7	38.6
	6	342.1	24.3	32.7	77.9	30.0	142.4	19.9	34.7	31.3	98.8	5.6	13.9	25.3	10.6	31.5
	7	225.1	19.4	63.1	65.4	57.8	77.8	67.5	23.6	42.0	21.9	99.2	59.7	27.3	38.4	30.6
	8	142.6	10.8	14.9	33.6	11.5	54.4	9.7	12.3	27.4	8.2	39.2	28.2	9.7	7.1	18.8
	9	146.0	14.1	80.2	50.0	70.0	90.9	60.8	37.9	35.0	2.7	87.6	48.0	42.0	56.6	47.4
	10	14.6	17.2	5.2	7.7	3.8	11.4	5.7	2.0	3.9	2.7	9.1	6.0	3.2	5.0	7.8
	11	90.3	15.6	50.3	39.9	120.5	72.6	412.2	78.8	18.1	57.6	37.2	66.3	29.2	20.0	7.9
	12	14.2	3.1	27.8	22.9	72.9	14.9	86.6	26.9	12.0	33.1	38.3	44.2	17.9	13.2	10.2
	13	100.0	6.7	29.4	147.1	156.1	107.0	461.2	107.7	19.8	87.7	34.0	47.3	35.7	4.2	29.0
	14	140.8	11.5	47.2	290.1	42.4	177.0	628.0	149.8	25.9	95.0	115.2	119.7	17.2	27.2	8.9
	15	25.2	4.7	44.0	27.5	54.5	20.3	87.3	24.1	12.2	27.3	17.2	18.1	5.9	9.2	4.9
	16	61.4	28.1	84.5	149.8	40.3	51.4	482.3	101.1	19.2	101.7	234.2	256.9	46.0	97.8	15.6
	17	68.9	48.5	234.5	89.0	523.6	150.5	159.4	128.2	19.4	103.3	398.7	341.3	69.4	80.3	13.7
	18	108.2	46.1	501.5	305.7	222.6	206.0	124.6	183.9	23.4	76.9	348.9	308.1	90.4	149.8	17.7
	19	112.0	25.2	200.1	228.2	360.6	145.9	131.3	68.4	4.5	72.8	185.0	174.3	42.4	50.2	25.7
	20	83.3	36.8	379.8	181.1	460.1	117.9	201.3	91.5	25.5	64.3	463.4	470.8	120.8	225.7	10.0
	21	105.8	73.3	513.5	145.7	672.1	202.7	30.4	201.5	20.1	107.9	97.3	81.1	99.6	222.8	17.6
	22	46.1	5.3	51.3	24.2	45.4	101.1	119.6	37.6	19.0	552.6	253.4	298.1	230.7	97.1	186.9
	23	10.7	0.7	22.0	11.4	69.9	45.8	56.3	11.6	191.6	270.1	321.2	346.3	509.3	161.8	393.8
	24	10.2	6.1	37.4	12.3	42.3	8.9	33.2	4.4	17.2	115.6	75.4	48.6	53.7	36.5	47.5
	25	20.4	2.9	14.6	4.4	14.3	5.4	45.0	33.4	15.5	202.0	85.3	112.1	99.0	39.4	55.6
	26	54.7	4.2	46.1	20.4	73.0	7.6	105.7	85.0	26.0	516.2	268.5	263.7	176.7	85.1	134.1
	27	18.9	3.7	35.9	43.7	69.4	96.9	149.9	40.1	136.3	502.1	205.3	202.9	314.6	73.2	223.1
	28	6.1	4.2	54.8	24.6	40.4	21.1	21.7	27.3	15.6	60.4	446.9	444.1	188.9	130.8	385.0
	29	7.7	3.7	9.2	41.1	34.3	50.9	22.9	19.8	45.9	173.9	67.6	96.9	124.7	38.3	92.0
	30	10.7	17.0	28.8	11.0	45.5	29.5	28.7	23.1	43.8	177.3	89.2	124.1	123.7	42.3	102.9

Tables A1 and A2 depict the spin-orbit coupling matrix elements (SOCMEs) in [cm^{-1}] of the optimized Franck-Condon geometry of $[Re^{I}(CO)_3(bpy)(^{S\text{-}S}bpy)]^+$ at the PBE0/D4/SARC-ZORA-TZVP (Re), ZORA-def2-TZVP (C, O, N, S, H) level of theory between the singlet ground state and the 30 lowest lying singlet excited states and the 30 lowest lying excited triplet states. The SOCs were calculated using quasi-degenerate perturbation theory as implemented in *ORCA4.2.1*

A.4 LVC Absorption Spectra

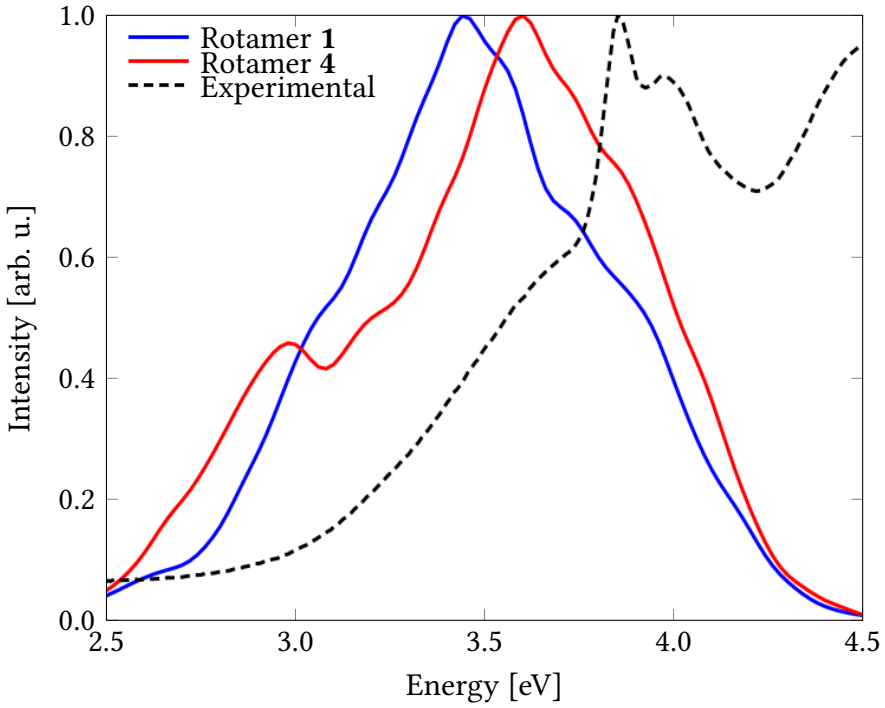

Figure A6: Computed absorption spectra (see also Fig. 6) from two LVC models based on rotamer **1** (blue) and rotamer **4** (red), compared to the experimental spectrum (black, dashed). The spectrum of rotamer **1** shows even further red-shift of the absorption energies compared to rotamer **4**. Furthermore, the spectrum of rotamer **4** resembles the shape of the experimental spectrum more closely. Thus, considering only rotamer **4** in the dynamics should be able to describe the electronic properties of the system.

A.5 TD-DFT/SH Dynamics

Figure A7 shows one of the excluded trajectories due to the unrealistic hop to high energies. The hop occurred at $t = 26\,\mathrm{fs}$. Figure A7a shows the singlet and triplet states in the adiabatic representation, the active state is indicated by a circle. The diagonal states are shown in Figure A7b. The hopping probability is seen in Figure A7c, color coded for the various states. The drawn random number is indicated by a triangle. The probability of the chosen state is shown in blue and is roughly 0.0007%. Such hops with small probabilities are supposed to occur only rarely in a large sample size of trajectories. With a small sample size like ours (101 trajectories) such paths would be over-represented and are thus excluded from analysis.

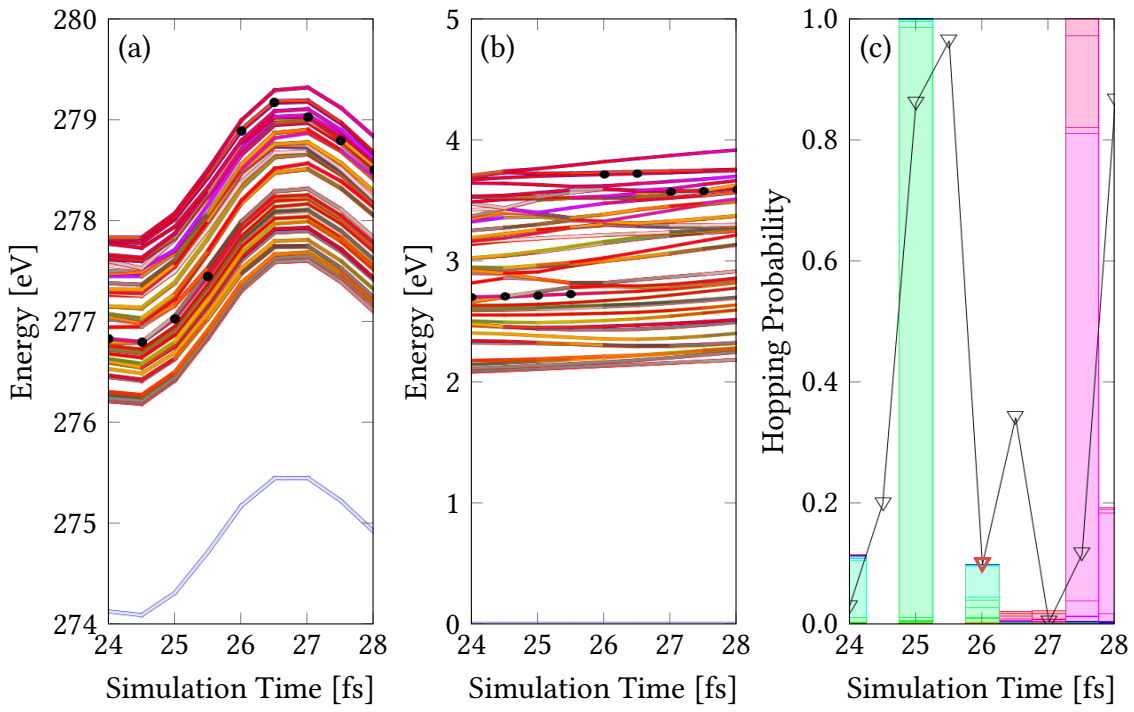

Figure A7: (a) Adiabatic states, the circle represents the active state. (b) Diagonal states, the circle represents the active state. (c) Hopping probabilities for the various adiabatic states, the triangle represents the random number.

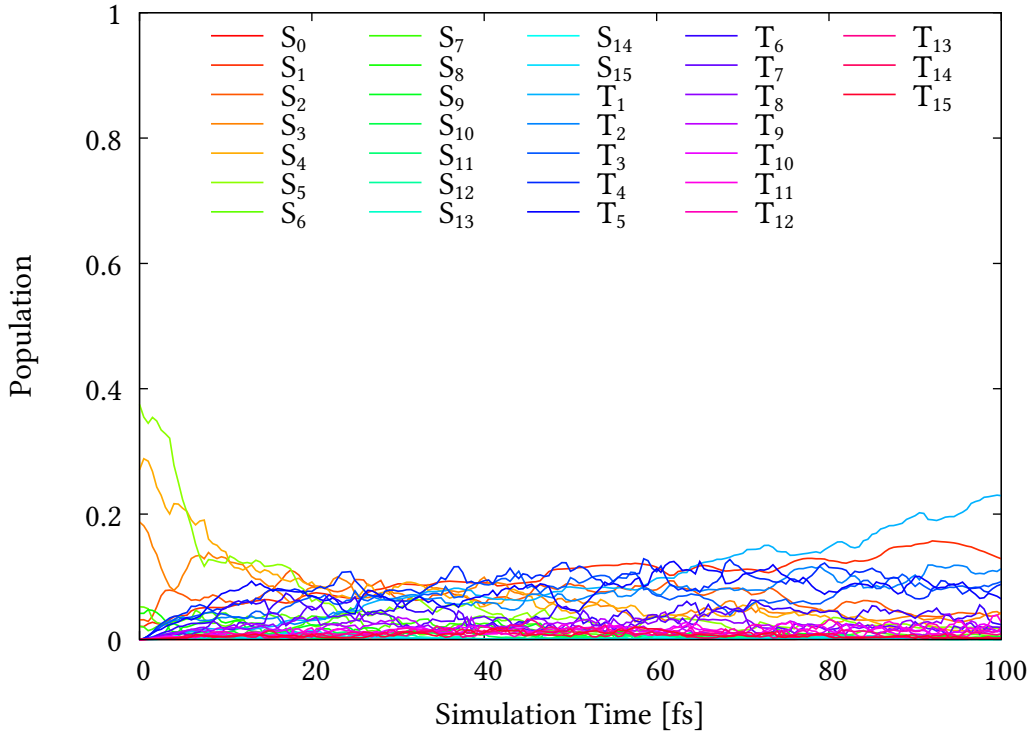

Figure A8: Electronic population of all considered states (S_0-S_{15}, T_1-T_{15}) within the TD-DFT /SH dynamics for 100 fs.

Table A3: Difference transition matrix of the 100 fs TD-DFT/SH dynamics indicating the population pathways.

	S_0	S_1	S_2	S_3	$_4$	S_5	S_6	S_7	S_8	S_9	S_{10}	S_{11}	S_{12}	S_{13}	S_{14}	S_{15}	T_1	T_2	T_3	T_4	T_5	T_6	T_7	T_8	T_9	T_{10}	T_{11}	T_{12}	T_{13}	T_{14}	T_{15}	Sum
S_0	0	0	0	0	0	0	0	0	0	0	0	0	0	0	0	0	0	0	0	0	0	0	0	0	0	0	0	0	0	0	0
S_1	0	0	12	2	1	2	0	0	0	0	0	0	0	0	0	0	-1	-1	-6	-2	1	0	1	0	0	0	0	0	0	0	0	9
S_2	0	-12	0	13	10	1	0	0	0	0	0	0	0	0	0	0	0	-2	-7	5	-4	-1	1	0	0	0	0	0	0	0	0	4
S_3	0	-2	-13	0	8	4	0	0	0	-1	0	0	0	-1	0	0	0	0	-5	0	-4	0	3	-2	1	0	0	0	0	0	0	-12
S_4	0	-1	-10	-8	0	13	0	1	0	0	0	0	0	0	0	0	0	0	0	0	6	-15	-7	-1	2	0	0	-1	0	0	0	-21
S_5	0	-2	-1	-4	-13	0	3	1	-1	0	0	0	0	0	0	0	0	0	0	0	-4	-7	2	-1	-1	-3	0	0	0	0	0	-31
S_6	0	0	0	0	0	-3	0	-4	3	-1	0	0	0	0	0	0	0	0	0	0	0	1	-3	0	3	0	-2	2	0	0	0	-4
S_7	0	0	0	0	-1	-1	4	0	1	2	-1	0	0	0	0	0	0	0	0	0	0	0	-1	-2	-1	0	1	-1	1	-1	0	0
S_8	0	0	0	0	0	1	-3	-1	0	-2	0	0	0	-1	0	0	0	0	0	0	0	0	0	0	-1	2	-1	0	0	1	1	-4
S_9	0	0	0	1	0	0	1	-2	2	0	6	2	-1	-1	0	0	0	0	0	0	0	0	0	0	0	-1	2	-2	-3	-1	-3	0
S_{10}	0	0	0	0	0	0	0	1	0	-6	0	2	0	0	0	0	0	0	0	0	0	0	0	0	0	0	0	0	2	-1	2	0
S_{11}	0	0	0	0	0	0	0	0	0	-2	-2	0	2	1	0	0	0	0	0	0	0	0	0	0	0	0	0	0	0	0	1	0
S_{12}	0	0	0	0	0	0	0	0	0	1	0	-2	0	2	0	0	0	0	0	0	0	0	0	0	0	0	0	0	0	0	-1	0
S_{13}	0	0	0	1	0	0	0	0	1	1	0	-1	-2	0	-2	2	0	0	0	0	0	0	0	0	0	0	0	0	0	0	0	0
S_{14}	0	0	0	0	0	0	0	0	0	0	0	0	0	2	0	-1	0	0	0	0	0	0	0	0	0	0	0	0	0	0	-1	0
S_{15}	0	0	0	0	0	0	0	0	0	0	0	0	0	-2	1	0	0	0	0	0	0	0	0	0	0	0	0	0	0	0	1	0
T_1	0	1	0	0	0	0	0	0	0	0	0	0	0	0	0	0	0	18	1	1	0	0	0	0	0	0	0	0	0	0	0	21
T_2	0	1	2	0	0	0	0	0	0	0	0	0	0	0	0	0	-18	0	14	8	0	0	0	0	0	0	0	0	0	0	0	7
T_3	0	6	7	5	0	0	0	0	0	0	0	0	0	0	0	0	-1	-14	0	8	-3	1	0	0	0	0	0	0	0	0	0	9
T_4	0	2	-5	0	0	0	0	0	0	0	0	0	0	0	0	0	-1	-8	-8	0	21	6	0	0	0	0	0	0	0	0	0	7
T_5	0	-1	4	4	-6	4	0	0	0	0	0	0	0	0	0	0	0	0	3	-21	0	16	2	0	0	0	0	0	0	0	-1	4
T_6	0	0	1	0	15	7	-1	0	0	0	0	0	0	0	0	0	0	0	-1	-6	-16	0	1	0	1	0	0	0	0	0	0	1
T_7	0	-1	-1	-3	7	-2	3	1	0	0	0	0	0	0	0	0	0	0	0	0	-2	-1	0	1	0	-1	-1	0	0	0	0	0
T_8	0	0	0	2	1	1	0	2	0	0	0	0	0	0	0	0	0	0	0	0	0	0	-1	0	-1	-2	1	0	0	0	0	3
T_9	0	0	0	-1	-2	1	-3	1	1	0	0	0	0	0	0	0	0	0	0	0	0	-1	0	1	0	-1	5	-1	0	1	0	1
T_{10}	0	0	0	0	0	3	0	0	-2	1	0	0	0	0	0	0	0	0	0	0	0	0	1	2	1	0	-8	1	1	0	0	0
T_{11}	0	0	0	0	0	0	2	-1	1	-2	0	0	0	0	0	0	0	0	0	0	0	0	1	-1	-5	8	0	1	1	-2	0	3
T_{12}	0	0	0	0	1	0	-2	1	0	2	0	0	0	0	0	0	0	0	0	0	0	0	0	0	1	-1	-1	0	1	2	-2	2
T_{13}	0	0	0	0	0	0	0	-1	0	3	-2	0	0	0	0	0	0	0	0	0	0	0	0	0	0	-1	-1	-1	0	4	0	1
T_{14}	0	0	0	0	0	0	0	1	-1	1	1	0	1	0	1	0	0	0	0	0	0	0	0	0	-1	0	2	-2	-4	0	1	0
T_{15}	0	0	0	0	0	0	0	0	-1	3	-2	-1	0	0	0	-1	0	0	0	0	1	0	0	0	0	0	0	2	0	-1	0	0
Sum	0	-9	-4	12	21	31	4	0	4	0	0	0	0	0	0	0	-21	-7	-9	-7	-4	-1	0	-3	-1	0	-3	-2	-1	0	0	0

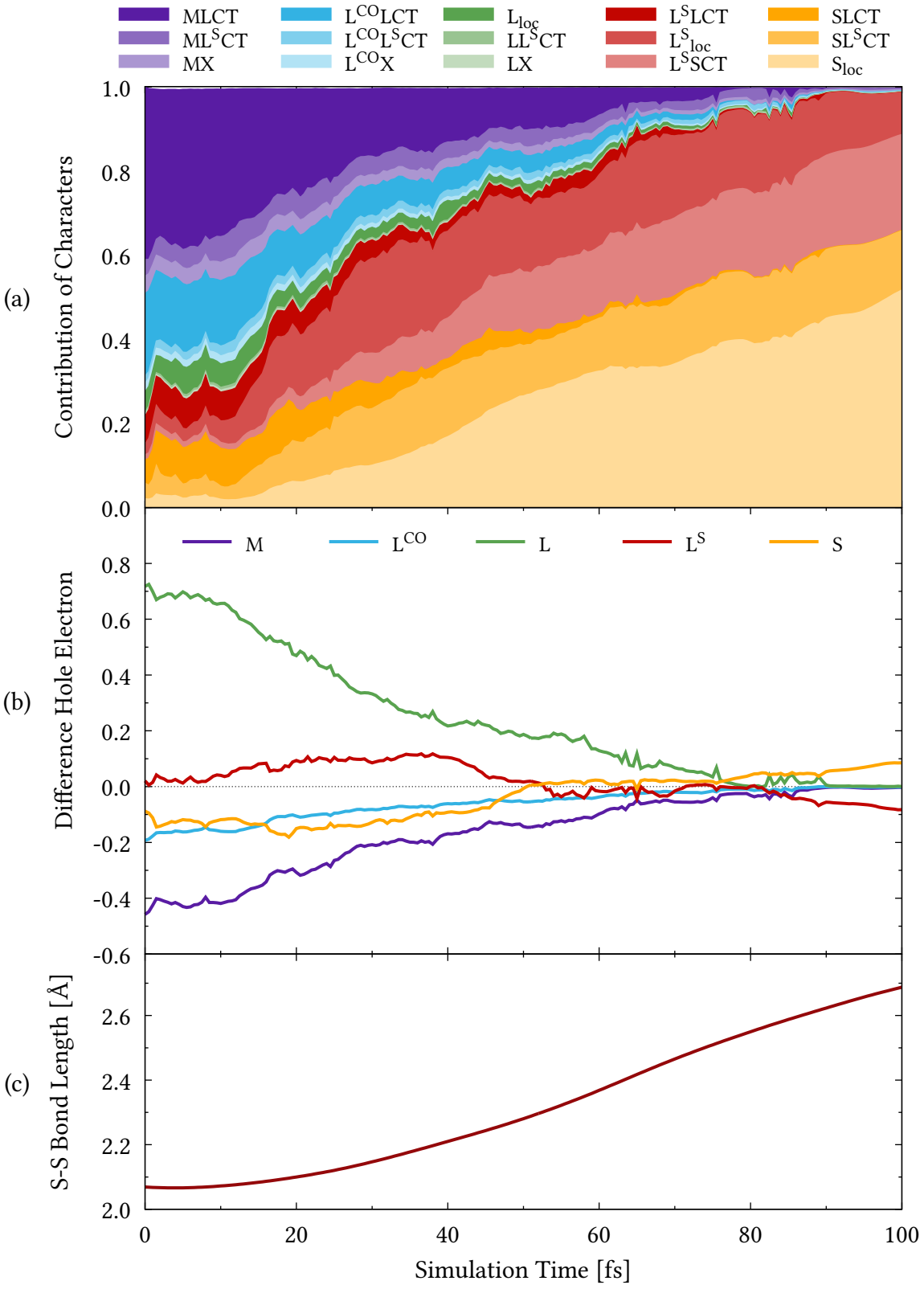

Figure A9: (a) Contribution of excited state characters, (b) difference population (hole-electron), and (c) S-S bond length over the simulation time for all S-S$_{long}$ trajectories. Fragments M and L^{CO} shown seperate1ly.

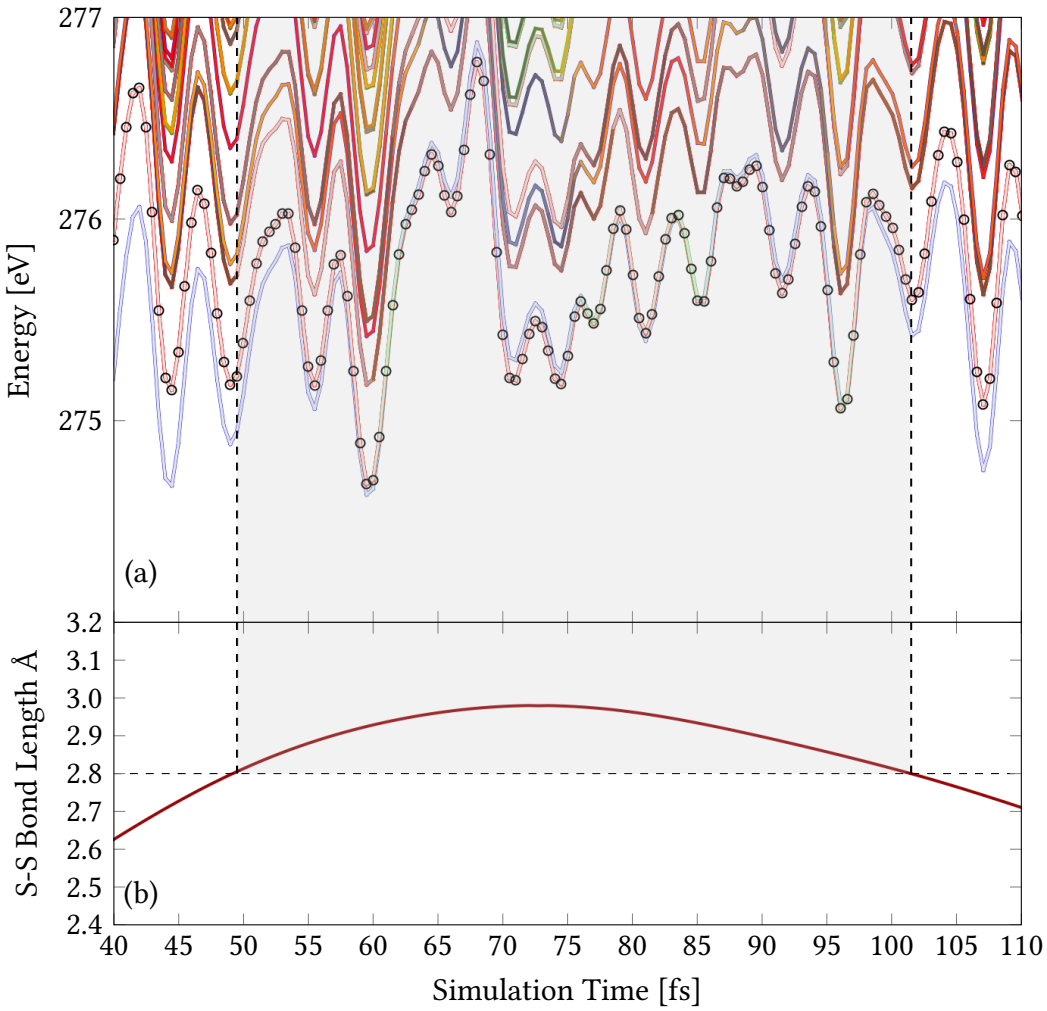

Figure A10: (a) Adiabatic states (not all shown) within the TD-DFT /SH dynamics for an example S-S_{long} trajectory. The active state is indicated by circles. In this case the active state is the T_1 throughout the shown simulation time. (b) The S-S bond length over the simulation time. The dashed line along 2.8 Å indicates the bond length of the S_0/T_1 MECP. The gray box depicts the region where the S-S bond length of the trajectory is beyond the MECP bond length. In this region, the S_0 (lowest blue curve) and T_1 (lowest red curve) become very close in energy, with the T_1 even being the lowest energy state. At bond lengths smaller than 2.8 Å the S_0 and T_1 show a more clear separation.

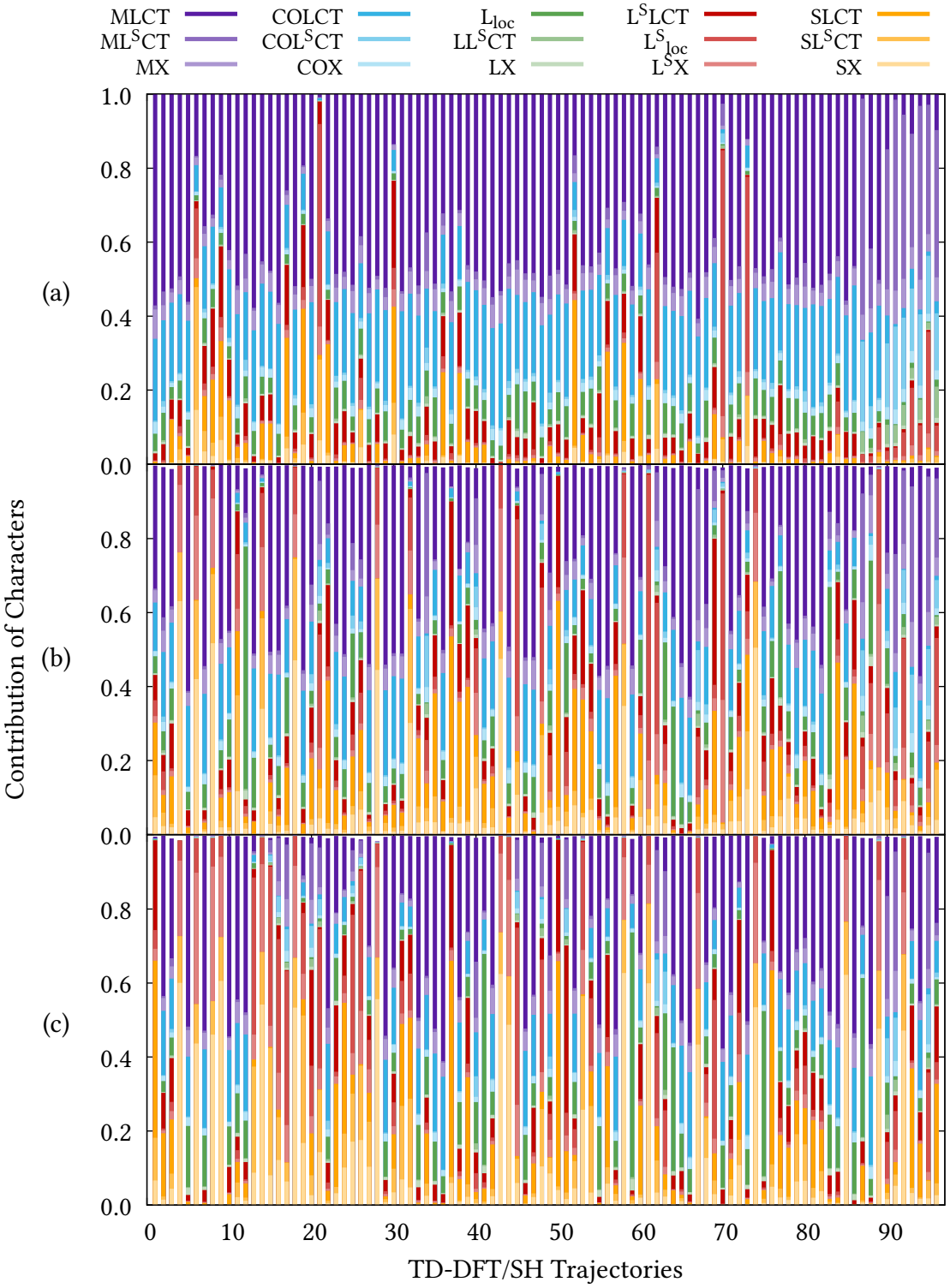

Figure A11: Character contributions of the active state of each individual trajectory at (a) $t = 0\,\text{fs}$, (b) $t = 50\,\text{fs}$, and (c) $t = 100\,\text{fs}$. It can be seen, that the initally populates states (a) show rather uniform character with mostly M'LCT. Over the simulation time however, the trajectories reach states of varying characters. The S-S$_{\text{long}}$ trajectories are characterized by high S$_{\text{loc}}$ contribution (bright yellow). The S-S$_{\text{short}}$ trajectories are more mixed in character.

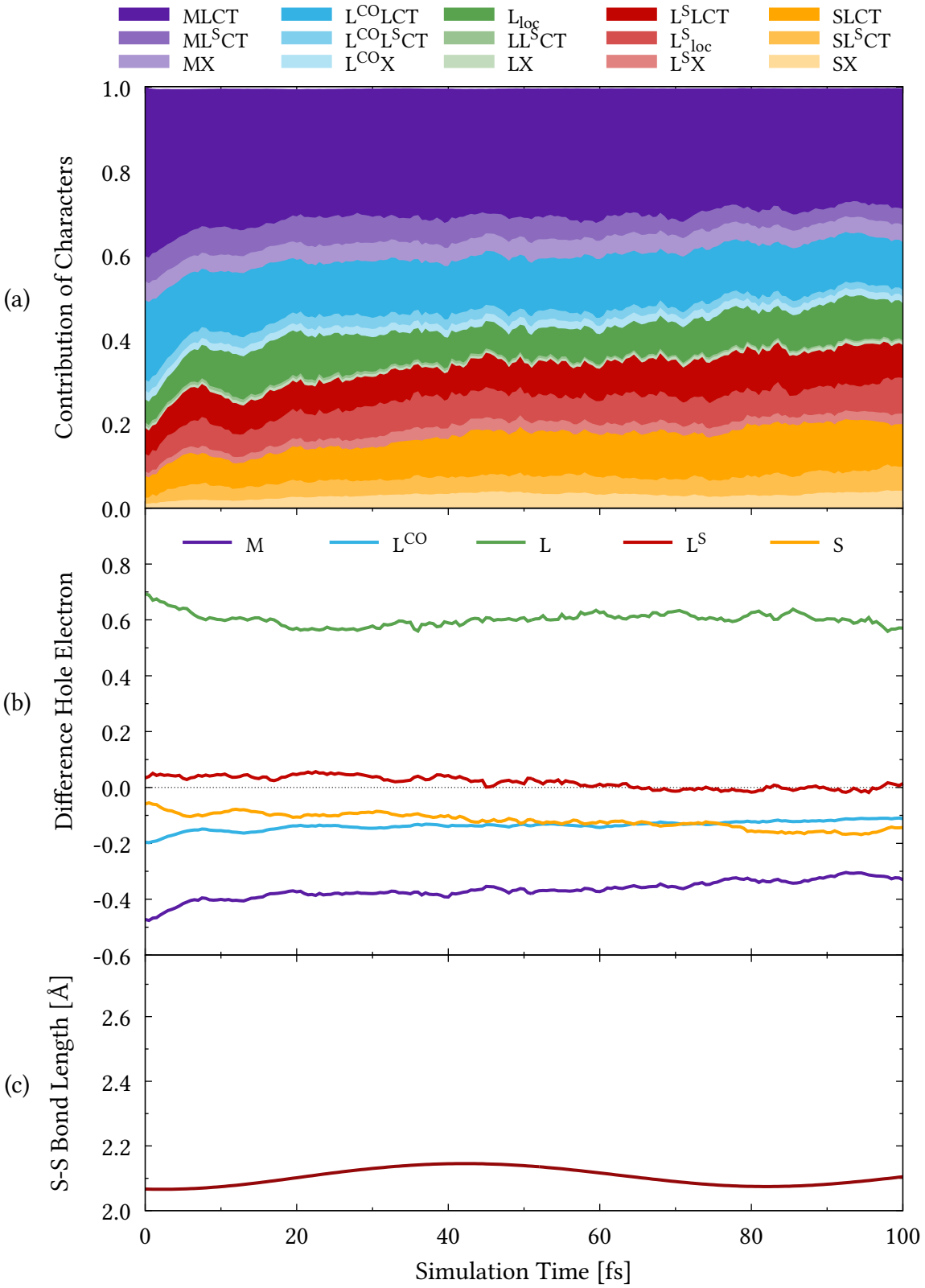

Figure A12: (a) Contribution of excited state characters, (b) difference population (hole-electron), and (c) S-S bond length over the simulation time for all S-S$_{short}$ trajectories. Fragments M and L^{CO} shown seperately.

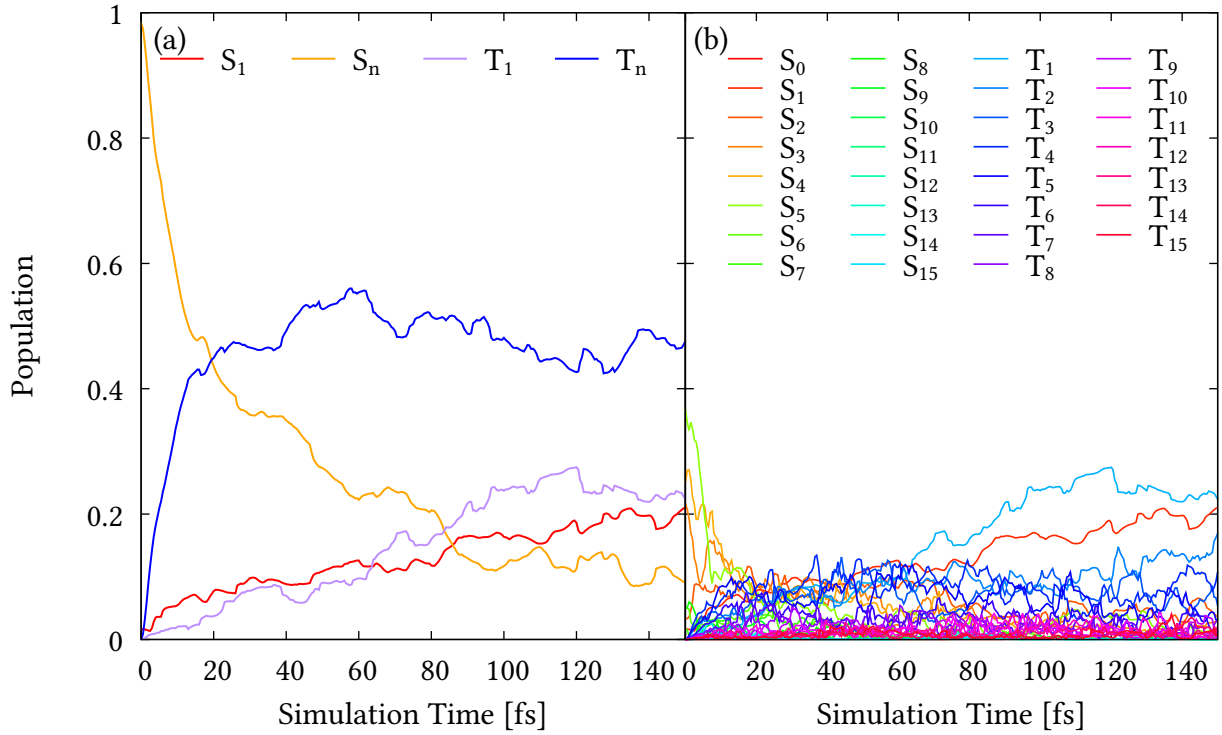

Figure A13: (a) Population of the established state groups (S_1, S_n, T_1, and T_n) and (b) Population of all considered electronic states (S_0-S_{15}, T_1-T_{15}) within the TD-DFT/SH dynamics for 150 fs.

A.6 LVC/SH Dynamics

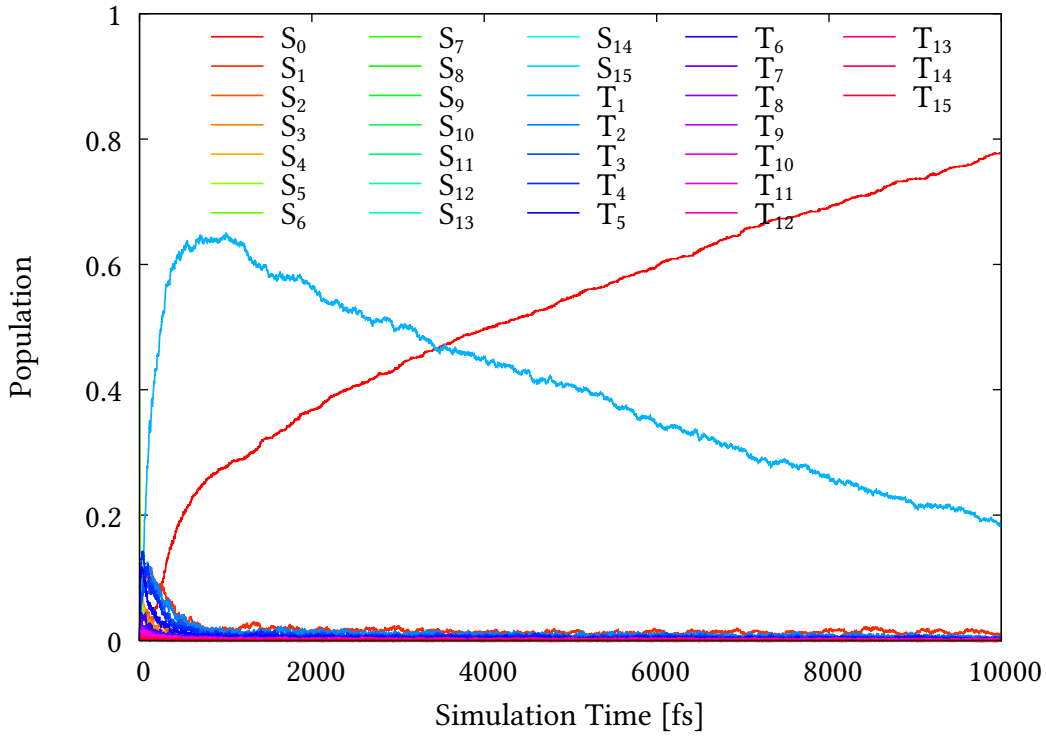

Figure A14: Electronic populations of the LVC/SH dynamics discussed in the main text (992 trajectories, 0.99999 damping, S_0quit, v rescaling) for all computed excited states (S_0-S_{15}, T_1-T_{15}).

Table A4: Difference transition matrix of the 10 ps LVC/SH dynamics indicating the population pathways.

	S_0	S_1	S_2	S_3	$_4$	S_5	S_6	S_7	S_8	S_9	S_{10}	S_{11}	S_{12}	S_{13}	S_{14}	S_{15}	T_1	T_2	T_3	T_4	T_5	T_6	T_7	T_8	T_9	T_{10}	T_{11}	T_{12}	T_{13}	T_{14}	T_{15}	Sum
S_0	0	774	-1	0	0	0	0	0	0	0	0	0	0	0	0	0	0	0	0	0	0	0	0	0	0	0	0	0	0	0	773
S_1	-774	0	297	32	-9	7	-1	1	-3	-3	-4	-1	-1	-2	-5	-4	284	45	86	59	-4	0	-2	0	0	-1	-1	-6	0	0	0	-10
S_2	1	-297	0	201	34	-6	-3	1	-6	-4	-2	-4	-2	-3	-1	1	-7	-113	-71	147	41	16	3	-1	0	-2	-2	-1	1	-1	-2	-82
S_3	0	-32	-201	0	154	15	-8	-4	-1	-4	-1	-3	-1	-2	0	-1	9	5	-110	-116	73	20	3	11	-2	1	-2	-2	-1	0	-1	-201
S_4	0	9	-34	-154	0	279	-17	-3	2	0	-2	-1	0	-1	-1	-2	16	1	-6	-87	-196	-11	-2	3	7	-1	-1	0	-1	-2	0	-205
S_5	0	-7	6	-15	-279	0	66	0	1	-2	-1	-2	-1	0	-1	0	16	-1	1	-38	-85	-66	-29	22	39	2	-2	-2	0	0	-1	-379
S_6	0	1	3	8	17	-66	0	38	-17	4	0	-2	-4	0	-1	-1	16	1	-2	7	-3	29	-97	-14	13	6	14	-2	-1	0	0	-53
S_7	0	-1	-1	4	3	0	-38	0	32	-7	0	-1	3	-2	-2	0	9	0	2	0	5	-3	-28	-23	7	21	-6	3	3	1	-3	-22
S_8	0	3	6	1	-2	-1	17	-32	0	27	-8	8	1	-3	0	0	9	0	-1	1	0	-3	6	-7	-1	-30	7	-12	6	1	-1	-8
S_9	0	3	4	4	0	2	-4	7	-27	0	69	-12	-7	-1	-1	0	9	4	0	3	0	0	-1	2	3	-11	-14	-17	-5	-6	-6	-2
S_{10}	0	4	2	1	2	1	0	0	8	-69	0	48	-5	2	0	-1	4	1	1	-1	2	1	-2	0	4	-6	-18	-8	-17	48	-2	0
S_{11}	0	1	4	3	1	2	2	1	-8	12	-48	0	-4	8	-3	1	2	0	1	1	2	1	0	1	1	2	3	0	5	16	-7	0
S_{12}	0	1	2	1	0	1	4	-3	-1	7	5	4	0	23	2	-3	1	2	1	0	0	0	0	0	0	1	0	3	-8	-34	-9	0
S_{13}	0	2	3	2	1	0	0	2	3	1	-2	-8	-23	0	20	0	1	0	2	1	0	0	0	-1	-1	2	-1	1	2	-4	-3	0
S_{14}	0	5	1	0	1	1	1	2	0	1	0	3	-2	-20	0	8	1	0	1	0	1	0	-1	0	0	1	1	-2	1	0	-4	0
S_{15}	0	4	-1	1	2	0	1	0	0	0	1	-1	3	0	-8	0	0	0	0	0	0	0	0	0	0	1	1	0	1	0	-5	0
T_1	0	-284	7	-9	-16	-16	-16	-9	-9	-9	-4	-2	-1	-1	-1	0	0	1347	7	-46	-123	-96	-88	-84	-73	-66	-59	-39	-36	-40	-48	186
T_2	0	-45	113	-5	-1	1	-1	0	0	-4	-1	0	-2	0	0	0	-1347	0	1134	182	19	-6	-5	-8	-4	-3	-5	0	0	-5	-2	5
T_3	0	-86	71	110	6	-1	2	-2	1	0	-1	-1	-1	-2	-1	0	-7	-1134	0	1060	59	-21	-6	-7	-1	-7	-7	-6	-6	-3	-4	5
T_4	0	-59	-147	116	87	38	-7	0	-1	-3	1	-1	0	-1	0	0	46	-182	-1060	0	1134	60	3	-1	-8	0	-1	-7	-4	-1	-3	-1
T_5	0	4	-41	-73	196	85	3	-5	0	0	-2	-2	0	0	-1	0	123	-19	-59	-1134	0	838	89	17	3	-9	-2	-4	-6	-1	-2	-2
T_6	0	0	-16	-20	11	66	-29	3	3	0	-1	-1	0	0	0	0	96	6	21	-60	-838	0	671	54	35	-3	0	-2	-1	1	0	-4
T_7	0	2	-3	-3	2	29	97	28	-6	1	2	0	0	0	1	0	88	5	6	-3	-89	-671	0	417	62	21	8	3	3	-1	0	-1
T_8	0	0	1	-11	-3	-22	14	23	7	-2	0	-1	0	1	0	0	84	8	7	1	-17	-54	-417	0	303	71	11	3	-6	-1	0	0
T_9	0	0	0	2	-7	-39	-13	-7	1	-3	-4	-1	0	1	0	0	73	4	1	8	-3	-35	-62	-303	0	329	75	-9	-8	-2	1	-1
T_{10}	0	1	2	-1	1	-2	-6	-21	30	11	6	-2	-1	-2	-1	-1	66	3	7	0	9	3	-21	-71	-329	0	276	59	-4	-11	0	1
T_{11}	0	1	2	2	1	2	-14	6	-7	14	18	-3	0	1	-1	-1	59	5	7	1	2	0	-8	-11	-75	-276	0	241	33	-4	5	0
T_{12}	0	6	1	2	0	2	2	-3	12	17	8	0	-3	-1	2	0	39	0	6	7	4	2	-3	-3	9	-59	-241	0	163	20	11	0
T_{13}	0	0	-1	1	1	0	1	-3	-6	5	17	-5	8	-2	-1	-1	36	0	6	4	6	1	-3	6	8	4	-33	-163	0	99	15	0
T_{14}	0	0	1	0	2	0	0	-1	-1	6	-48	-16	34	4	0	0	40	5	3	1	1	-1	1	1	2	11	4	-20	-99	0	71	1
T_{15}	0	0	2	1	0	1	0	3	1	6	2	7	9	3	4	5	48	2	4	3	2	0	0	0	-1	0	-5	-11	-15	-71	0	0
Sum	-773	10	82	201	205	379	53	22	8	2	0	0	0	0	0	0	-186	-5	-5	1	2	4	1	0	1	-1	0	0	0	-1	0	0

Figure A15 shows an alternative kinetic model for the LVC/SH dynamics for the early dynamics up to 1 ps. It was established in an effort to improve the fit of the predicted populations to the computed populations. The kinetic model discussed in the main text (Fig. 16) lacks in the description of the decreasing population of S_1, as it decreases too early. Additionally, the population of the S_0 is predicted to start too early compared to what is seen from the calculations. The kinetic model seen in Figure A15b incorporates internal relaxation within the S_1 states denoted by S_1a and S_1b.

Accounting for the relaxation within the S_1 state allows the population to stay in the S_1 for longer, thus yielding a very good fit for the population curve of the S_1. The increasing population of the S_0 is also slightly delayed compared to the model discussed in the main text, but is still predicted too early compared to the computed populations. Thus, the herein proposed model was able to slightly improve the one discussed in the main text, but was not able to fully describe the onset of the ground state population. For simplicity sake, the relaxation within the S_1 state was not included in the final relaxation pathway discussed in the main text.

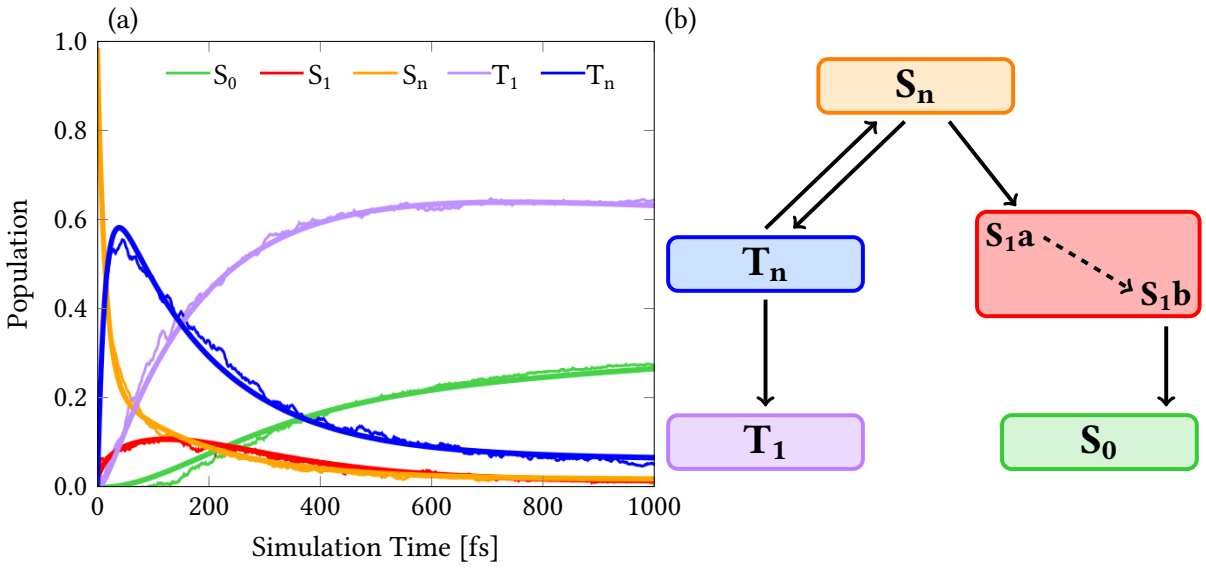

Figure A15: (a) Electronic populations (thin lines) of the LVC/SH dynamics. The bold lines indicate the fitted populations according to the kinetic model shown in (b) using the data points of the LVC/SH dynamics for 1 ps simulation time.

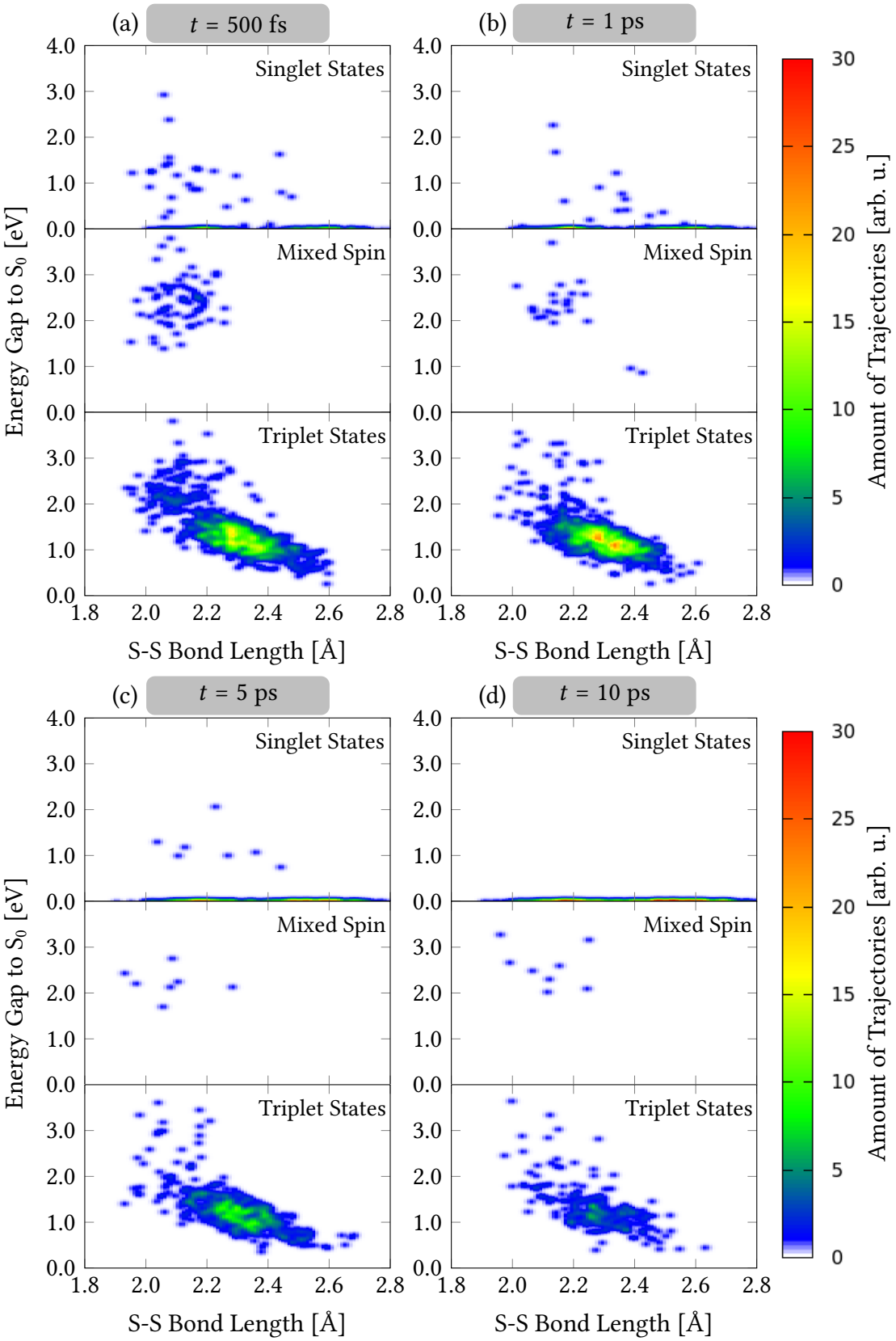

Figure A16: Geometric analysis of the LVC/SH dynamics. S-S bond length [Å] against energy gap of the active state to the ground state S_0 [eV] at (a) $t = 500\,\text{fs}$, (b) $t = 1\,\text{ps}$, (c) $t = 5\,\text{ps}$, (d) $t = 10\,\text{ps}$. Trajectories divided by spin expectation value $\langle S^2 \rangle$ ($0.2 > \langle S^2 \rangle$ singlet states, $0.2 < \langle S^2 \rangle < 1.8$ mixed spin, and $\langle S^2 \rangle > 1.8$ triplet states).